AD-A145 394 LOW-SPEED WIND TUNNEL TEST ON JOINED WING AND MONOPLANE 1/2
CONFIGURATIONS VO..(U) ACA INDUSTRIES INC RANCHO PALOS
VERDES CA J WOLKOVITCH FEB 82 ACA-82-1
UNCLASSIFIED N00014-79-C-0953 F/G 20/4 NL

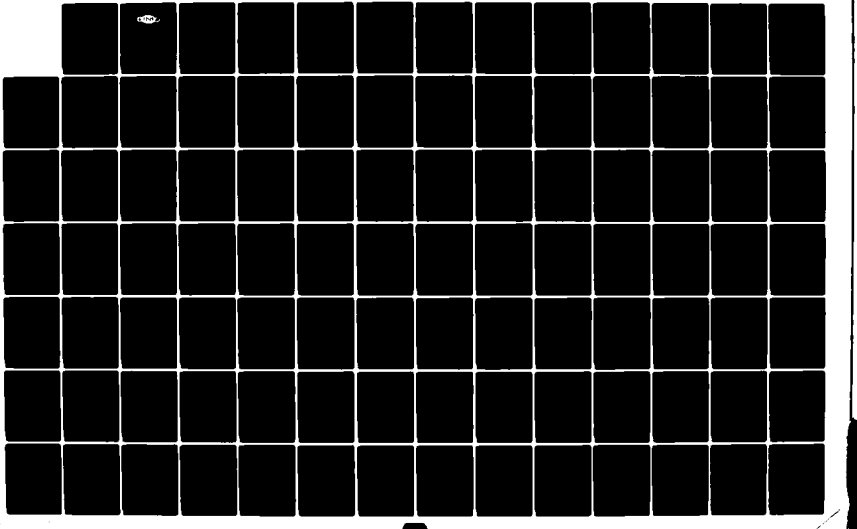

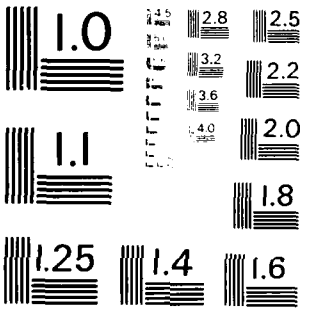

ACA REPORT 82-1

LOW-SPEED WIND TUNNEL TEST ON JOINED WING AND MONOPLANE CONFIGURATIONS

Volume I. Analysis of Results

Julian Wolkovitch

ACA Industries Inc.
28603 Trailriders Drive
Rancho Palos Verdes
California 90274

Contract N00014-79-C-0953

Final Report

Final Report for Phase II

Approved for public release; distribution unlimited

Prepared for

Office of Naval Research, 800 N. Quincy St., Arlington, VA 22217

FOREWORD

The research described in this report was supported by the Office of Naval Research under Contract N00014-79-C-0953 with Dr. Robert E. Whitehead as ONR Contract Technical Monitor.

Additional research on the joined wing concept is now in progress. This research includes generalized structural analyses and further wind tunnel tests. Detailed information on these research efforts can be obtained from the author.

SECURITY CLASSIFICATION O IS PAGE (When Data Entered)

REPORT DOCUMENTATION PAGE

READ INSTRUCTIONS BEFORE COMPLETING FORM

1. REPORT NUMBER ACA Report 82-1	2. GOVT ACCESSION NO. A145 394 / 3. RECIPIENT'S CATALOG NUMBER
4. TITLE (and Subtitle) LOW-SPEED WIND TUNNEL TEST ON JOINED WING AND MONOPLANE CONFIGURATIONS Volume I: Analysis of Results	5. TYPE OF REPORT & PERIOD COVERED Technical Report Volume I 6. PERFORMING ORG. REPORT NUMBER ACA Report 82-1
7. AUTHOR(s) Julian Wolkovitch	8. CONTRACT OR GRANT NUMBER(s) N00014-79-C-0953
9. PERFORMING ORGANIZATION NAME AND ADDRESS ACA Industries Inc. 28603 Trailriders Drive Rancho Palos Verdes, CA 90274	10. PROGRAM ELEMENT, PROJECT, TASK AREA & WORK UNIT NUMBERS 62241N RF41-411
11. CONTROLLING OFFICE NAME AND ADDRESS Office of Naval Research (Code 210) 800 North Quincy Street Arlington, VA 22217	12. REPORT DATE February 1982 13. NUMBER OF PAGES 112
14. MONITORING AGENCY NAME & ADDRESS(if different from Controlling Office)	15. SECURITY CLASS. (of this report) Unclassified 15a. DECLASSIFICATION DOWNGRADING SCHEDULE

16. DISTRIBUTION STATEMENT (of this Report)

Approved for public release; distribution unlimited.

17. DISTRIBUTION STATEMENT (of the abstract entered in Block 20, if different from Report)

18. SUPPLEMENTARY NOTES

19. KEY WORDS (Continue on reverse side if necessary and identify by block number)

Joined wing, tandem wing, cruise missile, aircraft design, aerodynamics

20. ABSTRACT (Continue on reverse side if necessary and identify by block number)

The joined wing is a new airplane and missile configuration comprising two wings, a fuselage, and a fin, such that the wings form diamond shapes both in plan view and front view. Advantages claimed for the joined wing include lightness, stiffness, low induced drag, low wave drag and high trimmed maximum lift coefficient. Comparative low-speed wind tunnel tests were performed on joined wing and conventional wing configurations having

(Continued)

20. ABSTRACT (Concluded)

similar areas and spans. The effect of adding canard surfaces to the joined wing was investigated. The joined wing developed less induced drag than the comparable conventional wing, gave a higher maximum trimmed lift coefficient, and showed generally good stability and control characteristics, except for low directional stability. Favorable canard/joined wing interactions were found, yielding further increases in maximum lift coefficient. ~~The present report~~ (Volume I) analyses the test data, which are presented in Volume II.

TABLE OF CONTENTS

1.0 BACKGROUND

1.1 BACKGROUND TO THE TESTS

The present report is Volume I of a 2-volume set which describes wind tunnel test results for a new type of airplane and missile wing, known as the joined wing.* In Volume II the complete test results are presented with no analysis. The present volume analyzes the test results. For ease of reference, certain test data and model configuration details from Volume II are also given in Volume I, but both reports should be read to obtain a complete account of the tests and the significance of their results.

The joined wing concept has been fully described in Ref. 1. Accordingly only an abbreviated description is given here. The following paragraphs describing the joined wing are taken from Ref. 1.

The joined wing is a general concept which involves the combination of two wings, a fuselage, and a fin, such that the wings form a diamond shape both in plan view and in front view. Figure 1 shows a design for a joined wing manned aircraft. Figure 2 illustrates a design for an advanced cruise missile employing a foldable joined wing plus a canard. Many arrangements for joining the wings are possible. Figure 3 shows a design with the joint located inboard of the tips, while Fig. 4 shows that the joint can be a winglet, thus returning some aerodynamic benefit as well as providing the necessary structural tie between the wings.

Advantages claimed for the joined wing include:

- Light weight
- High stiffness
- Low induced drag
- Good transonic area distribution
- High trimmed $C_{L_{max}}$
- Reduced wetted area and parasite drag

*U.S. Patent 3,942,747. Other patents pending.

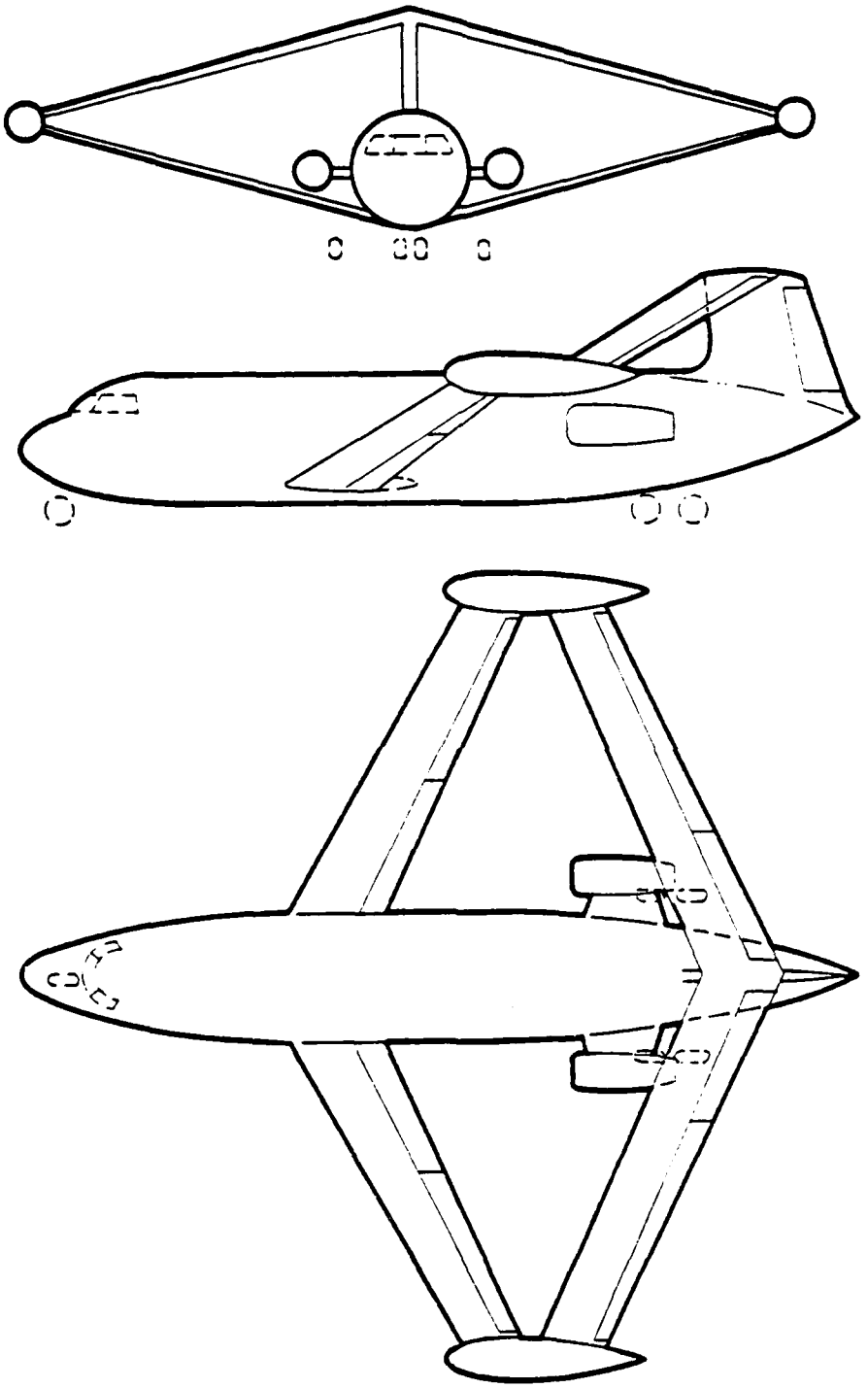

FIGURE 1. JOINED WING AIRPLANE

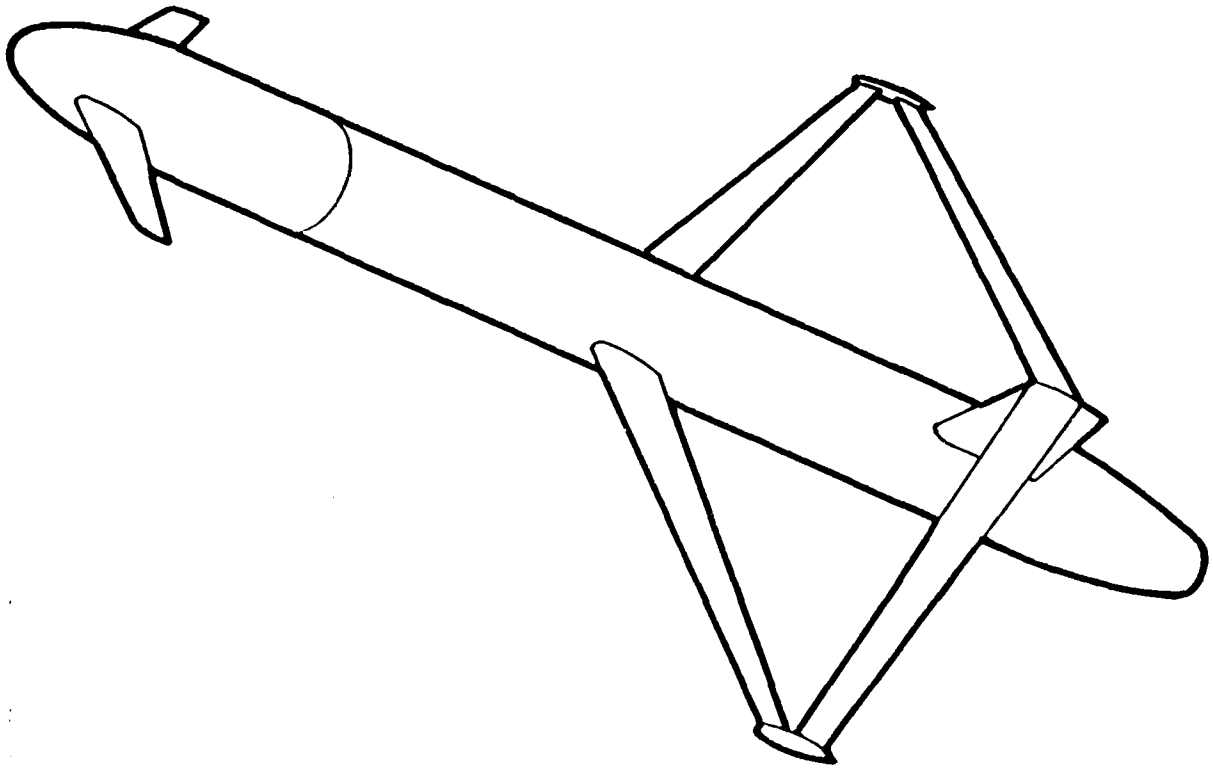

FIGURE 2. ADVANCED CRUISE MISSILE EMPLOYING JOINED WING AND CANARD

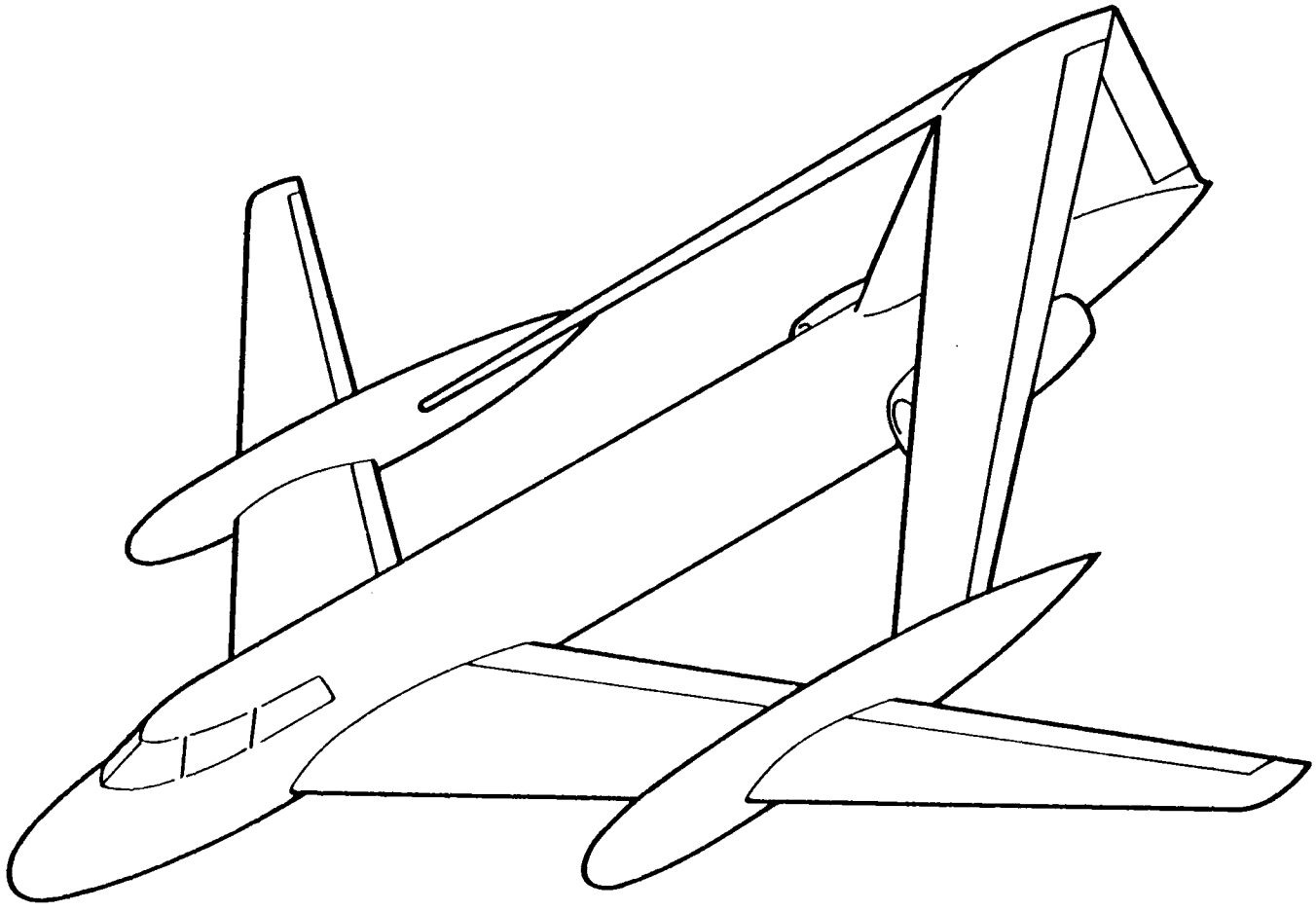

FIGURE 3. INBOARD-JOINT CONFIGURATION

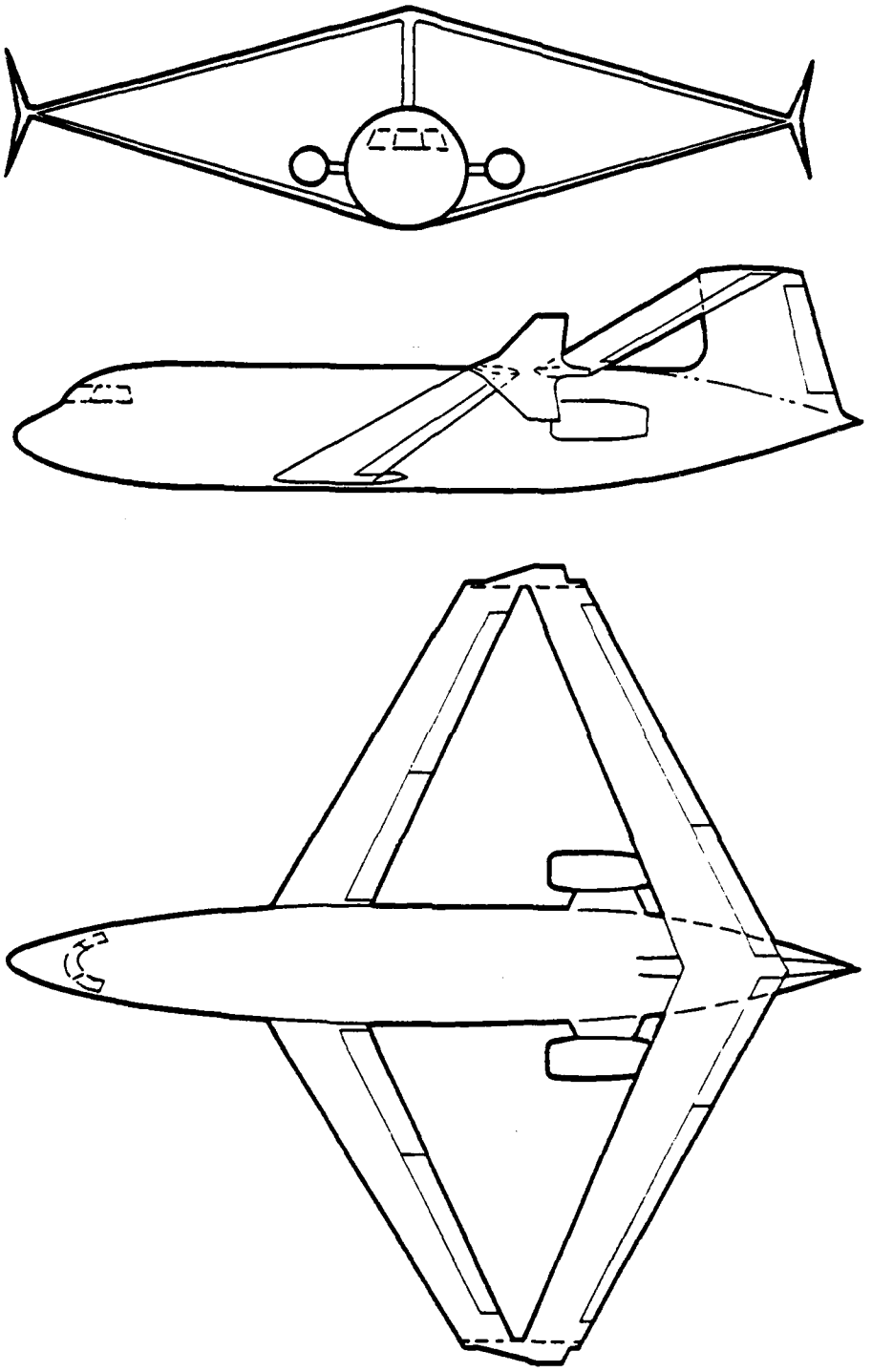

FIGURE 4. JOINED WING AIRPLANE WITH WINGLETS

- Direct lift control capability
- Direct sideforce control capability
- Good stability and control

These claims have been supported by independent analyses, design studies and wind tunnel tests, as described in Refs. 1 and 2.

1.2 TEST OBJECTIVES AND CONFIGURATIONS

Volume II of this report presents full configuration details. For ease of reference brief configuration descriptions are given below. Configuration dimensions and areas are given in Table 1.

The general objective of the test was to compare the aerodynamic characteristics of joined wing configurations versus baseline conventional (wing-plus-tail) configurations at low Mach numbers. Thus several baseline configurations were tested, as follows.

Baseline Configurations

BNWHDV: This is illustrated in Fig. 5. It represents a 0.5 scale model of an advanced cruise missile which employs a torpedo-shaped fuselage of similar dimensions to the fuselage of the current General Dynamics Tomahawk sea-launched cruise missile (SLCM). For the advanced cruise missile considered here the gross wing area full scale is 16.0 ft^2. This is approximately 1.33 times the wing area employed on the Tomahawk. The wing area was increased to improve maneuver and terrain-following capability and also to enhance high altitude cruise performance. The inlets were not represented on the model.

BWHDV: This configuration, shown in Fig. 6, is identical to BNWHDV except that the nose is shorter. The ratio of fuselage length to span is 1.38 as opposed to 1.09 for BNWHDV. This configuration was included to:

TABLE 1. CONFIGURATION DIMENSIONS AND AREAS

Dimensional Data Used for Data Reduction

	Conventional Wing	Joined Wing	Joined Wing With Canards
Projected Wing Area, S, (ft^2)	3.9998	3.9998	3.9998
Wing span, b, (ft.)	6.4625	6.4625	6.4625
Wing mean geometric chord, c, (ft.)	0.6189	0.6189	0.6189
Moment reference center location: F.S. (in.)	66.5800	73.0070	67.2306
W.L. (in.)	0	0	0
B.L. (in.)	0	0	0

TABLE 1. (CONTINUED)

General Model Dimensional Data

Conventional Wing, W

Total projected wing area	(ft^2)	3.9977
Exposed wing area	(ft^2)	3.3407
Wetted wing area	(ft^2)	6.8266
Wing mean geometric chord	(ft)	0.6186
Wing mean aerodynamic chord	(ft)	0.6415
Mean geometric chord of exposed area	(ft)	0.5964
Wing span (measured normal to fuselage plane of symmetry	(ft)	6.4625
Aspect ratio, b^2/S		10.4415
Sweep: at L.E.	(deg)	3.65
at 0.25 chord	(deg)	1.83
at 0.50 chord	(deg)	0
Dihedral (measured at wing T.E.)	(deg)	3.0
Root chord, C_R	(ft)	0.8248
Tip chord, C_T	(ft)	0.4124
Taper ratio, C_T/C_R		0.50
Wing location on fuselage:		
Root chord L.E.	(F.S.,in)	63.9887
0.25 MAC	(F.S.,in)	64.8134
0.25 MAC	(B.L.,in)	17.240

TABLE 1. (CONTINUED)

Joined Wing, F.R. (excluding fin)

		F	R
Total projected wing area	(ft^2)	2.4000	1.6000
Exposed wing area	(ft^2)	2.0431	1.6208
Wetted wing area	(ft^2)	4.1782	3.3145
Wing mean geometric chord	(ft)	0.3714	0.2476
Wing mean aerodynamic chord	(ft)	0.3851	0.2568
Wing span (excluding tip joint and measured normal to fuselage plane of symmetry), b	(ft)	6.4625	6.4625
Mean geometric chord of exposed area	(ft)	0.3552	0.2471
Wing span including tip joint, b_T	(ft)	6.5258	6.5258
Aspect ratio, b^2/S		17.4004	26.1006
Aspect ratio, b_T^2/S		17.7442	26.6163
Sweep: at L.E.	(deg)	30.00	-19.38
at 0.25 chord	(deg)	29.17	-20.03
at 0.50 chord	(deg)	28.33	-20.68
Dihedral (measured at wing T.E.)	(deg)	10.8	- 9.2
Root chord, C_R	(ft)	0.4952	0.3301
Tip chord, C_T	(ft)	0.2476	0.1651
Taper ratio, C_T/C_R		0.50	0.50
Wing location on fuselage:			
Root chord L.E.	(F.S.,in)	46.500	85.500
0.25 MAC	(F.S.,in)	57.6051	80.2069
0.25 MAC	(B.L.,in)	17.2335	17.2335

TABLE 1. (CONTINUED)

Joined Wing Vertical Airfoil Section

Exposed area	(ft^2)	0.2433
Wetted area	(ft^2)	0.4975
Mean geometric chord	(ft)	0.4700
Mean aerodynamic chord	(ft)	0.4820
Span (height), H	(ft)	0.5176
Aspect ratio, H^2/exposed area		1.1011
Sweep: at L.E.	(deg)	30.0
at 0.25 chord	(deg)	40.395
Root chord (at fuselage intersection), C_R	(ft)	0.600
Tip chord (at wing junction), C_T	(ft)	0.340
Taper ratio, C_T/C_R		0.567
Location on fuselage:		
Root chord L.E.	(F.S., in)	93.224
Tip chord L.E.	(F.S., in)	96.810
0.25 MAC	(F.S., in)	96.298
Root chord	(W.L., in)	5.000
Tip chord	(W.L., in)	11.211

TABLE 1. (CONTINUED)

Horizontal and Vertical Stabilizers, H,V,D

		H	V + D
Total projected area	(ft^2)	0.9601	0.9601
Exposed area	(ft^2)	0.5781	0.5781
Wetted area	(ft^2)	1.1822	1.1822
Mean geometric chord	(ft)	0.4500	0.4500
Mean aerodynamic chord	(ft)	0.4667	0.4667
Mean geometric chord of exposed area	(ft)	0.4467	0.4467
Span (between tips)	(ft)	2.1335	2.1335
Aspect ratio		4.741	4.741
Sweep: at L.E.	(deg)	30.0	30.0
at 0.25 chord	(deg)	32.930	32.930
at 0.50 chord	(deg)	35.677	35.677
Dihedral	(deg)	0	0
Root chord on fuselage $\mathcal{L}$, C_R	(ft)	0.600	0.600
Tip chord, C_T	(ft)	0.300	0.300
Taper ratio, C_T/C_R		0.500	0.500
Location on fuselage:			
Pivot for incidence angle change	(F.S., in)	113.96	--
Root chord L.E.	(F.S., in)	109.00	109.00
0.25 MAC	(F.S., in)	115.327	115.327
0.25 MAC	(W.L., in)	--	± 8.534
0.25 MAC	(B.L., in)	± 8.534	--

TABLE 1. (CONTINUED)

Canard Surfaces

		C_{30}	C_{60}
Total projected area	(ft^2)	0.9601	1.3482
Exposed area	(ft^2)	0.5188	0.4690
Wetted area	(ft^2)	1.0609	0.9509
Mean geometric chord	(ft)	0.4500	0.7946
Mean aerodynamic chord	(ft)	0.4667	0.7695
Mean geometric chord of exposed area	(ft)	0.3958	1.0959
Span	(ft)	2.1335	1.6967
Aspect ratio		4.741	2.1353
Sweep: at L.E.	(deg)	30.0	60.0
at 0.25 chord	(deg)	32.930	57.50
at 0.50 chord	(deg)	35.677	45.00
Dihedral	(deg)	0	0
Root chord, C_R	(ft)	0.600	1.013
Tip chord, C_T	(ft)	0.300	0.300*
Taper ratio, C_T/C_R		0.500	0.296
Location on fuselage:			
Pivot for incidence angle change	(F.S., in)	32.88	32.88
Root chord L.E.	(F.S., in)	27.92	19.22
0.25 MAC	(F.S., in)	38.448	28.85

*measured at 30° relative to aircraft plane of symmetry neglecting tip radius

TABLE 1. (CONCLUDED)

Body

		B	B + N
Overall length	(ft)	7.052	8.927
Body diameter (constant area section)	(ft)	0.8333	0.8333
Body diameter at base	(ft)	0.4375	0.4375
Leading edge	(F.S., in)	35.38	12.88
Trailing edge	(F.S., in)	120.00	120.00
Tapered aft body L.E.	(F.S., in)	109.00	109.00
Constant area section L.E.	(F.S., in)	50.42	27.92
Nose shape: semi-elliptical			
Semi major axis	(in)	15.04	15.04
Minor axis	(in)	10.00	10.00
Body wetted area	(ft^2)	18.7262	21.5362

Ailerons and Elevons

Dimensions given on Fig. 4 of Vol. II

Increase in wing wetted area due to addition of two ailerons or elevons	(ft^2)	0.4416

Strakes

Dimensions given on Fig. 5 of Vol. II

Increase in wing wetted area due to addition of two strakes	(ft^2)	0.1862

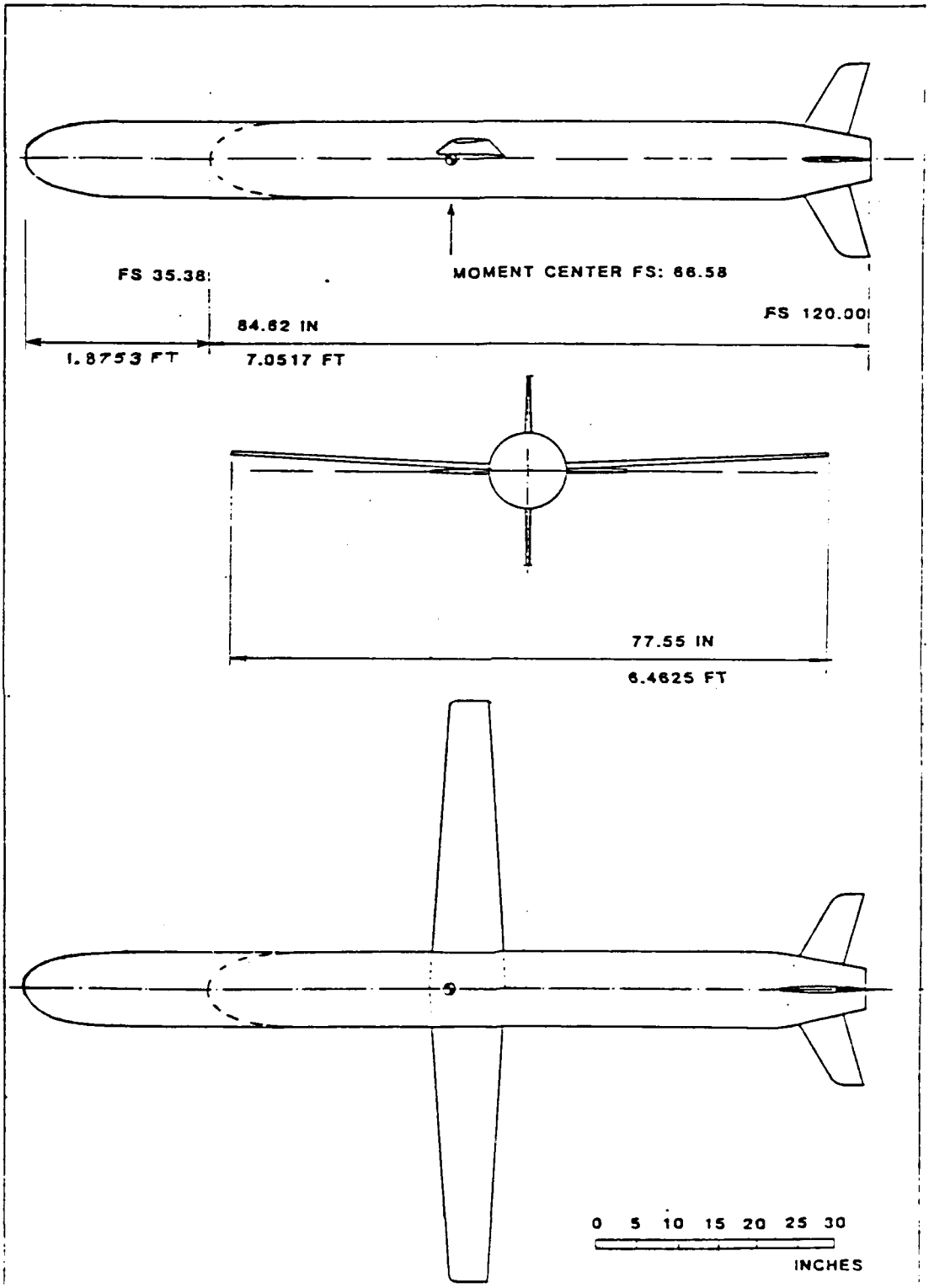

Figure 5. Baseline Configuration with Long Fuselage (Config. BNWHDV)

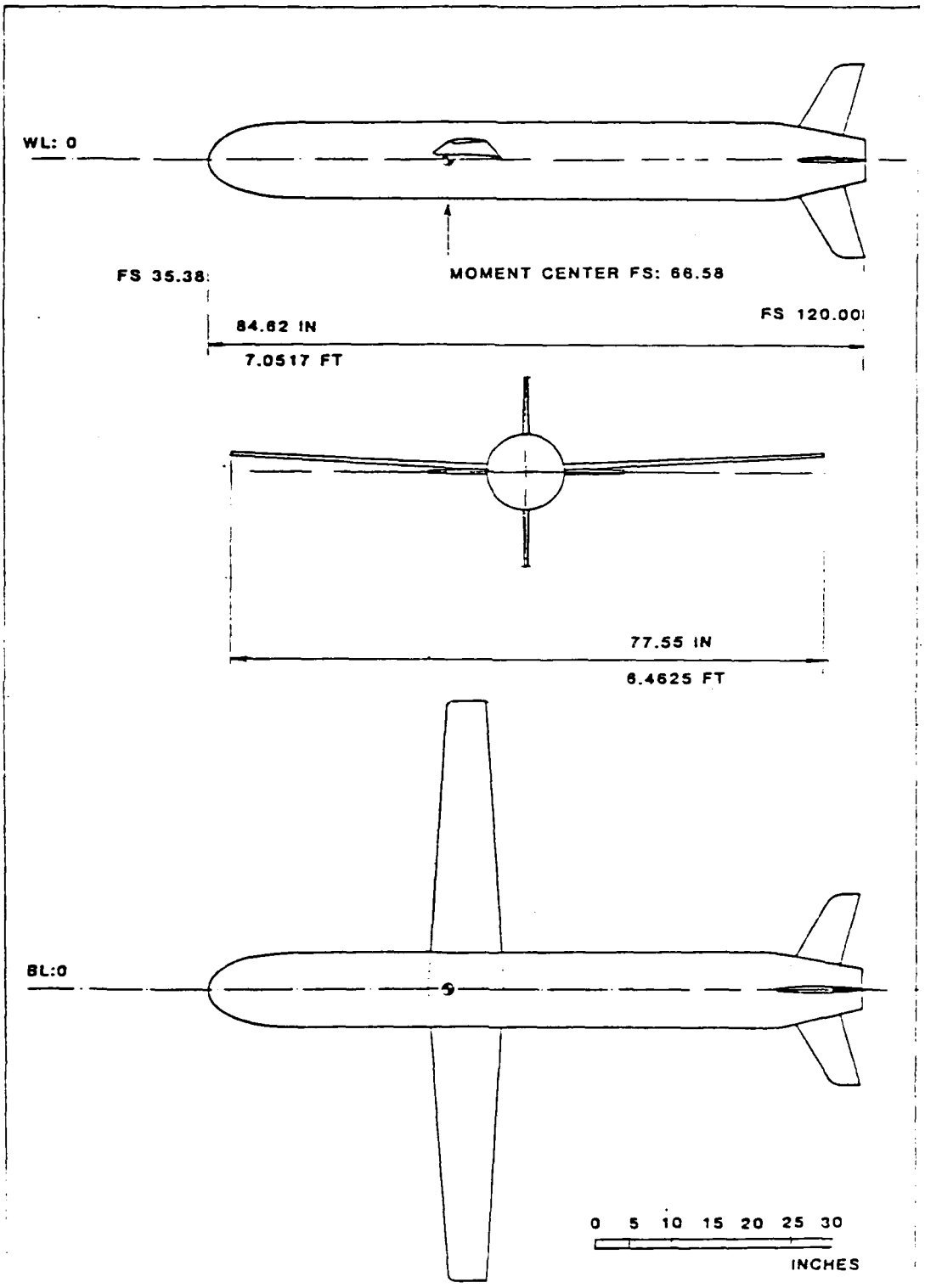

Figure 6. Baseline Configuration with Short Fuselage (Config. BWHDV)

(1) Represent an "airplane-like" configuration, rather than the cruise missile configuration of Fig. 5, so as to provide data useful for airplanes as well as missiles.

(2) Provide a baseline configuration having less fuselage drag than that of BNWHDV, thus facilitating the comparison of joined and conventional wings.

(3) Provide baseline data on fuselage length effects on stability parameters such as $\partial C_m/\partial C_L$ and C_{mo}.

Additionally, partial baseline configurations BW, BWDV, and B were tested to obtain drag build-up data.

Joined Wing Configurations

BFR: This is illustrated in Fig. 7. This represents a short-fuselage airplane-like configuration; the span and gross horizontal projected area (GHP area) of the front plus rear wings (FR) respectively equal the span and GHP area of the monoplane wing (W).

It is most important to note that the selection of equal GHP areas and spans for the configurations BW and BFR was made solely to facilitate fair comparisons of aerodynamic characteristics. When designing a practical joined wing aircraft or missile configuration the GHP area and span are selected to optimize the overall aerodynamic-plus-structural design. Therefore it would be purely coincidental if these parameters prove to be identical to the corresponding optimized parameters of a conventional configuration designed to the same specification.

BNFR: As BFR, but with a long cruise missile type fuselage identical to that employed for BNHWDV (see Fig. 8).

$BNFRC_{30}$: (See Fig. 9.) As BNFR, but with an undihedralled canard having 30^o leading edge sweep. The canard has variable incidence, pivoting about an unswept axis passing through the fuselage centerline. This configuration is one of a class of "hybrid" (i.e., joined wing plus canard) configurations discussed in Ref. 1. Such hybrid configurations are well suited for application with long fuselages, for

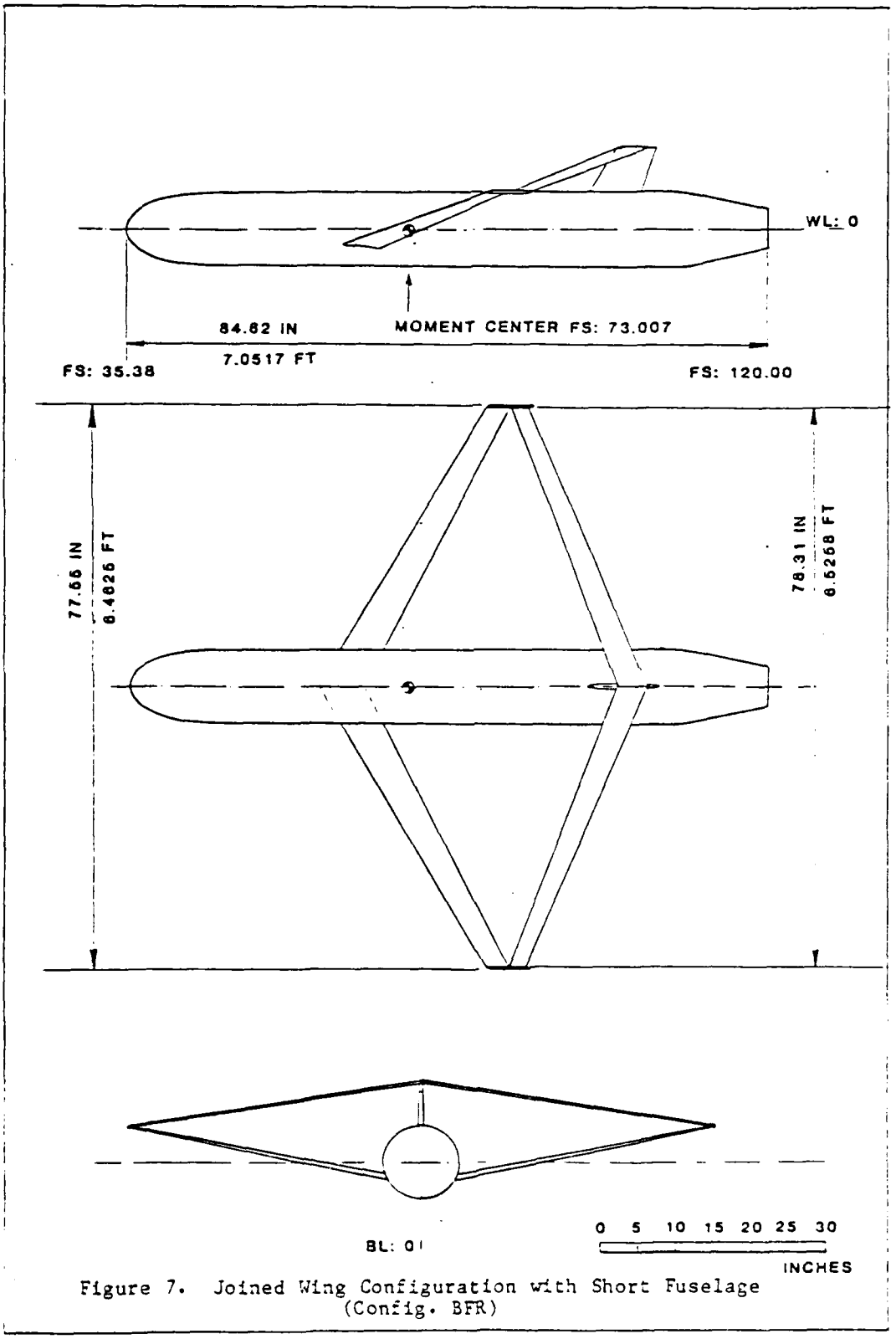

Figure 7. Joined Wing Configuration with Short Fuselage (Config. BFR)

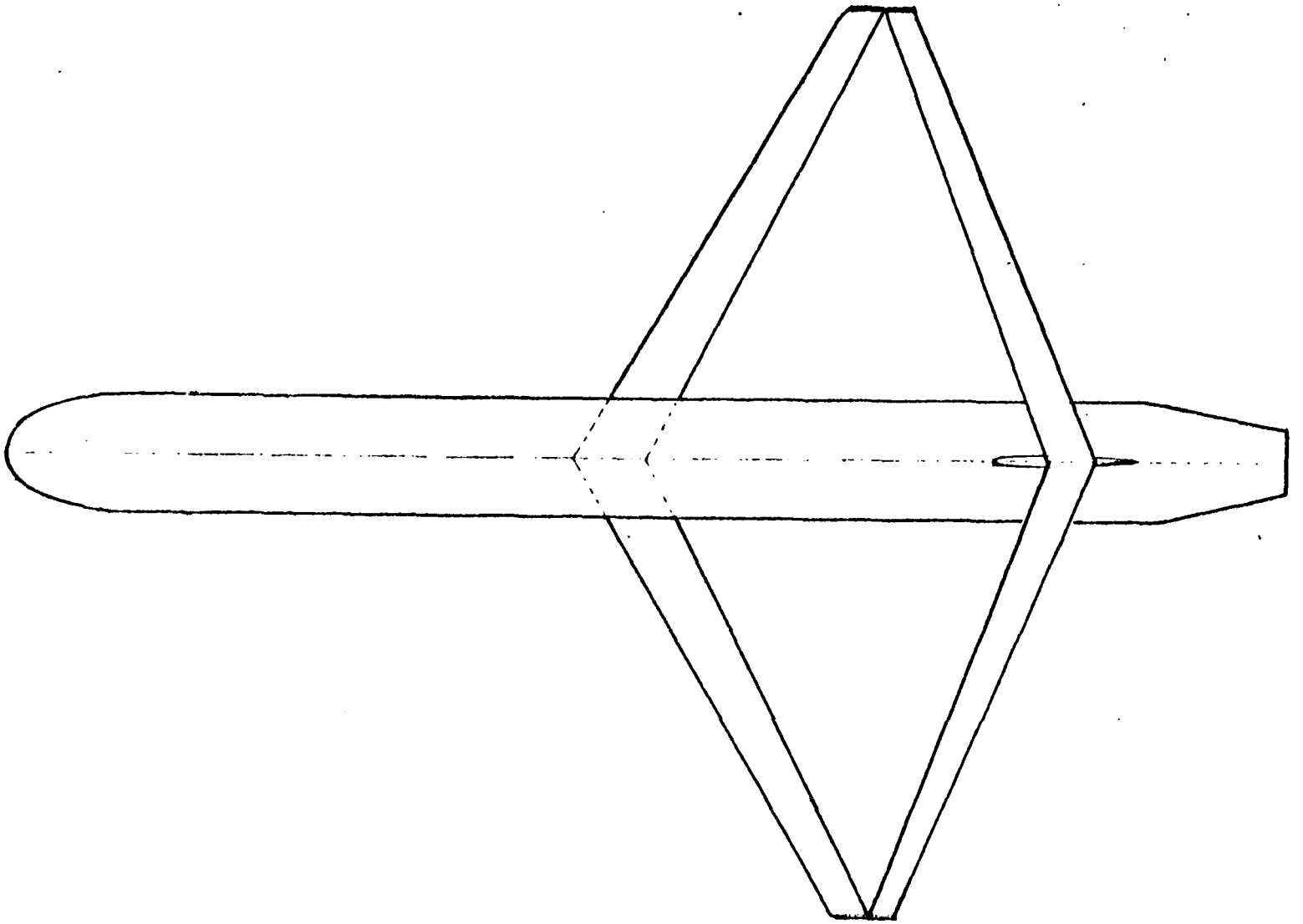

Figure 8. Joined Wing Configuration with Long Fuselage (Config. BNFR)

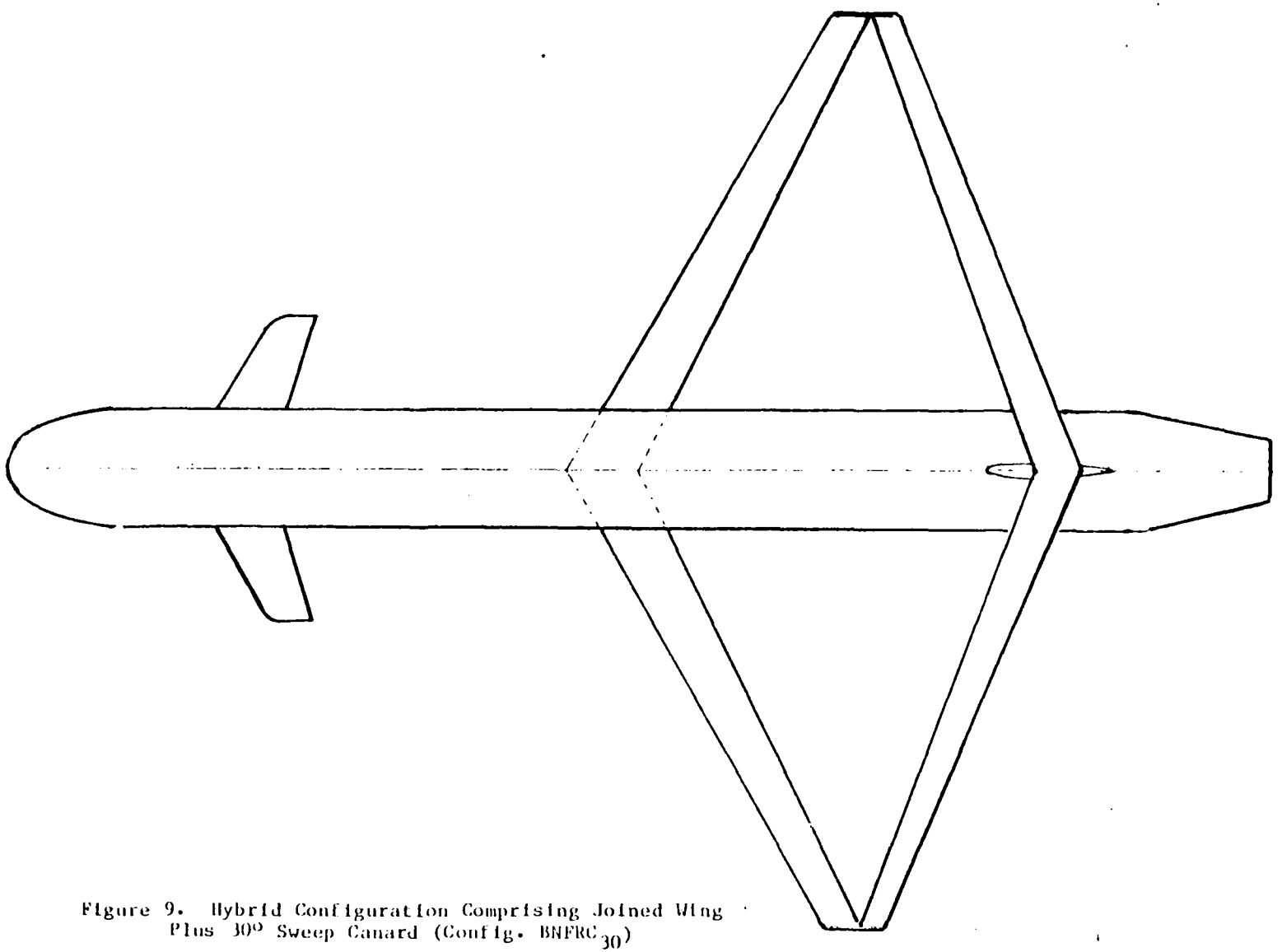

Figure 9. Hybrid Configuration Comprising Joined Wing Plus 30^{o} Sweep Canard (Config. $BNFRC_{30}$)

which the pure joined wing configuration may require excessive sweep angles on front and rear wings. One objective of testing $BNFRC_{30}$ was to determine the canard/joined wing aerodynamic interactions.

$BNFRC_{60}$: (See. Fig. 10.) As $BNFRC_{30}$ but with 60^{o} sweep on the canard leading edge.

E: Sheet metal plates added to the front joined wing as shown in Fig. 11, representing elevons. Both symmetric and anti-symmetric deflections were tested, by employing bent plates.

A: (See Fig. 11.) Sheet metal plates added to the rear joined wing to simulate ailerons. Only anti-symmetric deflections were tested.

S: (See Fig. 11.) Sheet metal plates representing strakes or leading edge extensions of the front joined wing.

The joined wing configurations described above display some features which are dictated by the cruise missile application. These include the relatively small vertical tail and low dihedral angles (≈10 deg) on both joined wings. For an aircraft application, where the wings and vertical tail are not required to fold inside the fuselage, the joined wing would generally employ dihedral angles of 15 to 20 degrees, with a consequently taller vertical tail joining the fuselage to the rear wing. Cruise missile folding constraints (in particular, the narrow fuselage) also led to the rather high aspect ratio (AR = 10.44) employed for both the conventional and joined wings. Finally, the fuselage dimensions were selected to match those of current Tomahawk cruise missiles, hence no windshield or landing gear fairings are modeled.

While the above features yield configurations that are more representative of a cruise missile than a manned aircraft, the test results are nevertheless of value for both applications. The major differences to be anticipated for an airplane-like configuration relate to the vertical tail size and dihedral angle. Increasing these would yield higher directional stability and lower induced drag.

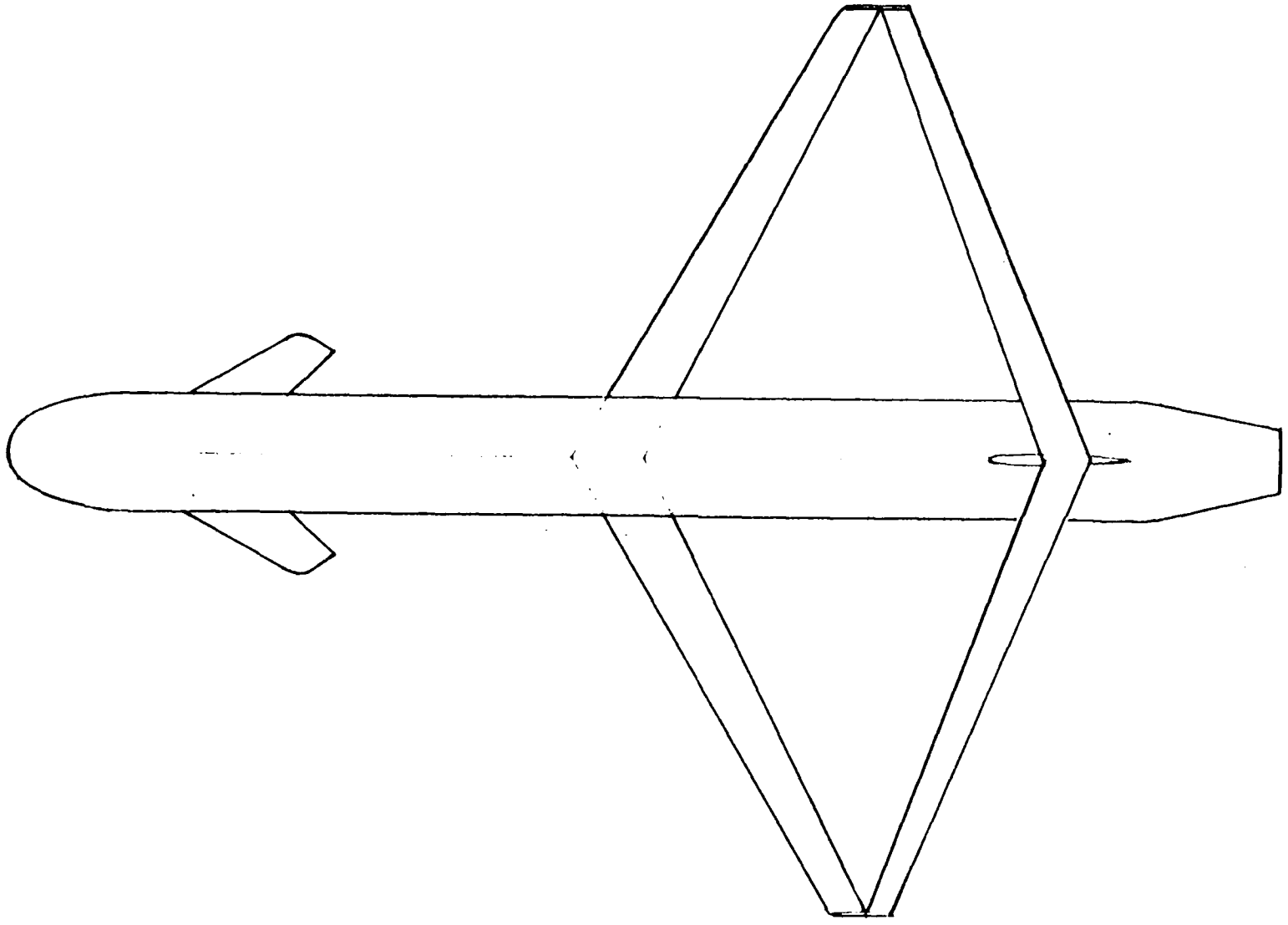

Figure 10. Hybrid Configuration Comprising Joined Wing Plus 60^{0} Sweep Canard (Config. $BNFRC_{60}$)

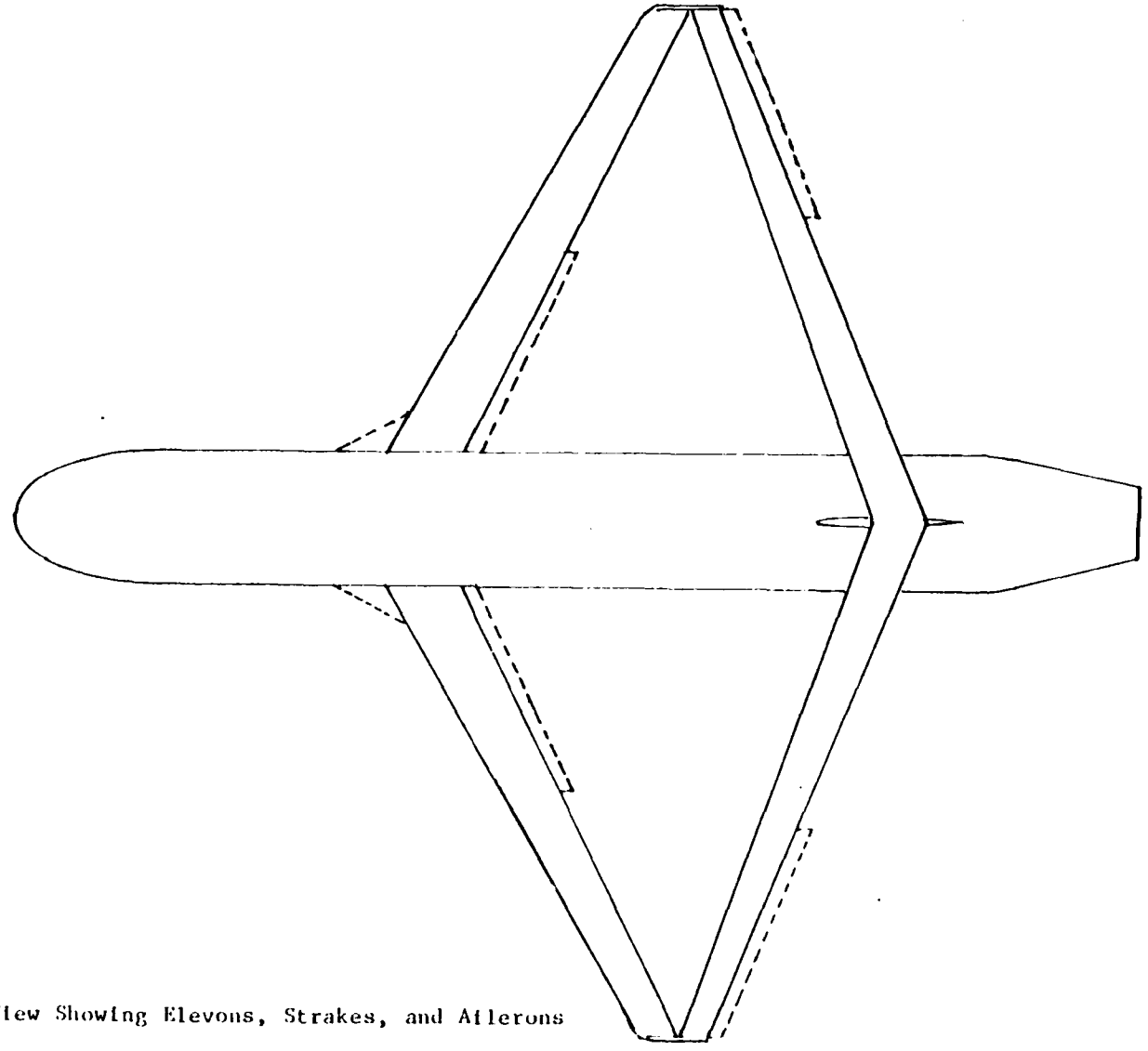

Figure 11. Plan View Showing Elevons, Strakes, and Ailerons

1.3 SELECTION OF DESIGN LIFT COEFFICIENT AND AIRFOIL DESIGN PROCEDURE

Reference 1 presents cruise missile preliminary design studies of various configurations including some closely similar to BNWHDV, BFR, $BNFRC_{30}$ and $BNFRC_{60}$. For these cruise missile designs the sea level 1 g cruise condition at mean gross weight corresponds to M = 0.7 at C_L = 0.215. As explained below, the airfoils of the joined and conventional wings were optimized for C_L = 0.645 at M = 0.20. The Mach number was reduced to correspond to the Mach number available in the 10' GALCIT wind tunnel in which the tests were performed. The C_L was increased to match the C_L required for a 3 g maneuver. The reasons for selecting this relatively high design C_L are explained below.

A major objective of the test was to determine whether the theoretically predicted induced drag advantage of joined wings over conventional wings was achieved in practice. Clearly a comparison of joined versus conventional wing induced drag requires each wing to be tested at a moderately high C_L so that the induced drag is a large fraction of the total drag. A 3 g (C_L = 0.645) condition was therefore selected rather than a 1 g (C_L = 0.215) condition as the design C_L. The 3 g condition is not necessarily the best choice for an actual cruise missile wing design. The cruise missile flies for long periods in 1 g flight and may require to pull 3 g's only for brief (but important) segments of its flight, e.g., during terrain-following and when performing terminal maneuvers. The relative importance of cruise range vs. maneuver capability will determine the wing design C_L. Optimum wing designs for practical cruise missiles may require relatively low design C_L's. Notwithstanding this, to achieve the particular test objective mentioned above a moderately high C_L must be selected, so that induced drag comparisons will not be invalidated by the effects of premature flow separation.

Airfoil Design Procedure: To obtain a fair comparison between the joined and conventional wings, the airfoils for each wing were designed by the same method, comprised of the following steps:

(1) Select a common design C_L (C_L = 0.645) and a common static margin (6 inches on the full scale configuration).

(2) Compute the optimum twist and camber of both lifting surfaces [wing + tail, or front + rear joined wings] to give minimum trimmed induced drag at the design C_L. This computation was done using the vortex-lattice program of Ref. 3.

(3) Approximate the computed optimum spanwise variation of twist and camber by linear spanwise variations, to simplify model construction. One linear variation was employed between the root and 70% of the span, a second linear variations was employed from 70% span to the tip.

(4) Fit NACA 0009 fairings around the camber lines obtained from (3).

Figures 12 and 13 illustrate the exact and approximate twist and camber spanwise variations for the joined and conventional wings. In applying the program of Ref. 3, 22 spanwise rows of horse-shoe vortices and 5 chordwise rows were employed to model the complete wing. Rooftop pressure distributions with a = 0.5 were assumed throughout.

The above procedure obviously does not reflect current airfoil design technology. More efficient airfoils could be designed by considering thickness and boundary layer effects. However the procedure has the merits of simplicity and fairness, since it is applied uniformly to both the joined and conventional wings. As with the choice of design C_L, the requirements of a fair comparative wind tunnel test differ from those of actual cruise missile aerodynamic optimization.

Fuselage Effects: The vortex-lattice procedure of Ref. 3 does not model thickness effects and therefore cannot properly compute fuselage contributions to C_{mo} and $\partial C_m/\partial C_L$. Accordingly it was decided not to include the fuselage in the vortex-lattice representations. As will be explained in Section 4, this yielded appreciable differences between predicted and measured values of C_{mo} and $\partial C_m/\partial C_L$. If fuselage effects had been included in the vortex-lattice model the airfoil shapes and particularly the relative incidences of front and rear lifting surfaces would be different from those shown in Figs. 12 and 13.

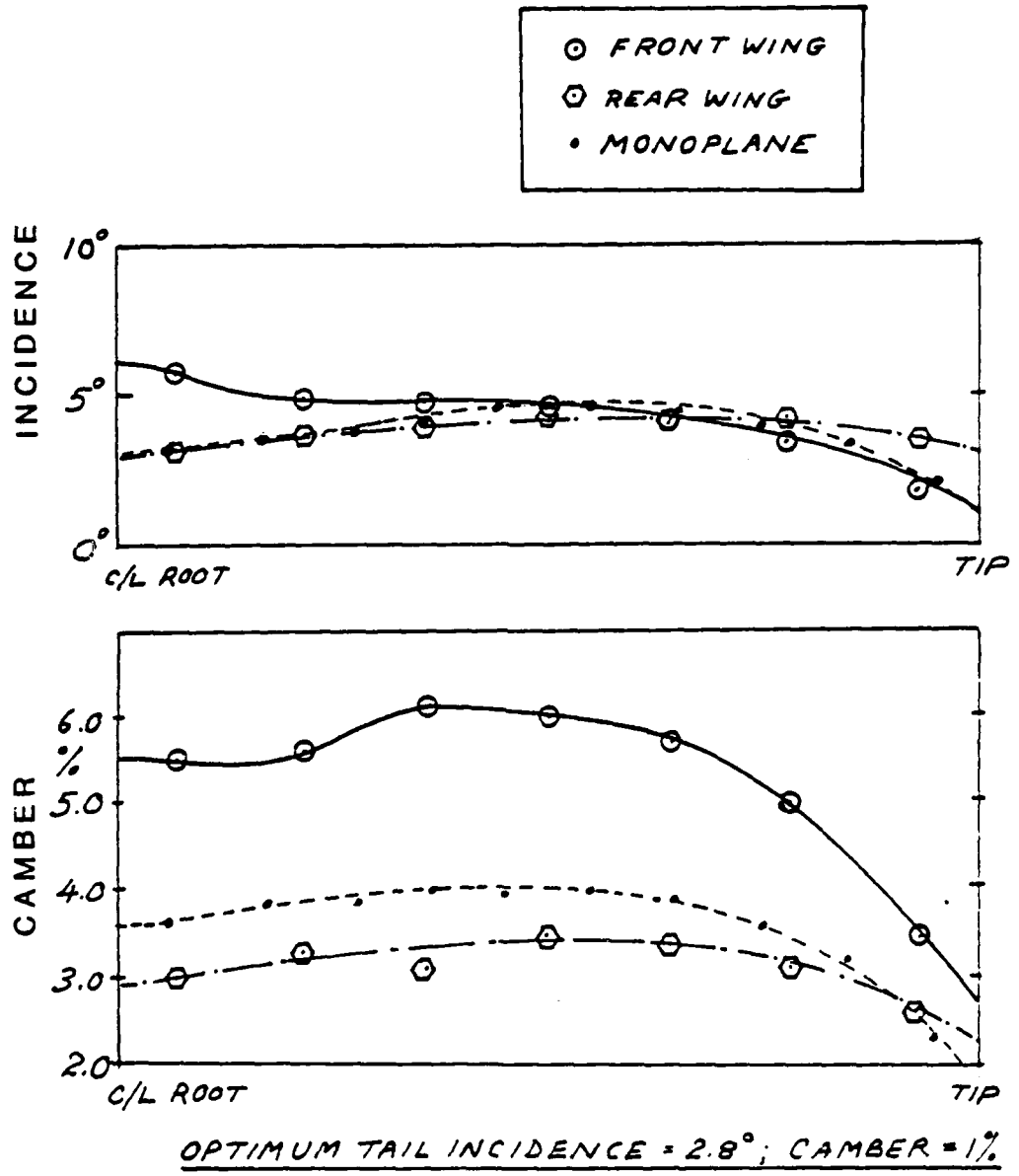

Figure 12. Optimum Twist and Camber Distributions

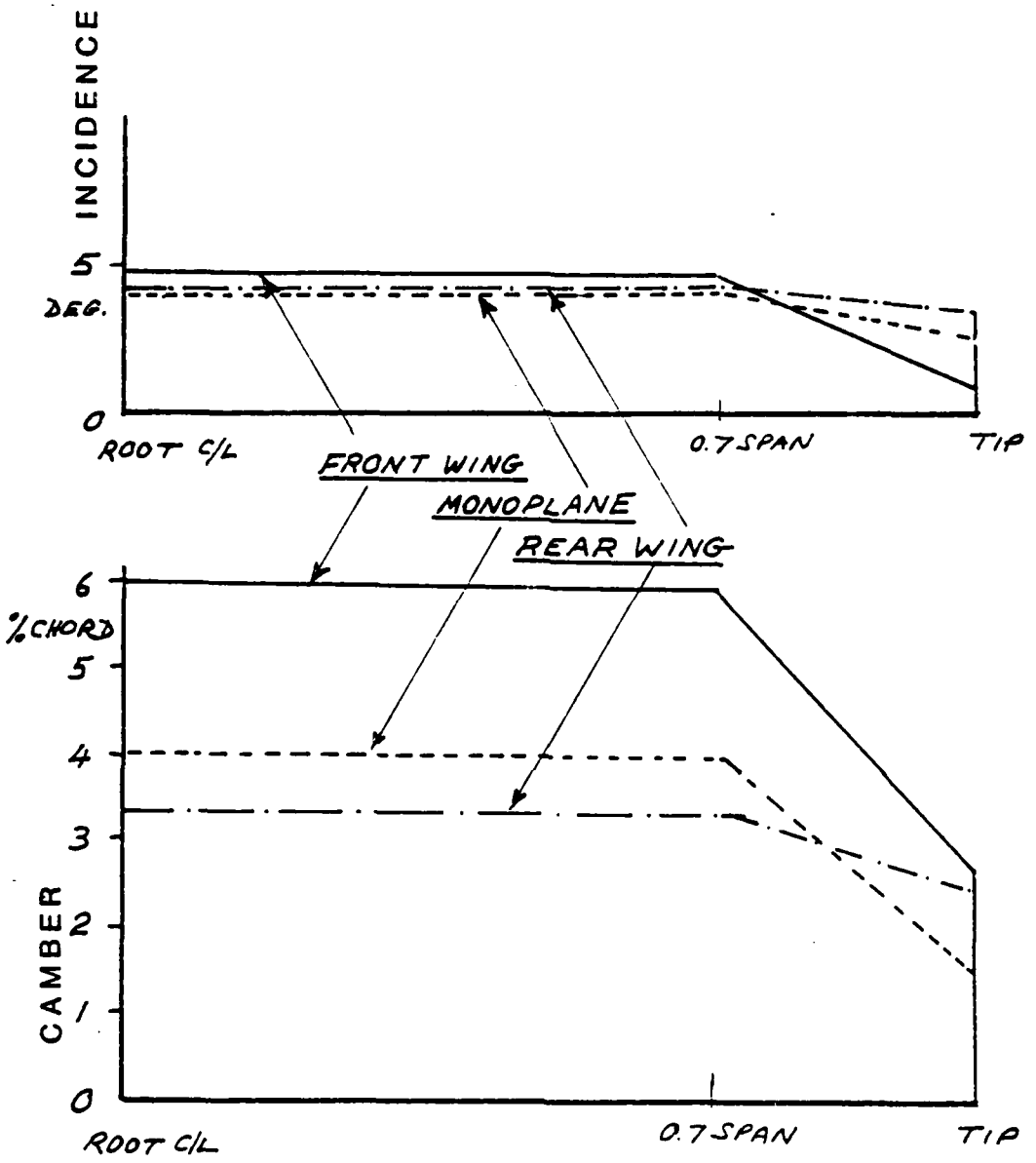

Figure 13. Approximately Optimum Twist and Camber Employed on Conventional and Joined Wing Model Components W and FR

1.4 TEST CONDITIONS

The tests were performed in the 10′ dia. GALCIT lowspeed tunnel at the California Institute of Technology. As described in Volume II, a two-point fuselage-mounted trunnion support system was employed.

Tests were conducted at dynamic pressures (q) of 3.75, 7.5, and 15.0 lb/ft^2 corresponding to tunnel speeds of 56, 79, and 112 fps, as shown in the run schedule (Table 2). Many of the joined wing tests were performed at q = 15 lb/ft^2 to facilitate comparison with monoplane tests performed at q = 3.75 lb/ft^2. This 4:1 ratio of dynamic pressures yields equal Reynolds numbers based on mean geometric chord (MGC), e.g.,

Mean Geometric Chord of Monoplane Wing (W)	0.6189 ft
Reynolds No./Ft at q = 3.75 lb/ft^2	357,264.4
Reynolds No. Based on MGC at q = 3.75 lb/ft^2	0.22×10^6
Average of Mean Geom. Chords of Front and Rear Joined Wings = (1/2) × (0.3714 + 0.2476)	0.3095 ft
Reynolds No./Ft at q = 15.0 lb/ft^2	714,528.8
Reynolds No. Based on Ave. MGC at q = 15.0 ft/ft^2	0.22×10^6

Of course, the body Reynolds numbers (based on body length) are not equal at q = 3.75 and q = 15.0 lb/ft^2, hence isolated-body test runs were performed at these q's to permit the body drag to be subtracted from the total measured drag. This is discussed fully in Section 2.

The relatively low Reynolds numbers of the tests were dictated by model strength considerations. Because of cost constraints, the wings of the conventional and joined wing configurations were fabricated from wood (maple) with no metal reinforcing spars. Such uniform (solid) construction is acceptable for cantilever wings but is badly suited to joined wings. Care was taken to force transition, and no unexpected effects of the Reynolds number limitations are apparent from the data analysis. Nevertheless, it is clear that the strength advantages of the joined wing for full-scale (hollow) wings are not obtainable with model

TABLE 2. INDEX OF RUNS

(Nomenclature defined on pages 16 through 20)

Run No.	Model Configuration	Test	q, lb/ft²	Settings, Deg.					
				α_g	ψ	i_H	i_C	δ_L	δ_R
1	BWHDV	P_6 + SP	3.75	Vary	0	0	--	--	--
2	" + T_s	"	"	"	"	"	--	--	--
3	" + "	" + SP	7.50	"	"	"	--	--	--
4	" + "	Y_6	"	0	Vary	"	--	--	--
5	" + "	" + SP	"	10	"	"	--	--	--
6	" + "	P_3	"	Vary	0	10	--	--	--
7	" + "	"	"	"	"	-10	--	--	--
8	BNWHDV + "	" + SP	"	"	"	0	--	--	--
9	" + "	Y_6	"	0	Vary	"	--	--	--
10	" + "	"	"	10	"	"	--	--	--
11	BWDV + "	P_3	"	Vary	0	--	--	--	--
12	BW + "	"	"	"	"	--	--	--	--
13	" + "	"	3.75	"	"	--	--	--	--
14	B + "	" + SP	7.50	"	"	--	--	--	--
15	" + "	"	3.75	"	"	--	--	--	--
16	" + "	" + SP	15.00	"	"	--	--	--	--
17	BFR + T_{s_1}	"	"	"	"	--	--	--	--
18	" + T_s	"	"	"	"	--	--	--	--
19	" + T_{s_2}	" + SP	"	"	"	--	--	--	--
20	" + "	"	7.50	"	"	--	--	--	--
21	" + "	Y_6	15.00	0	Vary	--	--	--	--
22	" + "	"	"	5	"	--	--	--	--
23	" + " + Tufts	TP	7.50	Vary	"	--	--	--	--

TABLE 2.
INDEX OF RUNS (CONT'D.)

Run No.	Model Configuration	Test	q, lb/ft²	Settings, Deg.					
				α_g	ψ	i_H	i_C	δ_L	δ_R
24	BNFR + T_{s_2}	P_6	15.00	Vary	0	--	--	--	--
25	" + "	Y_6	"	0	Vary	--	--	--	--
26	" + "	"	"	5	"	--	--	--	--
27	$BNFRC_{30}$ + "	P_3	"	Vary	0	--	0	--	--
28	" + "	Y_6	"	0	Vary	--	"	--	--
29	" + "	"	"	5	"	--	"	--	--
30	" + "	P_3	"	Vary	0	--	10	--	--
31	" + "	"	"	"	"	--	-5	--	--
32	$BNFRC_{60}$ + "	"	"	"	"	--	0	--	--
33	" + "	"	"	"	"	--	10	--	--
34	" + "	"	"	"	"	--	-5	--	--
35	" + "	"	7.50	"	"	--	0	--	--
36	BFR + T_{s_3}	"	15.00	"	"	--	--	--	--
37	BFRS + T_{s_2}	"	"	"	"	--	--	--	--
38	" + "	Y_6	"	5	Vary	--	--	--	--
39	BFRSE + "	P_3	"	Vary	0	--	--	-10	-10
40	" + "	"	"	"	"	--	--	10	"
41	" + "	"	"	"	"	--	--	"	10
42	" + "	"	"	"	"	--	--	-10	"
43	" + "	"	"	"	"	--	--	0	0
44	" + "	P_6	"	"	"	--	--	10	-10
45	" + "	"	"	"	"	--	--	-10	10
46	BFRSA + "	"	"	"	"	--	--	10	-10

TABLE 2. (CONCLUDED)

Run No.	Model Configuration	Test	q, lb/ft^2	Settings, Deg.					
				α_g	ψ	i_H	i_C	δ_L	δ_R
47	BFRSA + T_{S_2}	P_6	15.00	Vary	0	--	--	-10	10
48	" + "	P_3	"	"	"	--	--	0	0
49	BFRS + "	"	7.50	"	"	--	--	--	--
50	" + "	SP	"	"	"	--	--	--	--
51	" + "	TW	4.00	"	"	--	--	--	--
52	$BNFRSC_{60}$ + "	"	"	"	"	--	0	--	--
53	" + "	P_3	7.50	"	"	--	"	--	--
54	$BNFRSC_{30}$ + "	TW	4.00	"	"	--	"	--	--
55	" + "	P_3	7.50	"	"	--	"	--	--
56	BFR	"	"	"	"	--	--	--	--

wings made of solid, uniform material. This effect may be important for future joined wing tunnel tests, particularly tests at high Mach numbers. Therefore a full discussion of the effect is given in Appendix A.

1.5 ORGANIZATION OF THE MAIN TEXT OF THIS REPORT

Section 2 analyzes the drag data, with particular reference to validating the predicted induced drag advantage of joined wings over monoplane wings. Comparisons of predicted and measured parasite drag are also given.

Section 3 analyzes the measured lift characteristics, particularly C_{Lmax}.

Section 4 presents an analysis of the trim and pitching moment characteristics and a comparison with the characteristics predicted by vortex-lattice methods. Elevon effectiveness is also analyzed. The effect of trim on drag and C_{Lmax} is also discussed in Section 4.

Section 5 presents analyses of lateral stability and control characteristics.

Conclusions and recommendations for further work are given in Section 6.

Appendix A discusses structural aspects of joined wing wind tunnel models.

2.0 DRAG ANALYSIS

2.1 ORGANIZATION OF THIS SECTION

This section first shows that the variation of C_D with C_L for all the configurations tested closely fits an equation of the "offset drag polar" form

$$C_D = C_{Dmin} + \frac{(C_L - C_{Lx})^2}{\pi A e_x} \quad (1)$$

where C_{Dmin}, e_x, C_{Lx} are constants; whereas the "non-offset" form, Eq. 2,

$$C_D = C_{Dmin} + \frac{C_L^2}{\pi A e} \quad (2)$$

only fits to the data if extremely large variations of e with C_L are permitted.

Next, the minimum drag coefficient of the principal configurations tested is compared with theoretical predictions based on skin friction calculations. It is shown that, for the joined wing configurations, C_{Dmin} is slightly higher than predicted by skin friction considerations. The increment in C_{Dmin} is shown to be related to the offset of the drag polar, i.e., the parameter C_{Lx} in Eq. 1, and it is postulated that it is related to the component of induced drag which exists for twisted wings at zero total C_L. It is shown that, with the C_{Dmin} increment included, the theoretically predicted induced drag advantage of the joined wing is attained or surpassed over the C_L range of most interest.

2.2 SPAN-EFFICIENCY FACTOR COMPARISONS

Figure 14 compares $C_D - C_{Dmin}$ versus C_L for representative conventional and joined wing configurations BW and BFR respectively, operating at the same average wing Reynolds number.* Figure 15(a) shows the span-efficiency factor obtained by fitting Eq. 2 to the data of Fig. 14.

*The effects of the transition strips T_s, T_{s2}, are discussed later (p. 53).

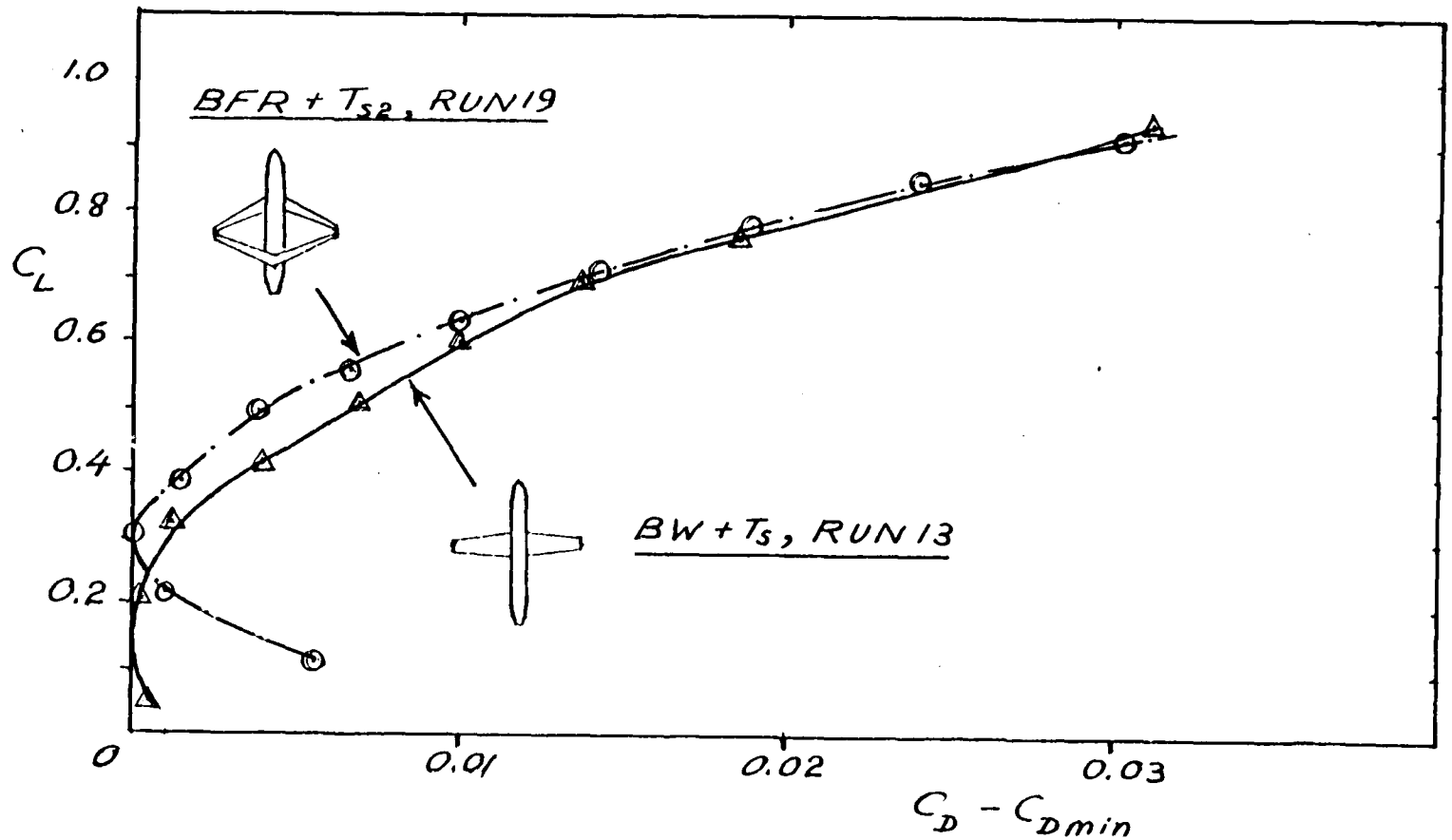

Figure 14. Coefficient of Lift-Dependent Drag, $C_D - C_{Dmin}$, Versus C_L

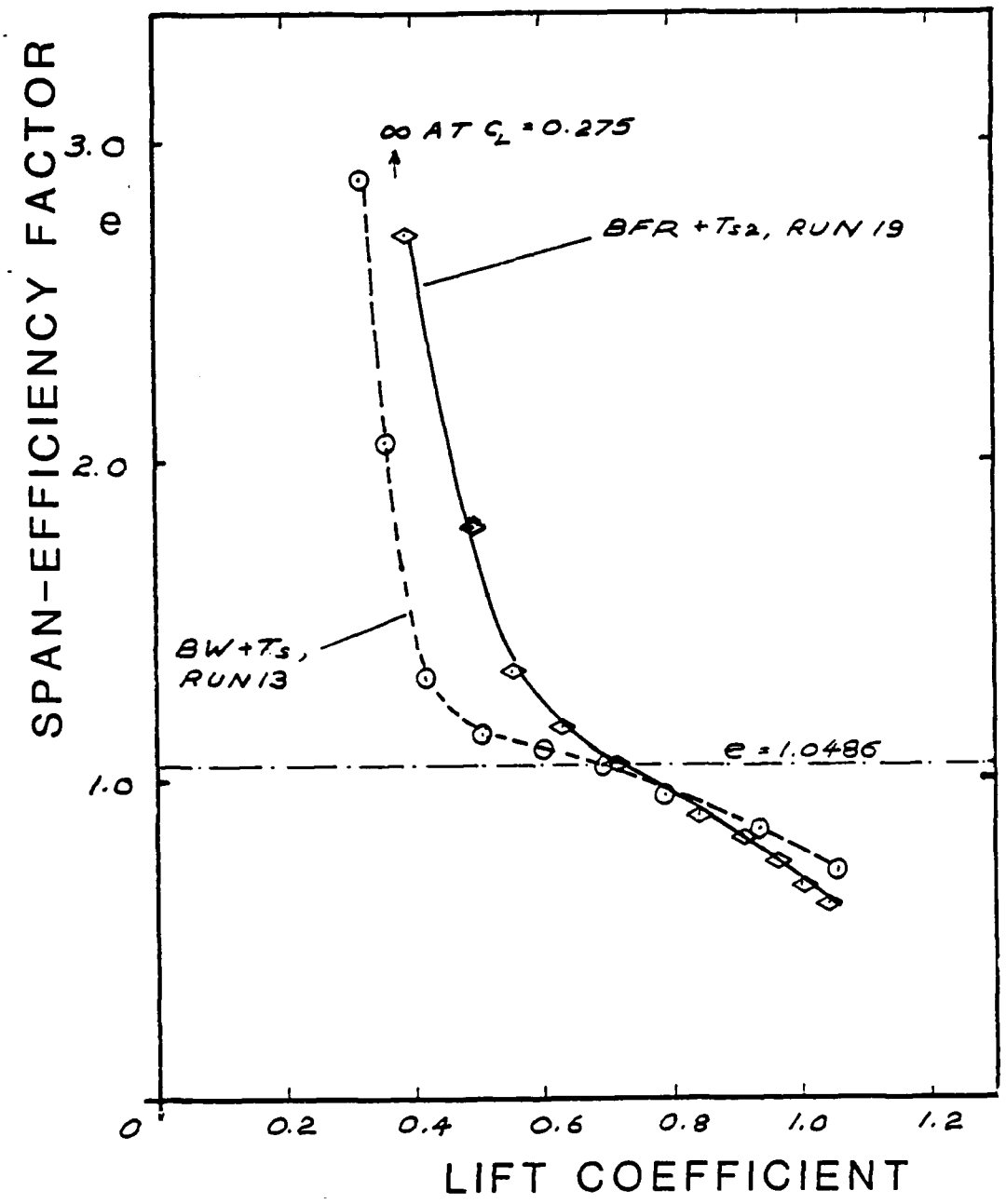

Figure 15 (a). Span-Efficiency Factor Comparison, Joined Wing Vs. "Tail-Off" Monoplane

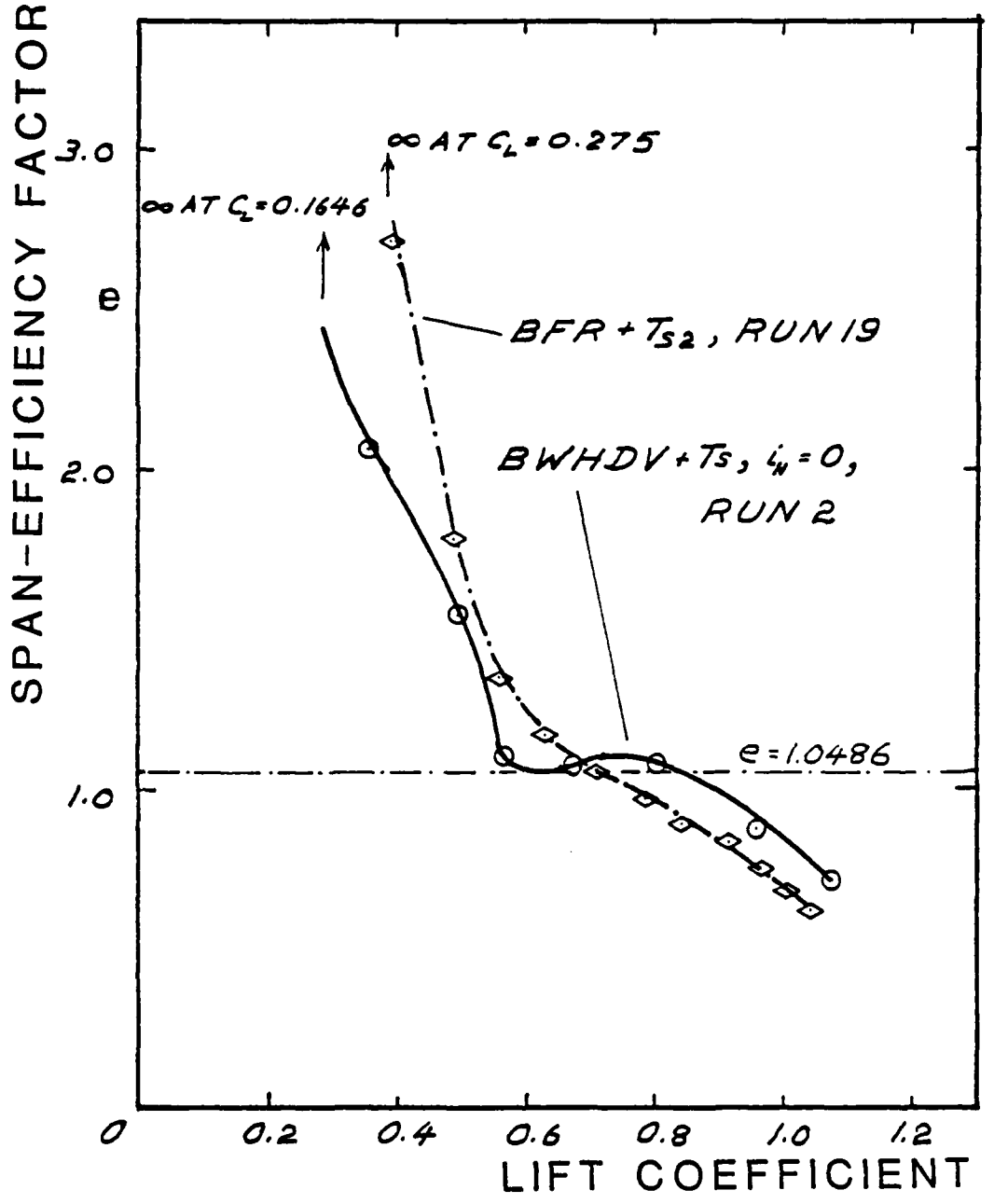

Figure 15 (b). Span-Efficiency Factor Comparison, Joined Wing Vs. "Tail-On" Monoplane

By allowing the span-efficiency factor, e, to vary with C_L, Eq. 1 can be fitted to the measured C_D vs. C_L data. Figures 15(a) and 15(b) illustrate the resulting variation of e with C_L for $C_L > C_{Lx}$, where C_{Lx} is the C_L for minimum C_D. Figure 15(b) compares the joined wing configuration versus a conventional "tail-on" baseline configuration, while in Fig. 15(a) the baseline configuration is "tail-off." For each of these figures the Reynolds number based on mean geometric chord (MGC) of the monoplane equals the average of the Reynolds numbers of the front and rear joined wings based on their individual MGC's.

For purposes of computing the e variations shown in Figs. 15(a) and 15(b), the spans of the joined and monoplane wings were both taken as 6.4625 ft, giving equal aspect ratios A = 10.4415. If the tip joint member is included in the span of the joined wing its span increases to 6.5258 ft, giving A = 10.6470. Using this basis the joined wing e values shown in Figs. 15(a) and 15(b) would be reduced by a factor of $(6.4625/6.5258)^2 = 0.9807$, i.e., a reduction of 1.93%. As shown by the results graphed on Figs. 14, 15(a) and 15(b), whichever e is selected, it is clear that at low and moderate C_L's (e.g., below $C_L \approx 0.7$) the span-efficiency factor is higher for the joined wing.

Letcher (Ref. 4) has calculated exact theoretical span-efficiency factors for optimally loaded wings forming a diamond-shaped front view. This class includes the joined wing, since by Munk's stagger theorem the optimum e is unaffected by sweep, provided that the twist and camber are optimized. Letcher's exact result has been verified by a numerical optimization procedure described by Kuhlman in Ref. 5. Figure 15(c) is a reproduction of Kuhlman's Fig. 4 which illustrates this verification.

The present configuration employs dihedral angles of +10.8 degrees (front wing) and -9.2 degrees (rear wing). Taking a mean dihedral angle of 10 degrees, Letcher's results yield an exact theoretical span-efficiency factor e = 1.0486.

From the line at e = 1.0486 shown in Figs. 15(a) and 15(b) one could conclude that the joined wing attains (or slightly exceeds) its theoretically predicted induced drag reduction at the design C_L, that

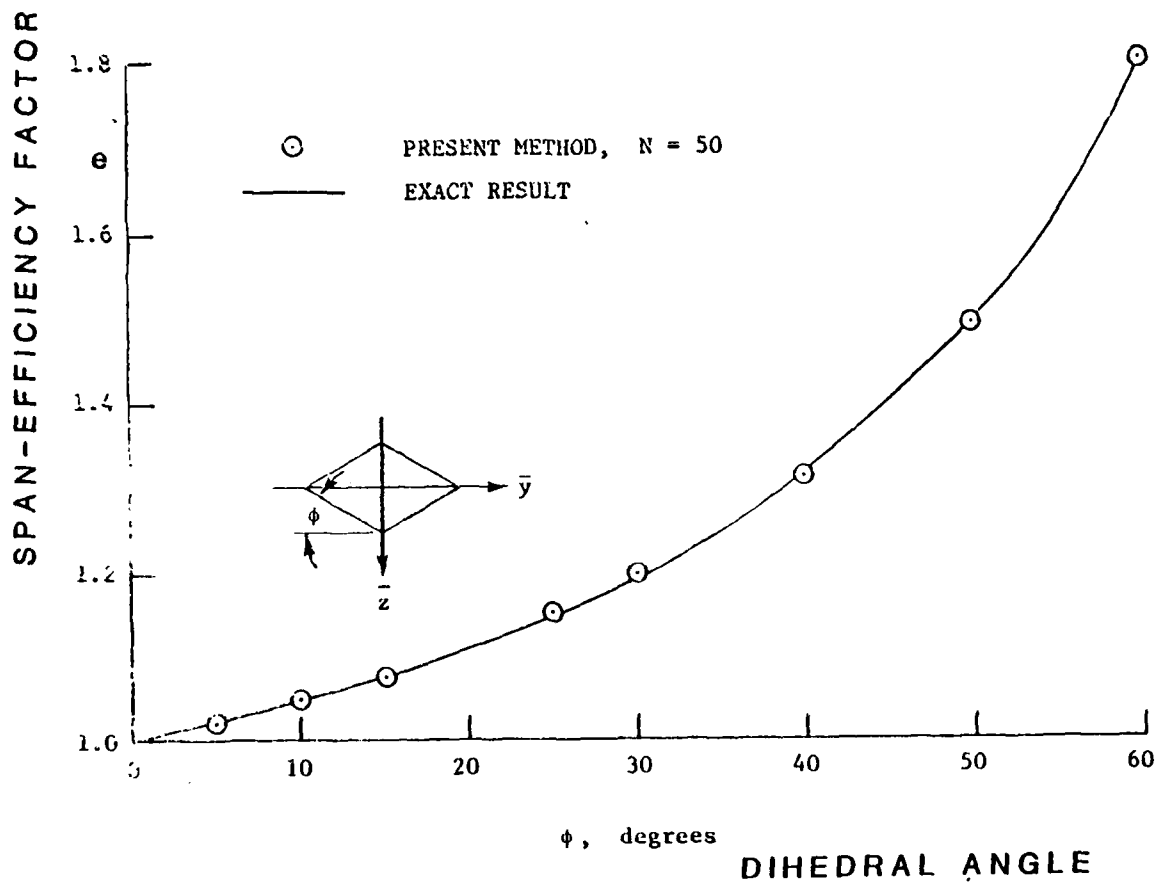

Figure 15 (c). Theoretical Span-Efficiency Factor for Diamond Wings (from Ref. 5)

below the design C_L the induced drag reduction is greater than predicted, and that at high C_L's the induced drag of the joined wing is greater than that of the monoplane. However this conclusion, while not incorrect, ignores some important questions. For example:

1. Are the C_{Dmin} values comparable for both the joined wing and conventional configurations?

2. What effect, if any, do the transition strips have on the variation of C_D versus C_L?

3. Can the large variations in e be avoided by curve-fitting the data with Eq. 1, instead of Eq. 2?

Question 1 is particularly important, since it would be disadvantageous to the joined wing if its apparent gain in e were counterbalanced by a large increase in C_{Dmin}. This question cannot be answered by comparing the measured values of C_{Dmin} of runs made at the same wing Reynolds numbers, because the fuselage Reynolds numbers differ by a factor of 2:1 stemming from the 4:1 ratio of dynamic pressures required to yield the equal wing Reynolds numbers.

Section 2.4 addresses Question 2 in detail by comparing theoretical versus measured C_{Dmin} values for components and complete configurations. First, however, Question 3 will be studied in Section 2.3.

2.3 DETERMINATION OF e_x AND C_{Lx}

Figures 16 and 17 graph the C_D and C_L data graphed in Figs. 14 and 15 in an alternative form, i.e., $\sqrt{C_D - C_{Dmin}}$ versus C_L. Inspection of Figs. 16 and 17 shows that, for the configurations BFR (Run 19) and BW (Run 13), Eq. 1 provides a close fit to the measured data for C_L's below those at which large-scale separation occurs. Table 3 generalizes this curve-fitting process by presenting e_x and C_{Lx} values computed for all the tested configurations for which drag polars were measured.

Table 3 illustrates the results of least-squares curve-fits, fitting equations of the form:

$$y' = bx' + a \qquad (3)$$

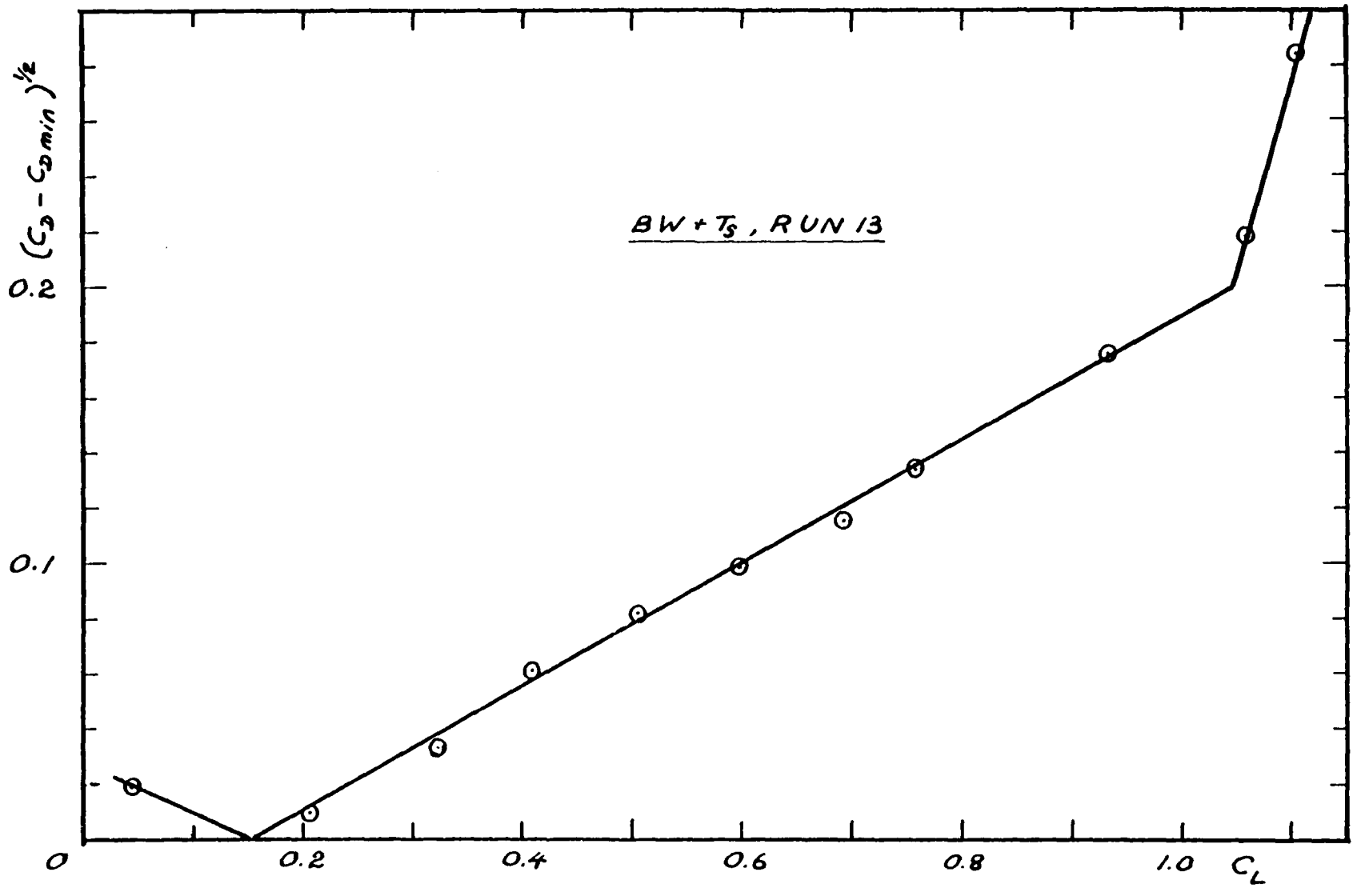

Figure 16. $(C_D - C_{Dmin})^{1/2}$ Versus C_L for Tail-Off Monoplane Configuration

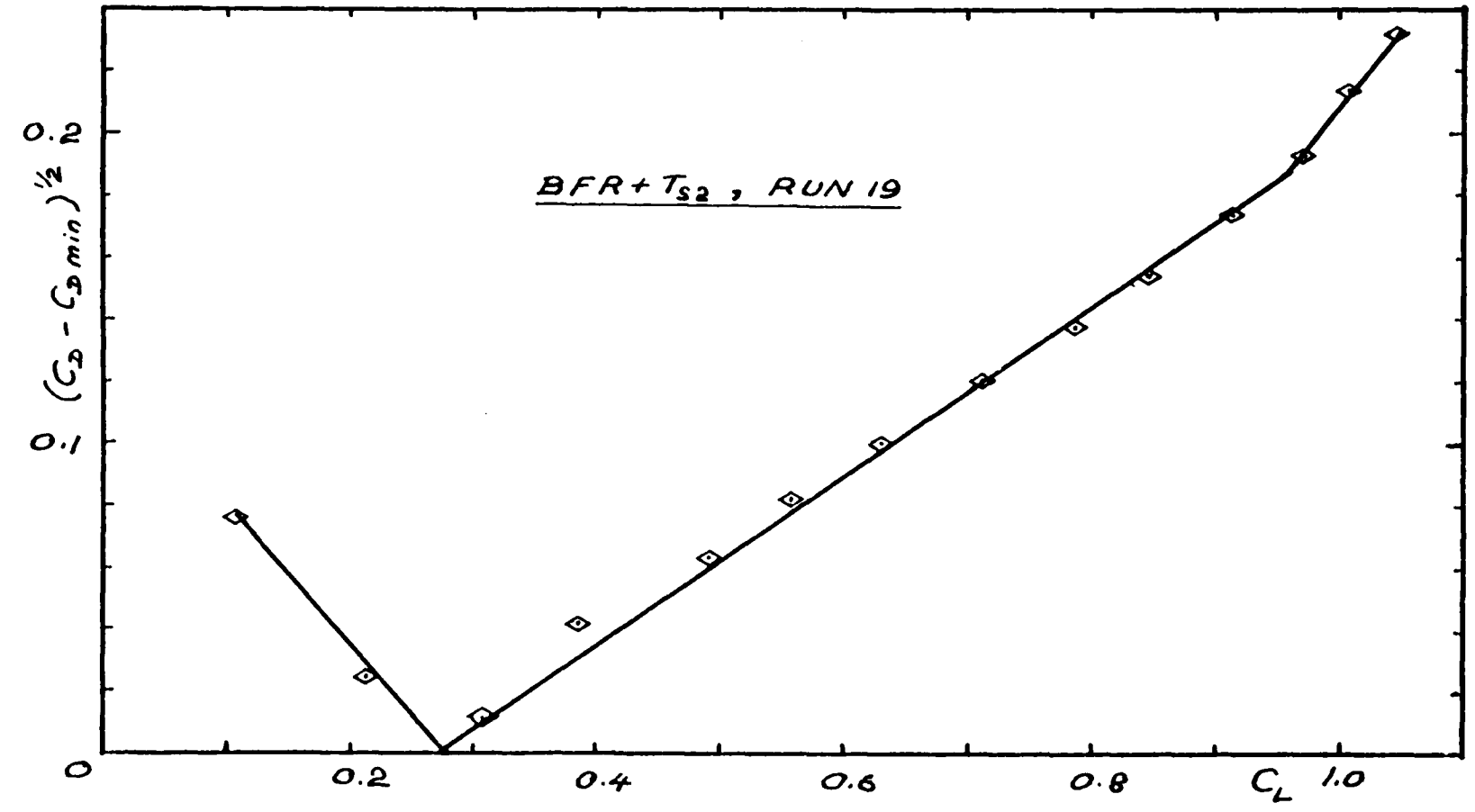

Figure 17. $(C_D - C_{Dmin})^{1/2}$ Versus C_L for Joined Wing Configuration

TABLE 3. CALCULATED VALUES OF e_x AND C_{Lx}

Run No.	Configuration	Dynamic Pressure (lb/ft^2)	b′	a	R	e_x	C_{Lx}	No. of Data Points
1	BWHDV, $i_H = 0$	3.75	0.0812	0.00035	0.6440	0.3755	0.290	4
2	" + T_s, $i_H = 0$	3.75	0.0506	-0.00009	0.9962	0.6026	0.1646	6
3	" + " , $i_H = 0$	7.5	0.0468	-0.00015	0.9991	0.6515	0.170	7
6	" + " , $i_H = 10$	7.5	0.0503	0.00094	0.9941	0.6061	0.125	5
7	" + " , $i_H = -10$	7.5	0.0258	0.00025	0.9715	1.1818	0.415	3
8	BNWHDV + " , $i_H = 0$	7.5	0.0548	0.00111	0.9897	0.5564	0.220	5
11	BWDV + "	7.5	0.0398	-0.0006	1.0000	0.7661	0.090	2
12	BW + "	7.5	0.0380	-0.00105	0.9976	0.8024	0.050	6
13	" + "	3.75	0.0467	0.00025	0.9954	0.6523	0.150	6
17	BFR + T_{s1}	15.0	0.0681	-0.00007	0.9999	0.4477	0.3425	5
18	" + T_s	15.0	0.0764	0.00051	0.9997	0.3991	0.275	6
19	" + T_{s2}	15.0	0.0786	0.00043	0.9981	0.3881	0.275	5
20	" + "	7.5	0.0812	0.00013	1.0000	0.3756	0.300	2
24	BNFR + T_{s2}	15.0	0.0765	-0.00073	1.0000	0.3986	0.275	2
27	$BNFRC_{30}$ + T_{s2}, $i_C = 0$	15.0	0.0694	0.00037	1.0000	0.4391	0.250	2
30	" + " , $i_C = 10$	15.0	0.0877	0.00004	1.0000	0.3477	0.330	2
31	" + " , $i_C = -5$	15.0	0.0595	0.00020	1.0000	0.5124	0.230	2
32	$BNFRC_{60}$ + T_{s2}, $i_C = 0$	15.0	0.0818	-0.00019	1.0000	0.3726	0.300	2
33	" + " , $i_C = 10$	15.0	0.0966	-0.00027	1.0000	0.3157	0.330	2
34	" + " , $i_C = -5$	15.0	0.07631	0.00001	1.0000	0.3996	0.300	2
35	" + " , $i_C = 0$	7.5	0.0983	0.00007	1.0000	0.3103	0.300	2
36	BFR + T_{s3}	15.0	0.0791	0.00018	0.9990	0.3855	0.315	5
37	" + T_{s2}	15.0	0.08729	0.00015	1.0000	0.3493	0.325	2
39	BFRSE + T_{s2}, $\delta_E = -10$	15.0	0.07338	0.00000	1.0000	0.4155	0.2616	2
41	" + " , $\delta_E = 10$	15.0	0.03171	0.00000	1.0000	0.9616	0.2410	2
43	" + " , $\delta_E = 0$	15.0	0.13894	0.00000	1.0000	0.2194	0.3968	2
49	BFRS + T_{s2}	7.5	0.0832	0.0001	1.0000	0.3667	0.300	2
56	BFR	7.5	0.09856	0.00032	1.0000	0.3094	0.320	2

to measured data expressed as

$$(C_D - C_{Dmin}) = \frac{(C_L - C_{Lx})^2}{\pi \times 10.4415 \times e_x} \tag{4}$$

Only data for $C_{Lx} < C_L < 0.7$ were employed, to avoid the separated flow regimes. The quantity R given in Table 3 is a measure of the closeness with which Eq. 4 fits the data. R is a correlation coefficient defined from:

$$R^2 = \frac{\left[\Sigma xy - \frac{(\Sigma x \, \Sigma y)}{n}\right]^2}{\left[\Sigma x^2 - \frac{(\Sigma x)^2}{n}\right]\left[\Sigma y^2 - \frac{(\Sigma y)^2}{n}\right]} \tag{5}$$

where

n = Number of points

$y = C_D - C_{Dmin}$

$x = (C_L - C_{Lx})^2$

for a perfect curve-fit R = 1.0.

The most significant data in Table 3 are those taken in runs for which the number of data points was large ($n \geq 5$). For n = 2 the curve-fitting process yields R = 1 automatically, and R loses its significance. With this proviso it is found that (except for Run 1) the values of R are close to unity throughout, indicating that the drag data are closely fitted by Eq. 4. (Run 1 was performed without transition strips and the graphed data of Volume II indicates that a laminar bucket was formed.)

Figure 18 graphs the values of e_x and C_{Lx} from Table 3. With the exception of Runs 7 and 41 (discussed below) there is remarkably little scatter in the data. A suggested single empirical curve-fit valid for conventional configuration (tail-on and tail-off), joined wing and hybrid configurations is

$$e_x = 0.90 - 1.70 \, C_{Lx} \tag{6}$$

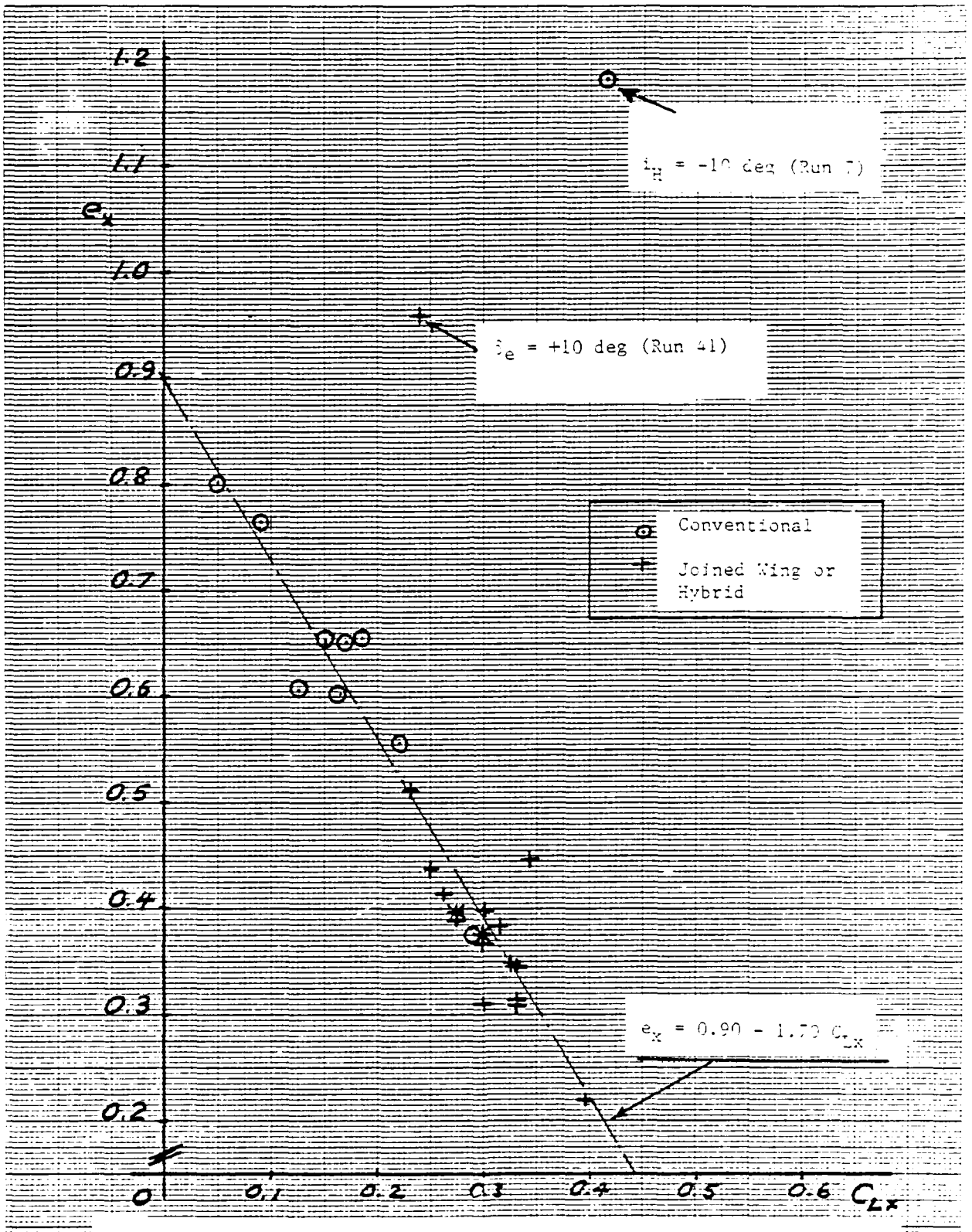

Figure 18. Results of Curve-Fit Analysis: e_x Vs. C_{Lx}

The divergent points for Runs 7 and 41 are both associated with large applied nose-up pitching moments, due to canard incidence (Run 41) or horizontal tail setting (Run 7). The mild divergence of some other runs may be a consequence of the small number of data points available for the runs in the prescribed C_L range ($C_{Lx} < C_L < 0.7$).

Figure 18 indicates that the joined wing and hybrid configurations yield higher C_{Lx} values but lower e_x values than the tail-on and tail-off conventional configurations. This observation must be interpreted carefully. It must not be inferred that a high value of C_{Lx} indicates that, when operating at $C_L = C_{Lx}$ the configuration has zero induced drag. On the contrary, the measured C_{Dmin} may contain an appreciable induced drag component. This component must be determined for both the joined and conventional wings in order to complete the induced drag comparison. The following subsection describes how this component is found.

2.4 PROCEDURE FOR ANALYSIS OF C_{Dmin}

Direct comparison of the measured C_{Dmin} values for each complete configuration tested is of little value for reaching general conclusions regarding the relative drag of joined and conventional wings. This is because each configuration contains components having different wetted areas operating at different Reynolds numbers. For example, at q = 3.75 and q = 15.0 the average Reynolds numbers of the joined and monoplane wings are similar, but the fuselage Reynolds numbers are in a 2:1 ratio. Furthermore, the wetted area of the joined wing employed here is larger than that of the monoplane wing, because of dihedral and fuselage shielding.

An alternative approach, employed below, is to compare the measured drag of each configuration versus the drag predicted by a standard procedure. This method, described in such texts as Refs. 6 and 7, employs the equation:

$$C_{Dmin} = k \times \frac{1}{S} \times \Sigma\, C_{fn} \times S_{wet,n} \times F_n \qquad (7)$$

where

S	Reference area for C_D
$S_{wet,n}$	Wetted area of nth component of the vehicle
C_{fn}	Flat plate skin friction coefficient of nth component
F_n	Form factor of nth component, defined as the ratio of the experimentally determined drag of that component in isolation to the product $C_f S_{wet} q$ for that component, where q = dynamic pressure
k	A factor applied to account for drag due to leaks and interference
Σ	Denotes a summation of the contributions of all components of the vehicle

For present purposes it is convenient to put $k = 1.0$, and to adjust F_n to match the measured C_{Dmin}. Then, by comparing the resulting F_n values for joined versus conventional configurations, a fair comparison can be made of minimum drag characteristics, including the induced drag component of C_{Dmin}. The comparison is fair because the joined and conventional wings tested have identical thickness/chord ratios and similar amounts of camber (taking the average of front and rear wing cambers for the joined wing pair). Comparing the joined wing data for $q = 15.0$ lb/ft^2 with the monoplane data for $q = 3.75$ lb/ft^2 assures equal average wing Reynolds numbers.

Some minor complications arise because of the effects of fuselage drag, wing taper, tail surfaces and transition strips. These points are explained below.

Fuselage Drag. To apply Eq. 7 to comparisons of wings it is necessary to remove the fuselage drag. This is done by subtracting the isolated-fuselage C_D at the angle of attack, α_x, corresponding to C_{Lx} of the complete configuration tested. The isolated-fuselage C_D's for the appropriate dynamic pressure are obtained from Runs 14, 15, and 16, and are graphed on Fig. 19. Table 4 lists the body-off C_D's calculated by this subtractive procedure.

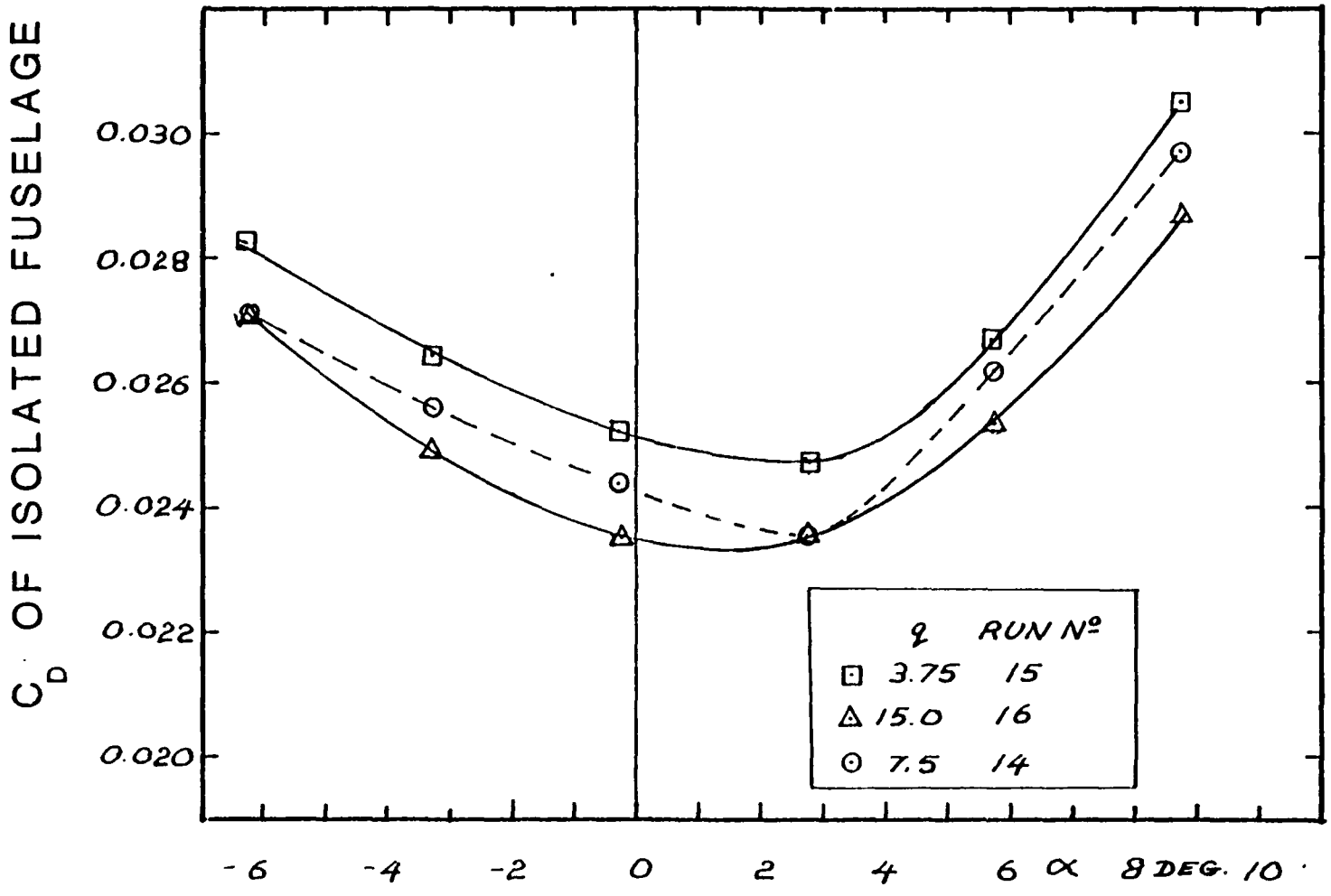

Figure 19. Isolated Fuselage Drag Coefficient Versus Angle of Attack

TABLE 4. C_{Dmin}, C_{Lx}, AND BODY-OFF C_D AT C_{Dmin}

Run No.	Configuration	Dynamic Pressure (lb/ft^2)	C_{Dmin}	C_{Lx}	α_x (deg)	Body C_D at given q & α_x	Body-Off C_D
1	BWHDV, $i_H = 0$	3.75	0.0443	0.290	-3.24	NA*	--
2	" + T_s, $i_H = 0$	3.75	0.0495	0.1646	-4.18	0.0269	0.0226
3	" + " , $i_H = 0$	7.5	0.0464	0.170	-4.08	0.0260	0.0204
6	" + " , $i_H = 10$	7.5	0.0471	0.125	-5.62	0.0268	0.0203
7	" + " , $i_H = -10$	7.5	0.0637	0.415	-0.61	0.0245	0.0392
8	BNWHDV + " , $i_H = 0$	7.5	0.0522	0.220	-3.49	NA	--
11	BWDV + "	7.5	0.0426	0.090	-5.63	0.0267	0.0159
12	BW + "	7.5	0.0406	0.050	-5.97	0.0270	0.0136
13	" + "	3.75	0.0442	0.150	-4.89	0.0274	0.0168
17	BFR + T_{s1}	15.0	0.0442	0.3425	-4.06	0.0249	0.0193
18	" + T_s	15.0	0.0486	0.275	-4.32	0.0256	0.0230
19	" + T_{s2}	15.0	0.04675	0.275	-4.49	0.0256	0.0212
20	" + "	7.5	0.0498	0.300	-3.9	0.0259	0.0239
24	BNFR + T_{s2}	15.0	0.0550	0.330	-1.39	NA	--
27	$BNFRC_{30}$ + T_{s2}, $i_C = 0$	15.0	0.0560	0.250	-4.17	NA	--
30	" + " , $i_C = 10$	15.0	0.0588	0.330	-4.06	NA	--
31	" + " , $i_C = -5$	15.0	0.0574	0.230	-3.12	NA	--
32	$BNFRC_{60}$ + T_{s2}, $i_C = 0$	15.0	0.0564	0.300	-3.99	NA	--
33	" + " , $i_C = 10$	15.0	0.0586	0.330	-4.06	NA	--
34	" + " , $i_C = -5$	15.0	0.0574	0.300	-6.47	NA	--
35	" + " , $i_C = 0$	7.5	0.0572	0.300	-3.89	NA	--
36	BFR + T_{s3}	15.0	0.0464	0.315	-4.28	0.0255	0.0209
37	" + T_{s2}	15.0	0.0488	0.325	-3.78	0.0252	0.0236
39	BFRSE + T_{s2}, $\delta_E = -10$	15.0	0.0487	0.2616	-3.14	0.0248	0.0239
41	" + " , $\delta_E = 10$	15.0	0.0525	0.2410	-6.15	0.0270	0.0255
43	" + " , $\delta_E = 0$	15.0	0.0498	0.3968	-3.09	0.0247	0.0251
49	BFRS + T_{s2}	7.5	0.0498	0.300	-3.92	0.0259	0.0239
56	BFR	7.5	0.0482	0.320	-4.09	NA	--

*NA denotes that body-alone data are not available (for tests either without transition strips or with extended nose).

Wing Taper. C_f is calculated from the Prandtl formula for a fully-turbulent flat plate (Refs. 6 and 7).

$$C_f = \frac{0.455}{(\log_{10} Re)^{2.58}} \tag{8}$$

At the relatively low Reynolds numbers of the present tests C_f is a strong function of Reynolds number. Therefore it is not sufficiently accurate to compute C_f from Re based on the mean geometric chord of the exposed area of each component. Instead, for large components (such as front and rear joined wings and the monoplane wing) the variation of C_f and F_n from root to tip must be allowed for, by means of a weighting factor, F_w, defined as:

$$F_w = \frac{C_{fRoot} \times F_{nRoot} + C_{fTip} \times F_{nTip}}{2 \times C_{fMGC} \times F_{nMGC}} \tag{9}$$

where the root, tip, and MGC Reynolds numbers are computed at the appropriate locations on the exposed area of each surface. Table 5 lists these Reynolds numbers. Table 6 presents the associated values of C_f, F_n, and F_w.

The form factors at the root, tip, and MGC required for Eq. 9 are obtained from two-dimensional test data on similar airfoils. Figure 20 graphs such data, taken from Ref. 8, for NACA 4409 at $C_L = 0.3$. These data were obtained in a turbulent wind tunnel, but show similar trends to the more recent data of Ref. 9 (for the same airfoil and C_L) obtained from a low turbulence tunnel. (The Ref. 9 data points are also shown on Fig. 20.)

Tail Surfaces. Figure 21 shows F_n for the NACA 0009 airfoil employed in the fin of the joined wing, the horizontal dorsal and ventral tails of the conventional configuration, and the 30-degree sweep canard. The two-dimensional drag data used for Fig. 21 were obtained from Ref. 8. No taper correction is necessary because of the small size of the tail surfaces. The form factor shown in Fig. 21 applies for zero angle of attack, hence it predicts too low a drag for the complete

TABLE 5. WING REYNOLDS NUMBER COMPARISON

Item	Reynolds No. Length (ft)	Reynolds Number $q = 3.75$ lb/ft^2	$q = 7.5$ lb/ft^2	$q = 15.0$ lb/ft^2
Rear wing, root chord	0.3295	--	166,462.4	235,413.3
Rear wing, M.G.C. of exposed area	0.2471	--	124,846.8	176,560.1 (1)
Rear wing, tip chord	0.1647	--	83,234.6	117,711.5
Front wing, root chord*	0.4628	--	233,828.8	330,683.9
Front wing, M.G.C. of exposed area	0.3552	--	179,464.1	253,800.6 (2)
Front wing, tip chord	0.2476	--	125,099.4	176,917.3
Monoplane wing, root chord*	0.7714	275,593.8	389,748.5	--
Monoplane wing, M.G.C. of exposed area	0.5964	213,072.5 (3)	301,330.0	--
Monoplane wing, tip chord	0.4214	147,375.8	208,420.9	--

*At wing-fuselage junction (not centerline).

Note: Average of (1) and (2) = 215,180.4 = 1.01 × (3)

TABLE 6. WING TAPER WEIGHTING FACTORS AND C_f VALUES

Item	Location	q = 3.75 lb/ft^2		q = 7.5 lb/ft^2		q = 15.0 lb/ft^2	
		$C_f \times 10^4$	F_n	$C_f \times 10^4$	F_n	$C_f \times 10^4$	F_r
Rear Joined Wing	Root	--	--	64	1.0269	59	0.9193
	M.G.C.*	--	--	68	1.198	63	1.0073
	Tip	--	--	75	1.3594	69	1.1785
				F_w = 1.2323		F_w = 1.0758	
Front Joined Wing	Root**	--	--	60	0.9193	55	0.8753
	M.G.C.*	--	--	63	0.9976	59	0.9046
	Tip	--	--	68	1.1932	63	1.0023
				F_w = 1.0807		F_w = 0.9438	
Monoplane Wing	Root**	58	0.8949	54	0.8753	--	--
	M.G.C.*	61	0.9438	57	0.8802	--	--
	Tip	66	1.0905	61	0.9487	--	--
		F_w = 1.0171		F_w = 0.9222			

*Mean geometric chord of exposed area.

**Root chord of exposed area (not centerline chord).

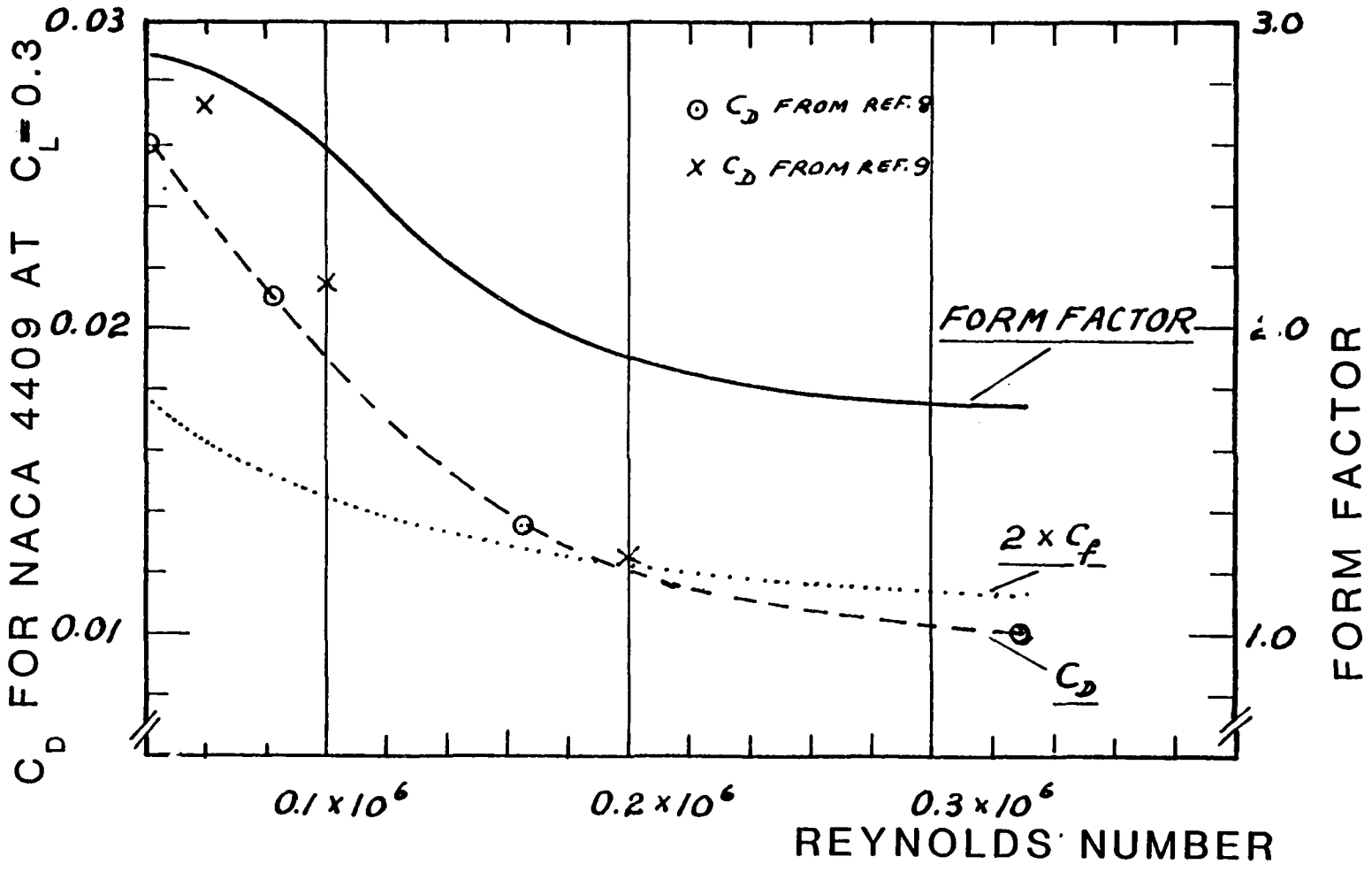

Figure 20. Drag Coefficient and Form Factor for NACA 4409 Airfoil at C_L = 0.3

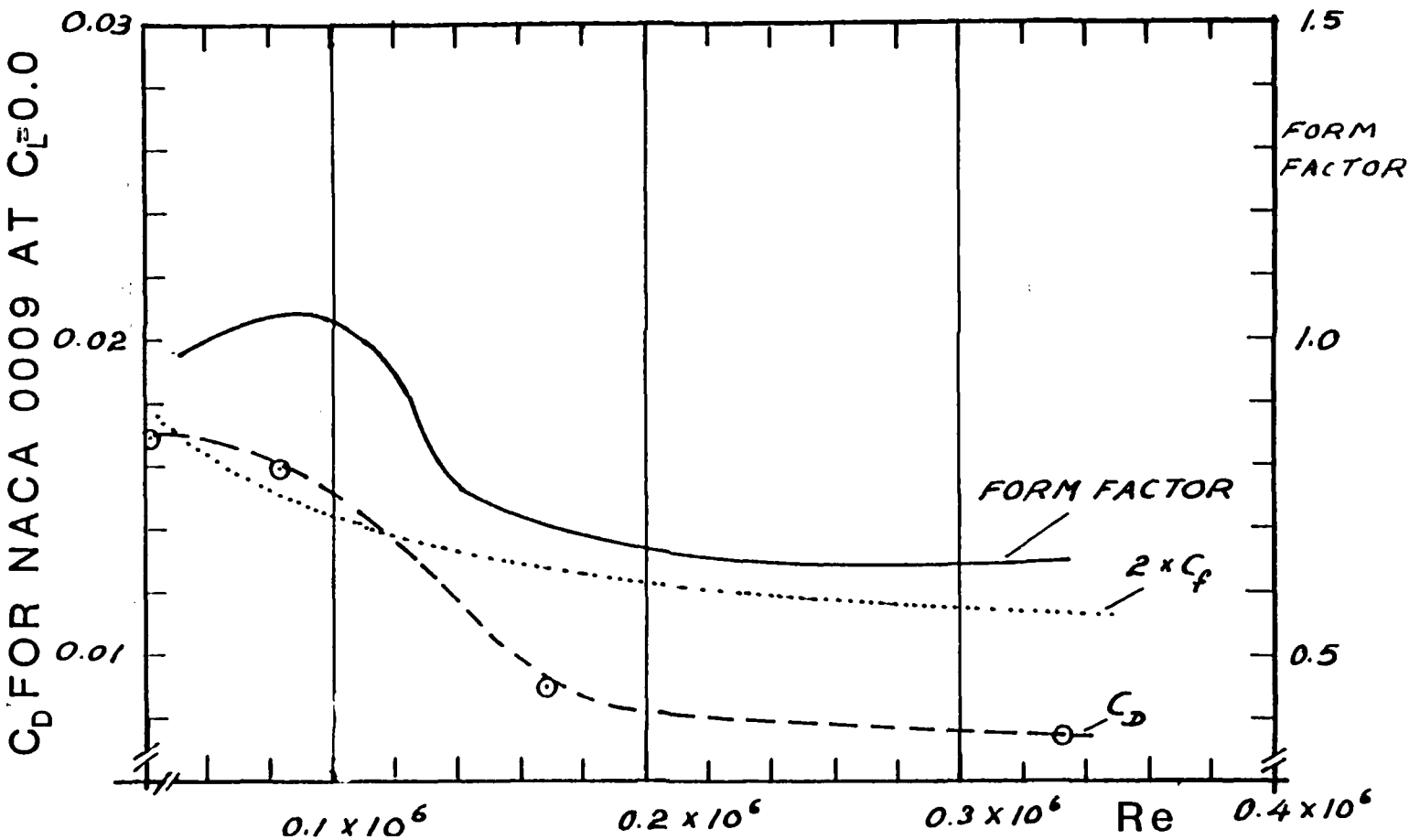

Figure 21. Drag Coefficient and Form Factor for NACA 0009 Airfoil at C_L = 0.0

configuration when the tail surfaces are at non-zero angle of attack. The most accurate prediction occurs when the tail incidence is such that the tail carries no lift.

Transition Strips. Since transition strips were employed to force transition at 5% chord it would be more accurate to compute C_f in Eq. 7 for a 95% turbulent flat plate rather than a fully turbulent flat plate, as was done here. However, the gain in accuracy was found to be negligible and did not justify the added complication.

A more important consideration of transition strips relates to their added drag. Figure 22 shows the variation of the drag of joined wing configuration BFR with various thicknesses of transition strip. The graph of Fig. 22 indicates that transition was forced even with a transition strip only 0.005 in. high, since extrapolation of the variation of C_D with strip height yields a C_D higher than the C_D with no strip. (See Ref. 10 for explanation of this criterion for determining whether transition has been forced.) To compare joined versus conventional wing drag coefficients it is desirable that the comparison should be made at equal values of h/c, where h = height of transition strip and c = mean geometric chord of exposed area. For the monoplane with transition strip T_s, which is 0.015 in. high, h/c = 0.0021. The joined wing was tested with transition strips 0.005, 0.010, and 0.015 in. high (T_{s3}, T_{s2}, and T_{s1}, respectively).* These give h/c values of 0.0014, 0.0028 and 0.0042 where c is the average of the front and rear wing MGC's. Thus for the most accurate drag comparison, the monoplane drag results should be compared against the average of results obtained for the joined wing with 0.005 and 0.010 inch strips. For example, Run 13 data on Configuration BW + T_s may be compared against the average of the data obtained in Run 36 (BFR + T_{s3}) and Run 19 (BFR + T_{s2}). This will be done in the drag comparison given below.

*See Volume II for further details of the transition strips.

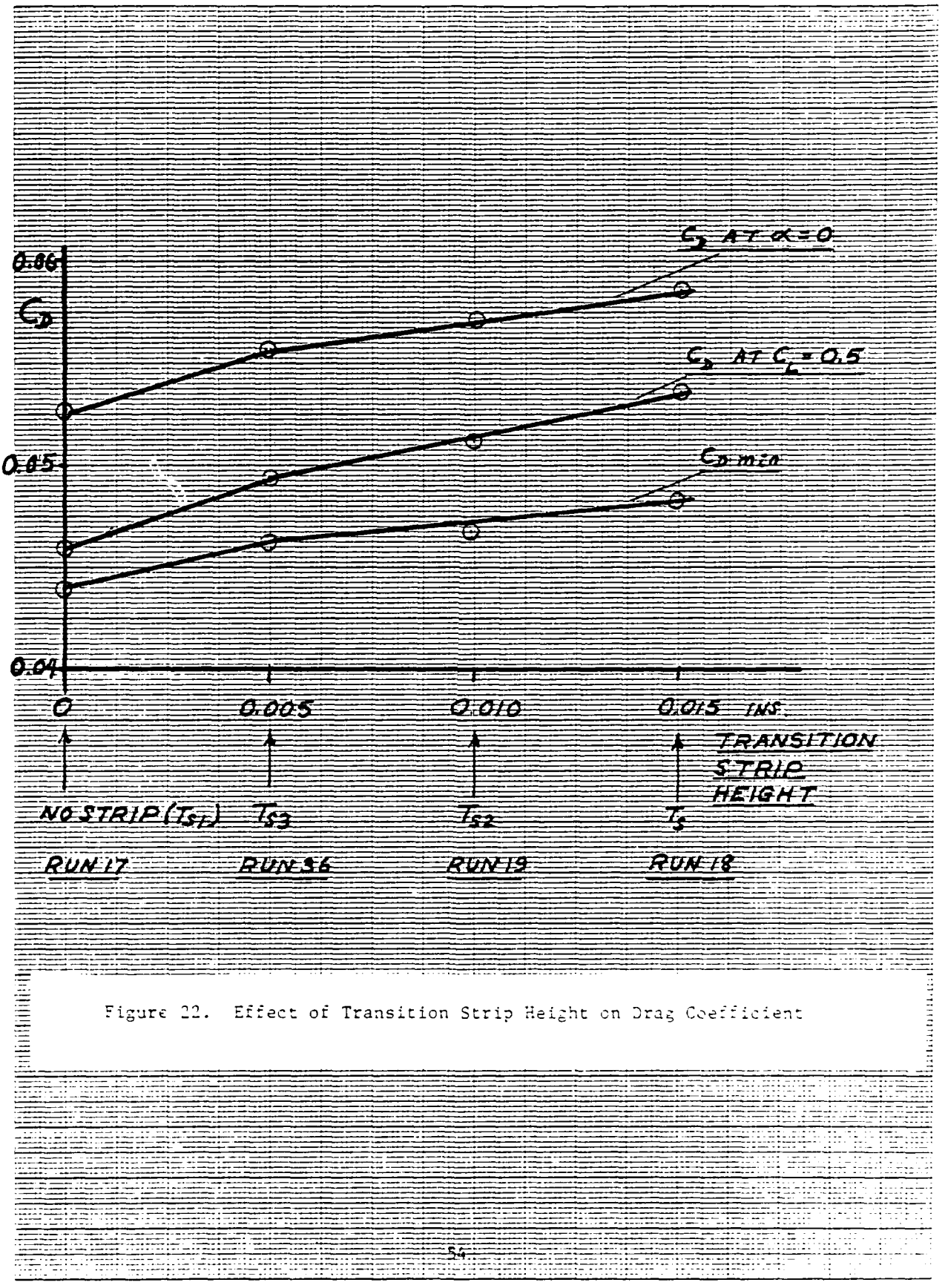

Figure 22. Effect of Transition Strip Height on Drag Coefficient

2.5 RESULTS OF ANALYSIS OF C_{Dmin}

The minimum drag coefficient for various body-off configurations was calculated by Eq. 7, with the F_n values for the monoplane wing and joined wings initially set equal to 1.0. Taper correction factors from Table 6 were applied and tail surface form factors from Fig. 21 were employed. The resulting C_{Dmin} was ratioed to the body-off C_{Dmin} deduced from the test results for the same configuration and dynamic pressure. Table 7 lists the values of this ratio, denoted as k'. These values of k' yield the difference in $(C_{Di})_{min}$ between the joined and conventional wing configurations, as explained below.

Consider two configurations "C" and "D". By definition their minimum drag coefficients are given by:

$$C_{DDmeasured} \triangleq C_{DDpredicted} \times k'_D \tag{10}$$

$$C_{DCmeasured} \triangleq C_{DCpredicted} \times k'_C \tag{11}$$

If the configurations employ airfoils of the same general type, with similar cambers and thicknesses, and if both configurations have a similar degree of aerodynamic cleanness one would expect that k'_C would equal k'_D, in which case the following equation would be satisfied:

$$C_{DDmeasured} = C_{DDpredicted} \times k'_C \tag{12}$$

In practice Eq. 12 will not be satisfied exactly, and from the definitions of Eqs. 10 and 11 it follows that:

$$C_{DDmeasured} \equiv \underbrace{C_{DDpredicted} \times k'_C}_{\text{"Expected Drag"}} + \underbrace{(k'_D - k'_C) \times C_{DDpredicted}}_{\text{"Unexpected Drag"}} \tag{13}$$

The last term in Eq. 13 represents that part of C_{DD} which cannot be predicted from test data on Configuration "C". For purposes of comparing a

TABLE 7. MINIMUM DRAG PARAMETER k′ FOR BODY-OFF CONFIGURATIONS

Run No.	Dynamic Pressure q lb/ft^2	Partial Configuration	A *	B **	$k' = \frac{A}{B}$
2	3.75	WHDV + T_s, i_H = 0	0.0226	0.0133	1.6992
3	7.5	WHDV + T_s, i_H = 0	0.0204	0.0112	1.8230
6	7.5	WHDV + T_s, i_H = 10	0.0203	0.0112	1.8125
7	7.5	WHDV + T_s, i_H = -10	0.0392	0.0112	3.5000
11	7.5	WDV + T_s, i_H = 0	0.0159	0.0100	1.5900
12	7.5	W + T_s	0.0136	0.0089	1.5281
13	3.75	W + T_s	0.0168	0.0105	1.6667
17	15.0	FR + T_{s1}	0.0193	0.0119	1.6218
18	15.0	FR + T_s	0.0230	0.0119	1.9320
19	15.0	FR + T_{s2}	0.0212	0.0119	1.7815
20	7.5	FR + T_{s2}	0.0239	0.0145	1.6483
36	15.0	FR + T_{s3}	0.0209	0.0119	1.7563
37	15.0	FRS + T_{s2}	0.0236	0.0121	1.9504
39	15.0	FRSE + T_{s2}, δ_E = -10	0.0239	0.0127	1.8819
41	15.0	FRSE + T_{s2}, δ_E = 10	0.0255	0.0127	2.0079
43	15.0	FRSE + T_{s2}, δ_E = 0	0.0251	0.0127	1.9764
49	7.5	FRS + T_{s2}	0.0239	0.0149	1.6040

* A = C_D of partial configuration from test at $C_{D_{min}}$ of complete configuration

** B = Predicted $C_{D_{min}}$ of partial configuration with with F_n = 1.0

joined wing Configuration ("D") versus a conventional configuration ("C") the last term in Eq. 13 represents a drag penalty on "D", which we denote as ΔC_D.

$$\Delta C_D = (k_D' - k_C') \times C_{DDpredicted}$$

$$= k_D' \left(1 - \frac{k_C'}{k_D'}\right) \times C_{DDpredicted}$$

$$= C_{DDmeasured} \left(1 - \frac{k_C'}{k_D'}\right)$$

Table 8 presents ΔC_D values for various pairs of configurations computed using the data given in Table 7.

The most significant comparison in Table 8 relates the joined wing configurations of Runs 19 and 36 to the tail-off monoplane configuration of Run 13. This comparison is illustrated in Fig. 23 which graphs $(C_D + \Delta C_D - C_{Dmin})$ for a pair of configurations "C" and "D". The baseline, "C", is the monoplane configuration of Run 13.* The "D" joined wing configuration is the mean of Runs 19 and 36. (As explained previously, the mean is taken to obtain a consistent ratio of transition strip height to wing chord.)

The relative lift-dependent drag of the two configurations of Fig. 23 can be obtained by ratioing $(C_D + \Delta C_D - C_{Dmin})$ from Fig. 23 at various C_L's. Figure 24 shows the result. This figure indicates that, at the design C_L (= 0.645), the lift-dependent drag of the monoplane (with ΔC_D included in lift-dependent drag) is 1.09 times that of the joined wing configuration. On the basis of Letcher's exact theoretical results graphed in Fig. 15(c) a ratio of 1.0486 would be expected. Hence, at the design C_L, the joined wing has less total drag than predicted. Some possible explanations of this are given below, after a discussion of the relative lift-dependent drag at off-design C_L's.

As shown by Figs. 23 and 24, the joined wing has less lift-dependent drag than the monoplane for $0.33 < C_L < 0.70$. At low C_L's the situation is reversed. This behavior is a consequence of the higher C_{Lx}

*For the baseline configuration ΔC_D is zero, by definition.

TABLE 8. CALCULATED MINIMUM DRAG INCREMENT, ΔC_D

I.D. of Partial Configurations Ⓒ and Ⓓ	Run No.	Dyn. Pr. q lb/ft^2	$C_{D_{Ⓓ}} = C_D$ of Partial Config. Ⓓ at $C_{D_{min}}$ of Total Config.* from Test	Ratio of k′-Values k'_C/k'_D	$\Delta C_{D_{Ⓓ-Ⓒ}}$ $\left(1 - \frac{k'_C}{k'_D}\right) \times C_{D_Ⓓ}$
D = FR + T_{s2}	19	15.0	0.0212	0.9357	0.00136
C = W + T_s	13	3.75			
D = FR + T_{s4}	36	15.0	0.0209	0.9490	0.00107
C = W + T_s	13	3.75			
D = FR + T_{s4}	36	15.0	0.0209	0.9675	0.00068
C = WHDV + T_s, i_H=0	2	3.75			
D = FR + T_{s2}	19	15.0	0.0212	0.9538	0.00098
C = WHDV + T_s, i_H=0	2	3.75			
D = WHDV + T_s, i_H=10	6	7.5	0.0203	1.00579	-0.00012
C = " + " , i_H=0	3	7.5			
D = WHDV + T_s, i_H=-10	7	7.5	0.0392	0.52086	0.02042
C = " + " , i_H=0	3	7.5			
D = FRSE + T_{s2}, δ_E=0	43	15.0	0.0251	0.9014	0.00248
C = FR + T_{s2}	19	15.0			
D = FRSE + T_{s2}, δ_E=10	41	15.0	0.0255	0.8873	0.00287
C = FR + T_{s2}	19	15.0			
D = FRSE + T_{s2}, δ_E=-10	39	15.0	0.0239	1.1107	-0.00264
C = FR + T_{s2}	19	15.0			

*From Table 7

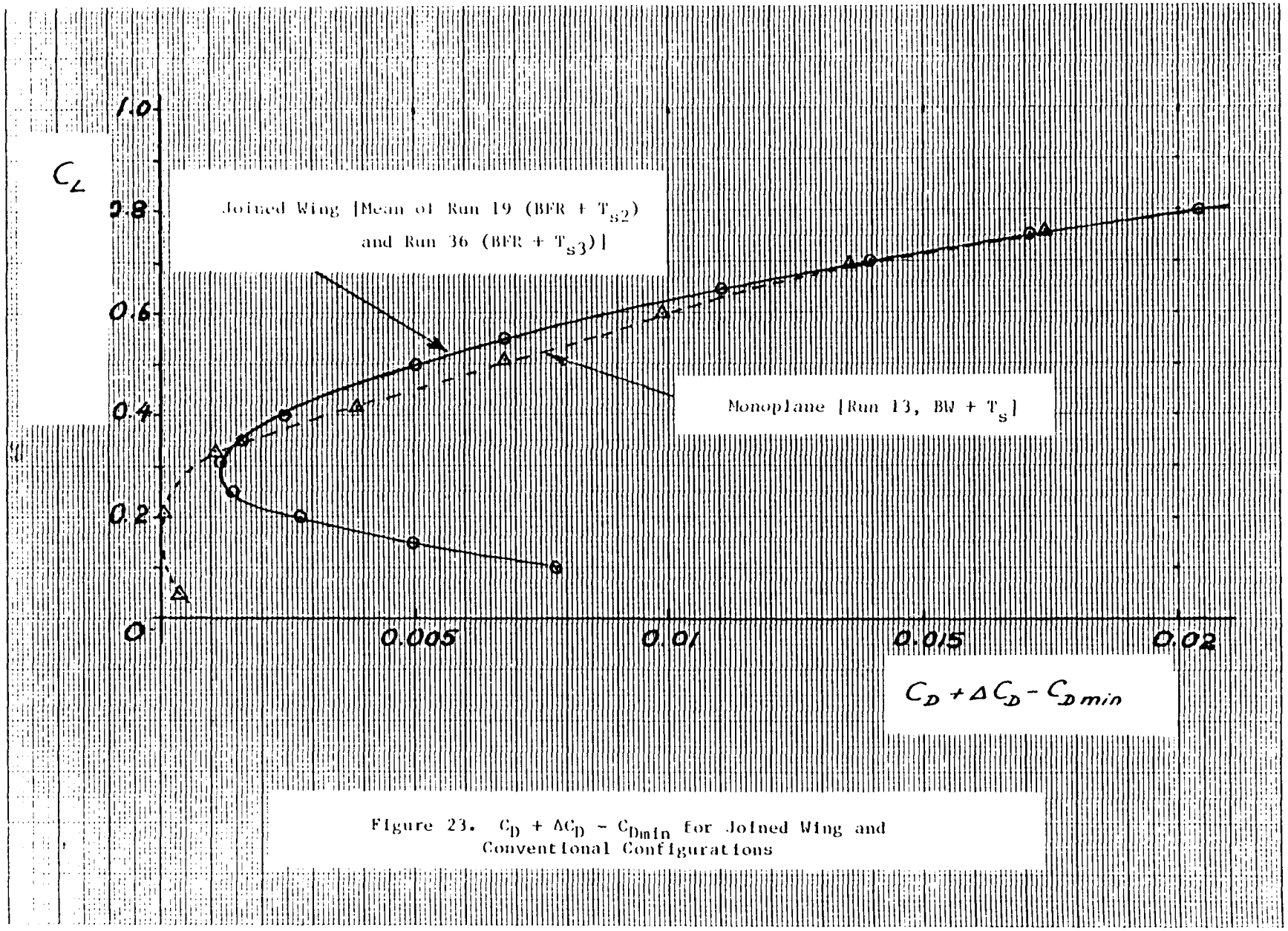

Figure 23. $C_D + \Delta C_D - C_{D_{min}}$ for Joined Wing and Conventional Configurations

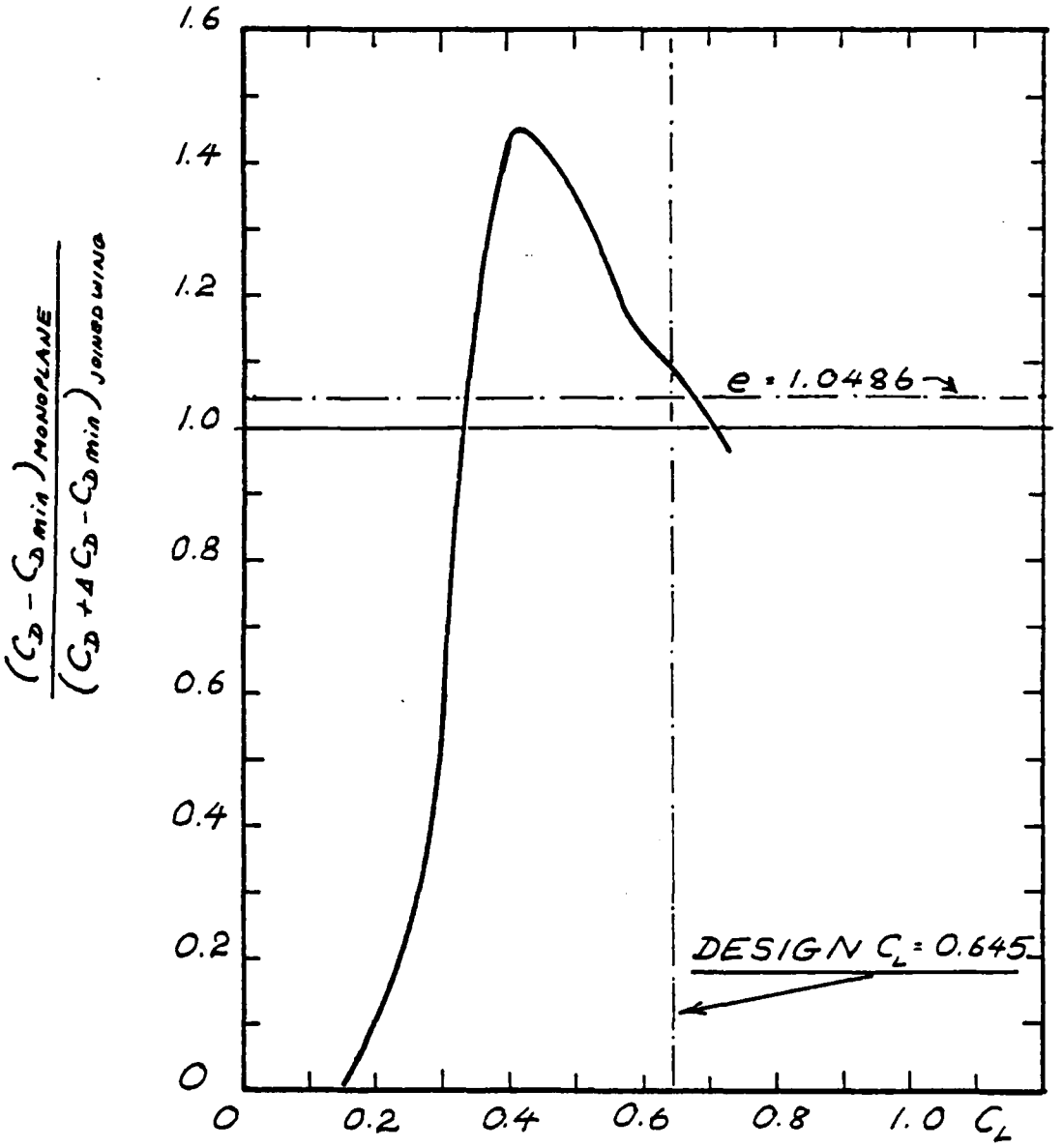

Figure 24. Relative Lift-Dependent Drag for Joined Wing and Conventional Configurations

of the joined wing and the fact that this increase in C_{Lx} is accompanied by a drag coefficient increment ΔC_D.

If ΔC_D is partly due to induced drag it may be correlated with the induced drag differential between the two configurations at their respective C_{Lx}'s. Thus it is of interest to correlate ΔC_D versus the quantity:

$$\frac{1}{\pi A}\left[\frac{(C_{Lx_D})^2}{1.0486} - \frac{(C_{Lx_C})^2}{1.00}\right]$$

where "D" denotes joined wing, and "C" denotes monoplane. Figure 25 shows this correlation for four pairs of configurations indicated by the run numbers for each pair. As explained previously, to obtain comparable transition strip height/chord ratios the mean of Runs 19 and 36 should be selected. The mean points on Fig. 25 fall near a line of slope 0.5. Although the data are limited, it would appear that ΔC_D is to some extent correlated with the function of C_{Lx} given above, and is partly due to induced drag.

2.6 INDUCED DRAG: CONCLUSIONS AND CONSEQUENCES

Although induced drag can be calculated theoretically, it cannot be precisely measured experimentally for a twisted wing because the component of induced drag at minimum total drag cannot be measured separately. This "baseline C_{Di}" has been included in the parasite-drag efficiency factor k′ in the analysis given above. By fixing equal k′ values for both the joined and monoplane wings FR and W, the drag increment of the former (ΔC_D) has been wholly assigned to induced drag. (This assignment is somewhat arbitrary, but it provides the simplest basis for comparison. Any other choice would involve unequal k′ values for the FR and W and would require simultaneous consideration of k′ and induced drag.) On this basis it is clear from Figs. 23 and 24 that for $0.33 < C_L < 0.67$ the joined wing has less induced drag than theoretically predicted. Indeed, at $C_L = 0.4$ the induced drag is 1.0486/1.45 = 72% of the predicted level. This is a valuable result for practical applications since it extends the benefit of induced drag savings to lower C_L's

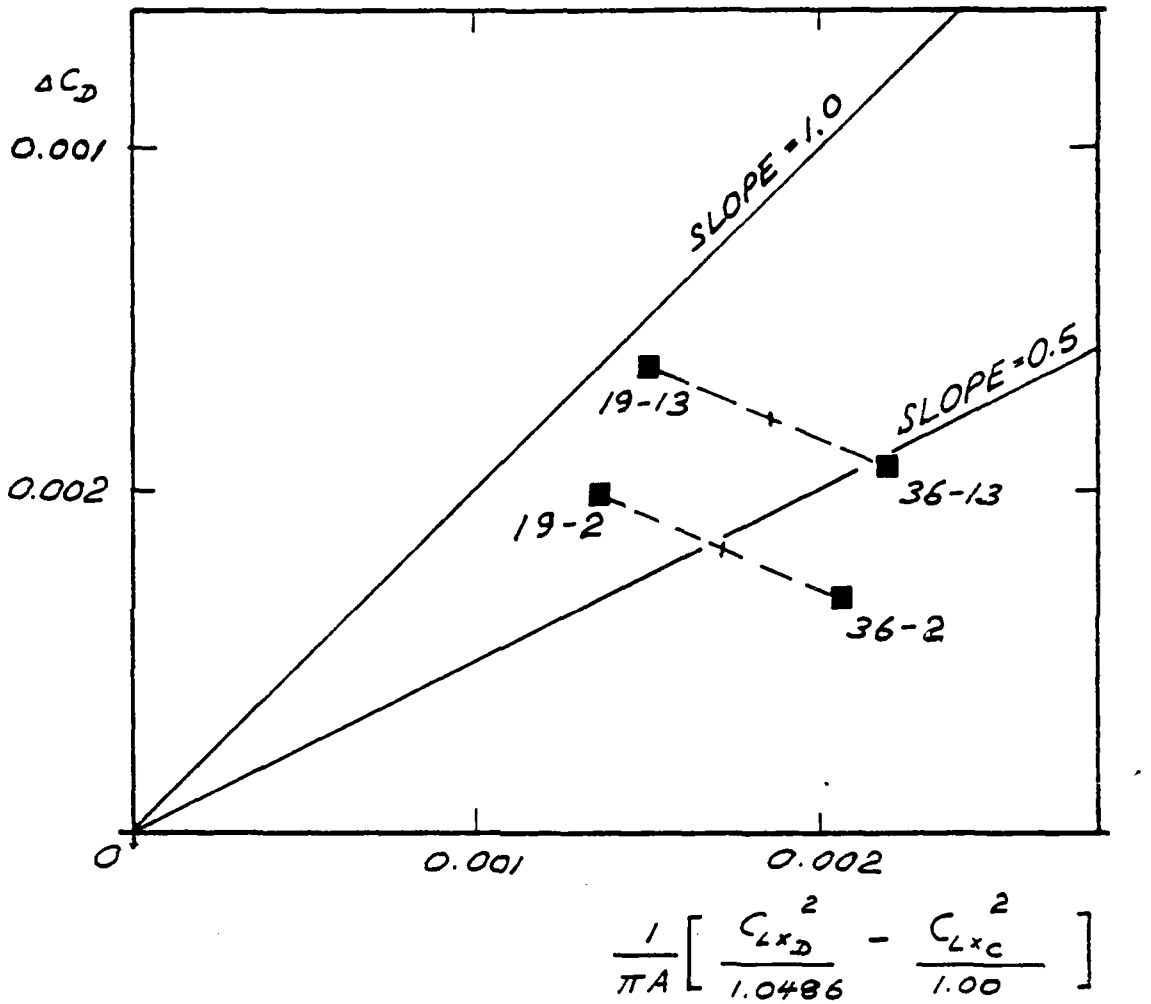

Figure 35. Induced Drag Penalty Correlation with Function of C_{Lx}

than the design C_L. In other words, the drag reduction decreases with C_L less rapidly than C_L^2. The joined wing thus overcomes an objection that has been raised against other nonplanar devices such as winglets, i.e., that such devices give the largest drag reduction at C_L's which are too high for cruise.

The reasons why the joined wing performs better than predicted at moderate C_L's are discussed below. The increases of induced drag at low C_L's ($C_L < 0.33$) and high C_L's ($C_L > 0.67$) are also discussed.

Standard methods of induced drag analysis assume that the vortex sheets shed by each lifting surface do not drift downwards relative to the free-stream direction. The neglect of this downward drift was recognized by Munk in his classical formulation of the Stagger Theorem, published in 1921 (Ref. 11). Munk's work was focused on biplane configurations having small stagger. This approximation has been retained in subsequent analyses of induced drag of configurations having highly staggered multiple lifting surfaces (e.g., Refs. 3 and 5). The approximation is also implicit in our application of Letcher's results for (unstaggered) diamond wings to (staggered) joined wings having identical Trefftz-plane configurations. Neglecting the downward drift of the vortex sheet shed by the front wing overestimates the downwash at the rear joined wing. We believe this to be the major factor causing the induced drag to be overpredicted at moderate C_L's. It would be of interest to analyze the joined wing by a free-wake computer program, which would avoid the above-described limitations of fixed-wake analyses. Note that the joined wing tested here employed untypically shallow dihedral angles and moderate sweeps. The overprediction of induced drag would be expected to be greater for more typical joined wings.

The lift results analyzed in Section 3 indicate that the joined wing develops vortex lift at high C_L's. This is generally associated with an increase of induced drag, and is believed to be the cause of the fall-off in span-efficiency factor at high C_L.

Figure 23 shows a noticeable induced drag penalty for the joined wing at C_L's below the C_L for 1 "g" flight ($C_L = 0.215$). This is believed to

be due to the high C_{Lx} of the joined wing. It is anticipated that the joined wing's performance at low lift coefficients could be improved by adopting a lower design C_L. Thus some of the benefit at high C_L could be traded to obtain lower induced drag for flight at very low C_L's, if such flight is of sufficient practical importance. Note also that the elevon deflection required to trim greatly reduces the joined wing's drag penalty at low C_L. This is shown in Section 4.2 in the subsection on trim drag.

3.0 ANALYSIS OF LIFT CHARACTERISTICS

3.1 INTRODUCTION

This section analyzes the lift characteristics of the conventional and joined wing configurations tested. Measured lift curve slopes are correlated with theoretical predictions from vortex-lattice computations, and the maximum lift capabilities of the various configurations are compared on a uniform basis.

3.2 LIFT CURVE SLOPES

Lift curve slopes were extracted by differencing adjacent data points. Thus the lift curve slope was calculated at a series of mean angles of attack given by

$$\alpha_M = \frac{\alpha_1 + \alpha_2}{2} \tag{17}$$

The subscripts 1 and 2 denote adjacent data points, and the lift curve slope at C_{LM} is calculated as:

$$\left.\frac{\partial C_L}{\partial \alpha}\right|_{\alpha=\alpha_M} = \frac{C_{L2} - C_{L1}}{\alpha_2 - \alpha_1} \tag{18}$$

Figure 26 illustrates typical results for monoplane and joined wing configurations. Because no smoothing has been employed in differentiating the $C_L - \alpha$ variation, Fig. 26 exhibits considerable scatter. Allowing for this scatter, it appears that at $\alpha_M = 0$ the lift-curve slope of the joined wing configuration BFR is lower than that of the tail-off monoplane BW. This result is predicted by theory, as discussed below. Figure 26 also indicates that, below the stall, the lift-curve slope decreases with angle of attack more rapidly for the joined wing than for the conventional wing.

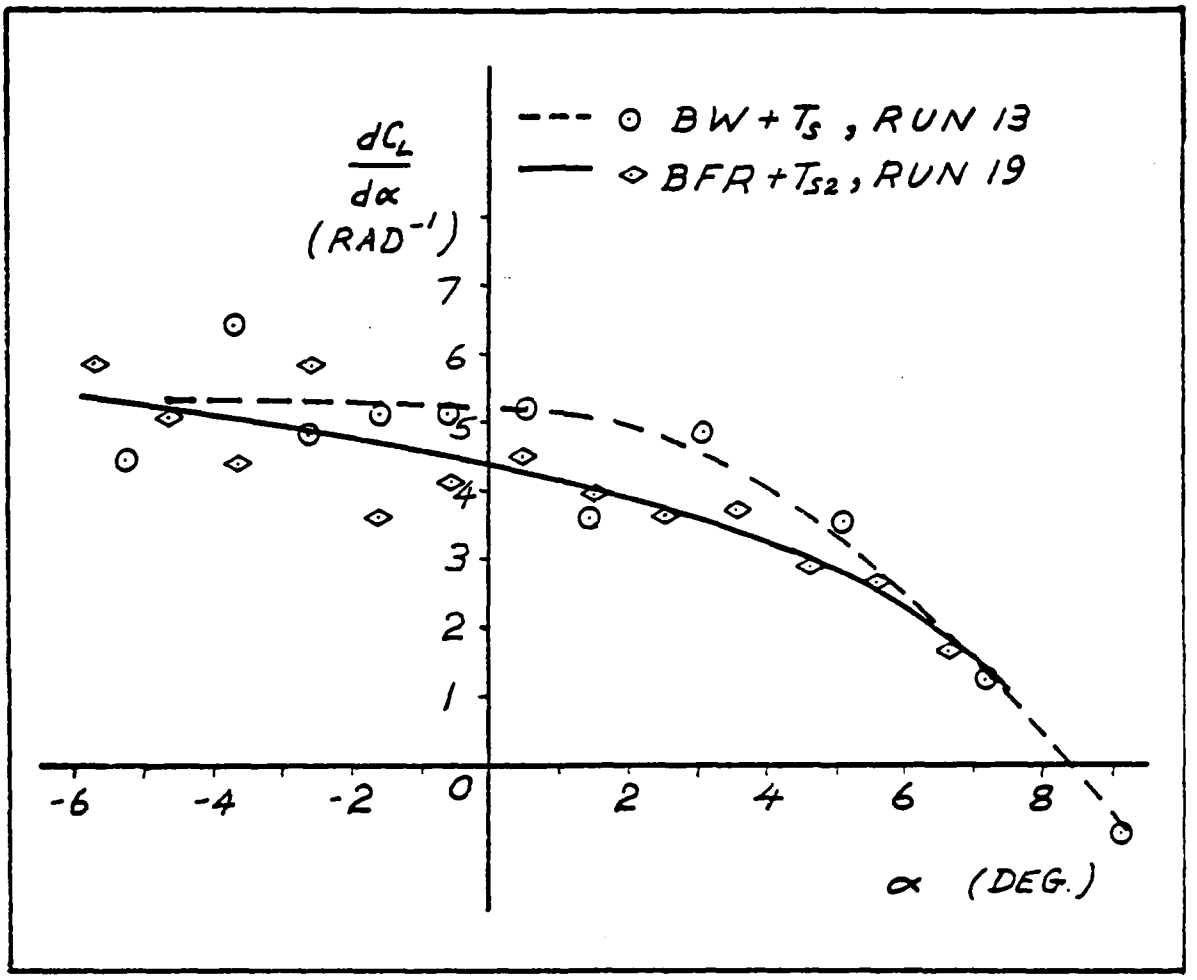

Figure 26. Comparative Lift Curve Slopes

Table 9 compares experimentally determined lift-curve slopes versus slopes predicted by a vortex-lattice digital computer program similar to that described in Ref. 12. (An updated version of this program given in Ref. 13 was employed.) Twenty-two spanwise rows of vortices and 5 chordwise rows were employed to model the joined and conventional wings, with 4 spanwise and 5 chordwise rows for canard and tail surfaces. Each surface was modeled by its gross planform, i.e., no account was taken of the interruption of the leading and trailing edges by the fuselage. No attempt was made to model the fuselage. (Note that for the short fuselage B the measured lift-curve slope is only 0.17 per radian. For the long fuselage BN, using data from runs 3 and 8, the lift-curve slope is estimated as 0.19 per radian.)

Table 9 indicates that the vortex-lattice method accurately predicts the lift curve slope at $\alpha = 0$ for the tail-off conventional configuration. For the other configurations the vortex-lattice method overestimates the lift curve slope. The vortex-lattice method would

TABLE 9. THEORETICAL AND EXPERIMENTAL LIFT CURVE SLOPES

Run No.	Configuration	Dynamic Pressure (lb/ft^2)	Measured $\partial C_L/\partial\alpha$ at $\alpha = 0$ (rad^{-1})	$\partial C_L/\partial\alpha$ from Vortex-Lattice Theory (rad^{-1})	$\frac{(\partial C_L/\partial\alpha)_{Expt.}}{(\partial C_L/\partial\alpha)_{Theory}}$
1	BWHDV, $i_H = 0$	3.75	5.39	6.01	0.90
2	BWHDV + T_s, $i_H = 0$	7.5	5.66	6.01	0.94
13	BW + T_s	3.75	5.20	5.24	0.99
14	B + T_s	15.0	0.17	--	--
16	B + T_s	7.5	0.17	--	--
19	BFR + T_{s2}	15.0	4.41	4.82	0.91
27	$BNFRC_{30}$ + T_{s2}, $i_C = 0$	15.0	5.10	6.6	0.77
32	$BNFRC_{60}$ + T_{s2}, $i_C = 0$	15.0	4.76	Not available	

give more accurate results if fuselage/tail and fuselage/canard interference effects were modeled. This may require representation of fuselage thickness (e.g., by doublets) which is beyond the capabilities of the programs of Refs. 12 and 13. The nonlinearity of the C_L vs. α relationship is not predicted by the vortex-lattice methods employed. This is ascribed to the fact that the methods employ the following approximations:

(1) No variation in the wind-axis coordinates of the configuration components is made as the vehicle is rotated to increase overall angle of attack. (In Refs. 12 and 13 each component is rotated individually.)

(2) The downward drift of the vortex sheet shed by each lifting surface is neglected.

These approximations are more important for joined wing configurations than for conventional wing-tail configurations particularly if a canard-plus-joined wing is employed because such a configuration extends over a larger longitudinal distance than an equivalent monoplane wing-plus-tail.

In summary, standard vortex-lattice methods predict $\partial C_L/\partial\alpha$ at $\alpha = 0$ with good accuracy for the isolated wing, but overestimate $\partial C_L/\partial\alpha$ by approximately 10% for the wing/tail combination and for the joined wing, and by approximately 29% for the joined wing/canard combination.

3.3 MAXIMUM LIFT COEFFICIENT

Figure 27 compares the variation of lift coefficient with angle of attack for monoplane, joined wing and hybrid (joined wing plus canard) configurations. The data shown in this graph are for untrimmed configurations; trimmed C_{Lmax} comparisons are given later in this section.

In Fig. 27 the high-C_L data for the configurations embodying a joined wing were taken at a dynamic pressure of 7.5 lb/ft^2 and therefore at a lower Reynolds number than the monoplane data obtained at 3.75 lb/ft^2 dynamic pressure. For the latter Re = 0.20×10^6, while the joined wing had Reynolds numbers of 0.17×10^6 and 0.11×10^6 on front and rear wings respectively. Despite this, the untrimmed C_{Lmax} of the

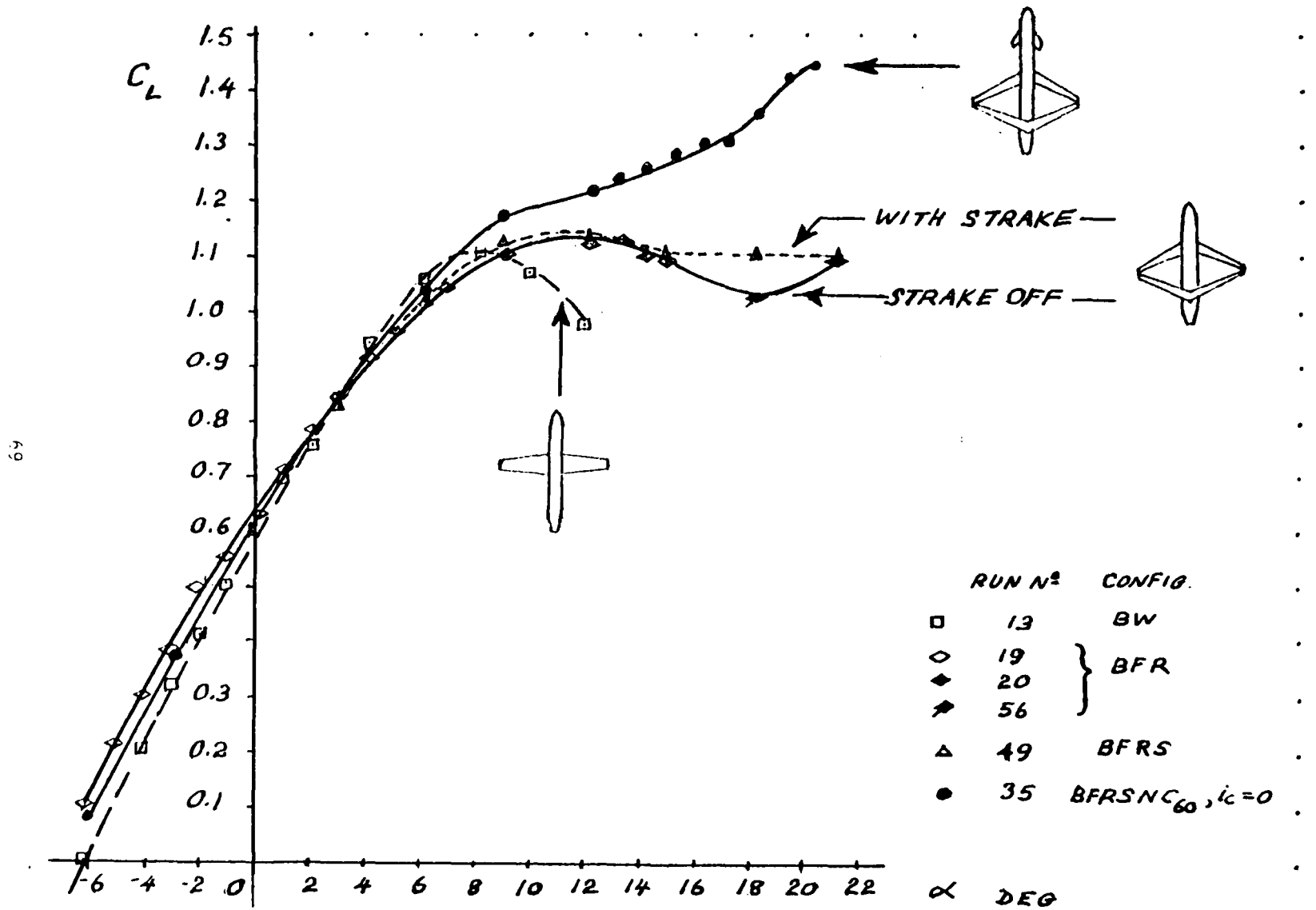

Figure 27. Lift Coefficient Versus Angle of Attack

joined wing is approximately 3% higher than that of the monoplane.* The joined wing also exhibits a less abrupt stall; with the strake installed the $C_L - \alpha$ curve was essentially flat from $\alpha = 12$ deg to $\alpha = 22$ deg which was the highest angle of attack tested.

For the hybrid configuration with the 60^o sweep canard the lift coefficient increases monotonically with angle of attack up to the maximum angle of attack tested (22 degrees). At this angle of attack a C_L of 1.45 is attained, with no indication that this represents a maximum.

In assessing the above results it must be noted that the C_L's quoted are for untrimmed configurations. In addition, although all configurations employ the same reference area, each configuration has a different exposed lifting surface area. To compare the maximum lift capability of the various configurations on a uniform basis the following parameter is used:

$$C_{Lexp} = \frac{\text{Trimmed Lift}}{\text{Dynamic Pressure} \times \text{Exposed Area of Lifting Surfaces}}$$

(Vertical tail surfaces are not included in the above exposed area.)

It is also desirable to select a common static margin for all configurations. Accordingly a static margin of zero was selected, and the C_m data given in Volume II was transferred to a moment center which gives approximately zero static margin at $C_L = 0.645$. Figures 28 and 29 show the resulting $C_m - C_L$ graphs, with C_m referred to such a moment center. Because the graphs are somewhat nonlinear the moment center does not yield zero static margin at all C_L's; however at the design C_L of 0.645, $\partial C_m/\partial C_L$ is essentially zero.

Figure 30 summarizes the results of this comparison, with additional information given in Table 10. It is clear that despite the lower Reynolds number the joined wing with elevons develops a C_{Lexp} which is at least 7% greater than that attained by the conventional wing-plus-tail configuration. The hybrid configuration $BNFRSC_{60}$ gives still further improvement, increasing C_{Lexp} to more than 119% of that of the trimmed monoplane, with no sign that this a maximum.

*Trimmed C_{Lmax} comparisons are given in Fig. 30.

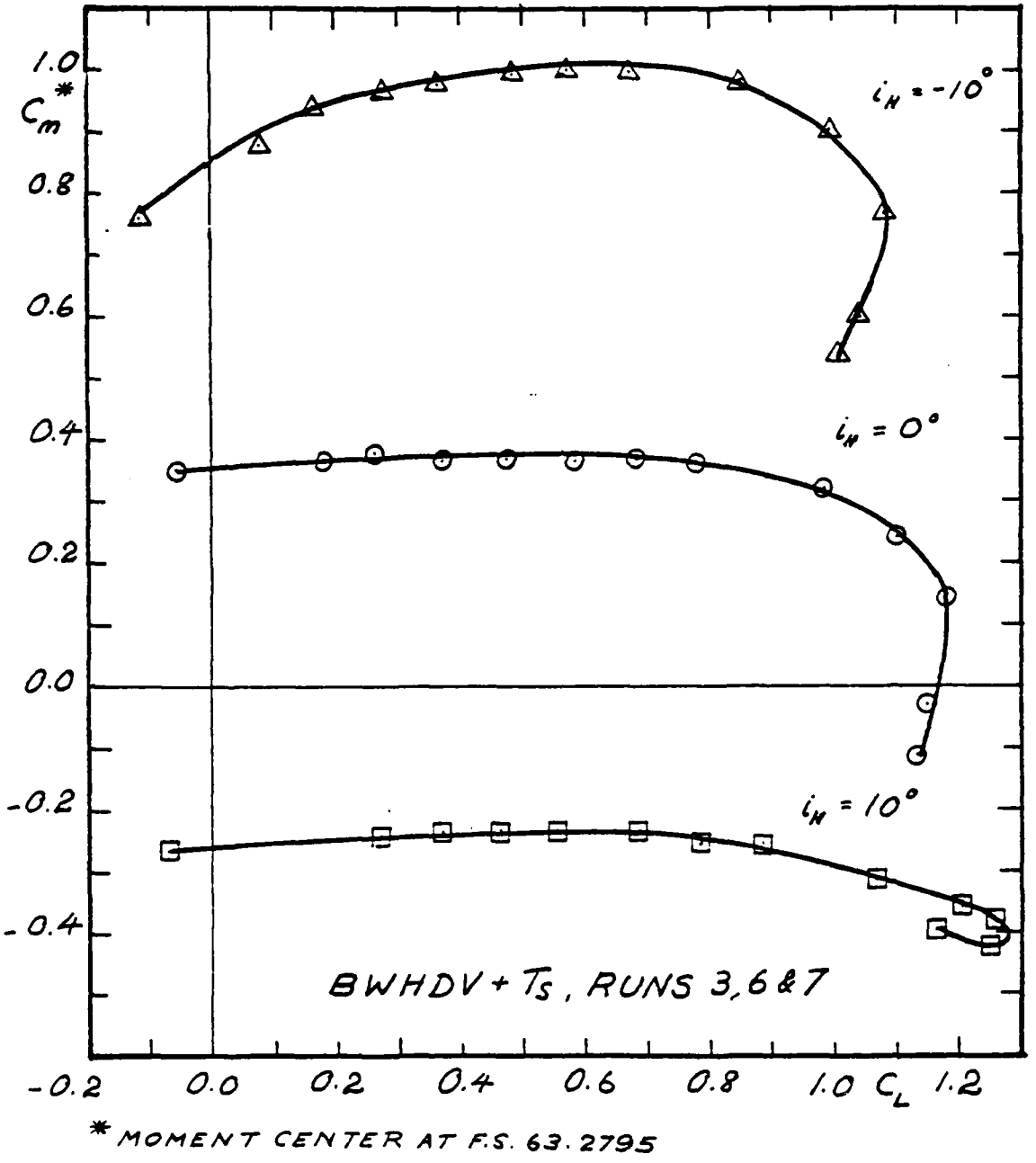

Figure 28. C_m Versus C_L for Conventional Configuration

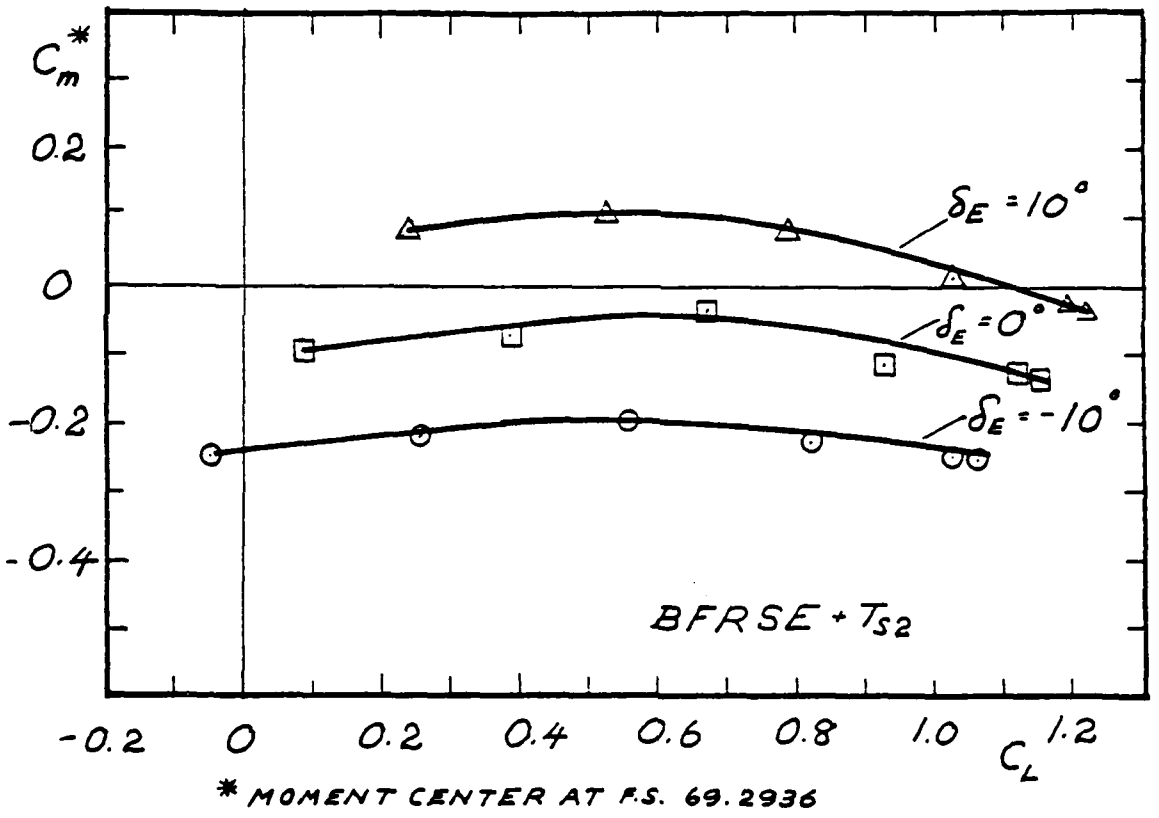

Figure 29. C_m Versus C_L for Joined Wing Configuration

TRIMMED $C_{L_{MAX}}$ AT ZERO STATIC MARGIN

CONFIG.	BWHDV	BFR	BFRSE	BFRSNC$_{60}$
	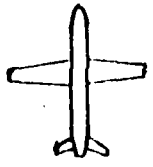	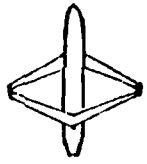	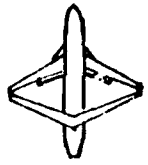	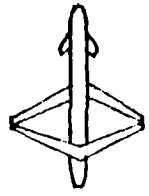
$C_{L\ MAX}$ BASED ON EXPOSED AREA	1.18	>1.24	1.27	>1.40
RELATIVE $C_{L\ MAX}$	100%	>104%	107%	>119%

Figure 30. Relative $C_{l,max}$ Based on Exposed Area

TABLE 10. MAXIMUM LIFT COEFFICIENT COMPARISON

Configuration	Exposed Area of Lifting Surfaces (ft^2)	Dynamic Pressure (lb/ft^2)	Run Nos.	$C_{L_{max}}$ Trimmed	$C_{L_{exp}}$ Trimmed	Ratio
*BWHDV + T_s, $i_H = 3^o$	3.9188	3.75	3, 6, 7	1.16	1.184	100%
*BFRSE + T_{s2}, $\delta_E = 13^o$	3.9778	7.5	39, 41, 43	1.26	1.267	107%
**$BNFRC_{60}$ + T_{s2}, $i_C = 0^o$	4.1329	7.5	35	>1.45	>1.4025	>119%
***BFR + T_{s2}	3.6639	7.5	20	1.132	1.236	104%

*Static margin = zero at $C_L = 0.645$.

**Static margin = zero at $C_L = 1.4$; large positive static margin at $C_L = 0.645$.

***Untrimmed configuration; with front wing elevons, trimmed $C_{L_{max}}$ will will be greater than untrimmed $C_{L_{max}}$.

3.4 DETAILED STALL AND BUFFET CHARACTERISTICS

Volume II of this report presents flow visualization photographs of tuft patterns on configuration BFR at angles of attack of -3, 0, 6, and 12 degrees. The latter angle of attack corresponds approximately to $C_{L_{max}}$. At this condition considerable flow separation is evident on the front wing except at the root. At α = 12 deg the rear wing exhibits some less extensive areas of separated flow except at its root. The absence of flow separation at the wing roots is encouraging, since no fillets were employed on either wing.

In view of the extensive separation displayed at α = 12 deg, the flat top of the $C_L - \alpha$ curve at higher angles of attack indicates that considerable vortex lift is developed at angles of attack greater than 12 degrees, despite the fact that the leading edge is not sharp (L.E. radius = 0.89% chord). Tuft wand examination of configuration BFRS at α = 20 deg showed strong vorticity emanating from the strake leading edge. At this condition the flow

near the front wing leading edge was separated along its entire span, but no concentrated vortices could be detected emanating from the front wing. Even in the unstalled regime (α > 6 degrees), no concentrated vortex was found to emanate from the front wing, although the standard tip vortex was readily identified located at approximately 95% of the span. (The tip vortex was found when the tuft wand was placed at least 0.5 local chord lengths aft of the rear wing.) The front and rear wings combine to generate a single pair of tip vortices of a generally similar type to that produced by a conventional monoplane. However, the lateral spacing between the tip vortices appears to be slightly wider than for a monoplane.

In view of the high C_L's obtained in the 60° sweep canard some comments on the observed flow found from tuft wands are of interest. With both the 60 deg and 30 deg canards the buffet at α > 6 degrees was markedly reduced, compared to the canard-off configurations. (Adding the strake also reduced buffet.) The 60 deg canard generated a strong L.E. vortex. At α = 11 deg this vortex passed between the front and rear wings, clearing the front wing by approximately 1.5 local chords. Between α = 11 and α = 15 deg this vortex moved above the rear wing such that at α = 15 deg it cleared the rear wing by approximately 0.3 of its local chord. At α = 20 deg the clearance reached approximately 1.5 times the local chord. These observations show that the high C_L developed for α > 15 degrees is not due to impingement of the canard vortices onto either the front or rear joined wing. For α = 20 deg, with the 60° canard on, the front wing developed a concentrated leading edge vortex located approximately 4 in. outboard of the outboard edge of the strake. This vortex did not appear for the canard-off configuration at the same angle of attack. Therefore it is not a standard "sharp leading-edge" vortex, but appears to be induced by the canard.

From the flow configurations described above it is concluded that:

(1) The joined wing does not exhibit premature or localized flow separation.

(2) The joined wing has gentle stall characteristics, giving a flat-topped C_L - α graph, particularly when a strake is fitted.

(3) Favorable interactions occur between the canard and the joined wing which increase the stalling angle of attack to >22 degrees.

(4) The joined wing generates extensive vortex lift at high angles of attack, despite the relative bluntness of its airfoils (L.E. radius = 0.89% chord).

(5) The joined wing displays considerable buffet at $\alpha > 6$ degrees. The buffet intensity is moderately reduced by the strake, and is greatly reduced by the 30-degree and 60-degree canards.

4.0 PITCHING MOMENT CHARACTERISTICS

4.1 INTRODUCTION

This section analyzes the pitching moment data presented in Volume II. In that volume the pitching moment data are graphed as C_m versus C_L curves, with C_m measured about the axis system defined in Volume II. As will be shown, additional insight can be gained by graphing C_m versus angle of attack, and by referring C_m to a fixed moment center which approximately coincides with the configuration's aerodynamic center location at low angles of attack. Hence the C_m results given in this section supplement, and do not duplicate, the corresponding results of Volume II.

Section 4.2 discusses the pitching moment characteristics at low angles of attack and compares the test results with theoretical predictions obtained by vortex-lattice calculations. Both the conventional and joined wing configurations display appreciable differences between theory and experiment. These are ascribed to the fuselage, which was not included in the vortex-lattice mathematical model. The front wing elevons are shown to generate adequate control moments, despite their short moment arm. A brief discussion of trim drag is given, extending the drag analysis of Section 3.

Section 4.3 summarizes the pitching moment characteristics at high angles of attack. It is shown that the high C_L's obtained by the addition of a canard surface are associated with large nose-up pitching moments.

Section 4.4. discusses the implications of the measured pitching moment characteristics for design of joined wing airplanes and missiles.

4.2 PITCHING MOMENT CHARACTERISTICS AT LOW ANGLES OF ATTACK

As explained in Section 2, the conventional configuration BWHDV and the joined wing configuration BFR were both optimized for $C_L = 0.645$, i.e., the wing twist and camber were computed to yield trim with minimum induced drag at this C_L. Accordingly, the wing incidences were selected to give approximately zero fuselage angle of attack at the design $C_L = 0.645$. Typically $C_L = 0.8$ is attained at $\alpha = 2$ degrees. At higher C_L's separated flow is prevalent. Hence the low angle of attack range will be defined at $\alpha < 2$ degrees. Within this range meaningful comparisons can be made between experiment and theory based on inviscid flow models, such as the vortex-lattice theory of Refs. 12 and 13, which was employed to design both the joined and cantilever wings. The results of such a comparison are given in Table 11.

Table 11 shows that the vortex-lattice method predicts C_{mo} to be more positive than the experimentally determined value. This overprediction apparently occurred because the fuselage was not represented in the vortex-lattice model. The C_{mo} collection required to bring theory into agreement with experiment is reasonably consistent for a given fuselage length (-0.262 and -0.260 for BWHDV and BFR respectively, and -0.336 and -0.425 respectively for the long-nose configurations BNWHDV and BNFR). The vortex-lattice method also overpredicts the static margin $-\partial C_m/\partial C_L$, by an increment which is fairly consistent for those joined wing and conventional configurations which have the same fuselage. For the canard-on configuration $BNFRC_{30}$ the overprediction is large. This is expected, since 39% of the canard span is covered by the fuselage, and the long moment arm of the canard magnifies the error resulting from not modeling the fuselage/canard interference.

The above-described differences between predicted and experimental pitching moment characteristics do not imply any inherent inaccuracy in the vortex-lattice method *per se*. They merely demonstrate that vortex-lattice models should include either a representation of the fuselage, or an empirical correction based on experimental data, such as that given in Table 11.

TABLE II. EXPERIMENTAL AND THEORETICAL PITCHING MOMENT CHARACTERISTICS AT LOW ANGLES OF ATTACK

Configuration		BW $i_H = 0$	BWHDV $i_H = 0$	BNWHDV $i_H = 0$	BFR	BNFR	$BNFRC_{30}$ $i_C = 0$	$BNFRC_{60}$ $i_C = 0$
Run No.		13	3	8	19	24	30	35
C_{Mo}	Expt	-0.18	0.365	0.290	-0.05	-0.17	-0.57	-0.41
	Theory	N.A.	0.627	0.627	0.255	0.255	N.A.	
	Expt-Theory	--	-0.262	-0.337	-0.260	-0.425	--	--
$\frac{\partial C_L}{\partial \alpha}$	Expt ($\alpha = 0$)	5.20	5.66	5.90	4.41	4.78	5.10	4.76
	Theory	5.24	6.01	6.01	4.828	4.828	6.60	N.A.
$\frac{\partial C_m}{\partial C_L}$	Expt ($\alpha = 0$)	0.275	-0.49	-0.358	-0.525	-0.292	-0.46	-0.75
	Theory	N.A.	-0.938	-0.938	-0.886	-0.938	-1.325	N.A.
	Expt-Theory	--	0.448	0.58	0.361	0.646	0.865	--
$\frac{\partial C_m}{\partial \alpha}$	Expt ($\alpha = 0$)	0.0529	-0.0866	-0.0607	-0.1190	-0.1611	-0.0902	-0.1576
	Theory	N.A.	-0.1561	-0.1561	-0.1835	-0.1943	-0.2008	N.A.
Moment Ref. Center Fuselage Station (in.)		66.58	66.58	66.58	73.007	73.007	67.2306	67.2306

Elevon Effectiveness. The test results on configuration BFRSE indicate elevon effectiveness parameters of:

$$\frac{\partial C_m}{\partial \delta_E} = 0.86 \text{ per radian} \quad , \quad \frac{\partial C_L}{\partial \delta_E} = 0.54 \text{ per radian}$$

Ratioing these parameters yields the effective center of pressure of the airload induced by elevon deflection. This is shown on Fig. 31. Note that the c.p. is located forward of the centroid of area of the elevons, giving the elevons a larger moment arm than might be expected. The forward location of the c.p. results from the moment induced by the elevon downwash on the rear wing.

Trim Drag. If trim drag is defined as the increment in drag due to control deflection, then trim drag may be obtained by differencing the ΔC_D values given in Table 8. With this definition the trim drag is zero when the controls are undeflected, hence a graph of trim drag versus control deflection passes through the origin. Figure 32 illustrates such graphs, drawn for configurations BFRSE and BWHDV. For the former the control is elevon deflection; the latter configuration is controlled by varying the incidence of the horizontal tail. In Figure 32 the experimentally derived data points at control deflections of -10, 0, and 10 degrees have been fitted by parabolic curves.

Figure 32, in conjunction with Figs. 29 and 30, indicates that the drag penalty for nose-up trimming moments is greater for the conventional configuration than for the joined wing configuration.

4.3 PITCHING MOMENT CHARACTERISTICS AT HIGH ANGLES OF ATTACK

Conventional Configuration. Figure 33 graphs the $C_M - \alpha$ variation for configuration BWHDV from runs 3, 6, and 7. The moment reference center for all runs has been moved aft by 0.4444 times the reference chord, to give approximately zero static margin at low angles of attack. This was done to obtain a uniform basis for comparison with the other configurations. It also provides a realistic condition because operation at small, zero, or negative static margins is typical for modern control-configured vehicles.

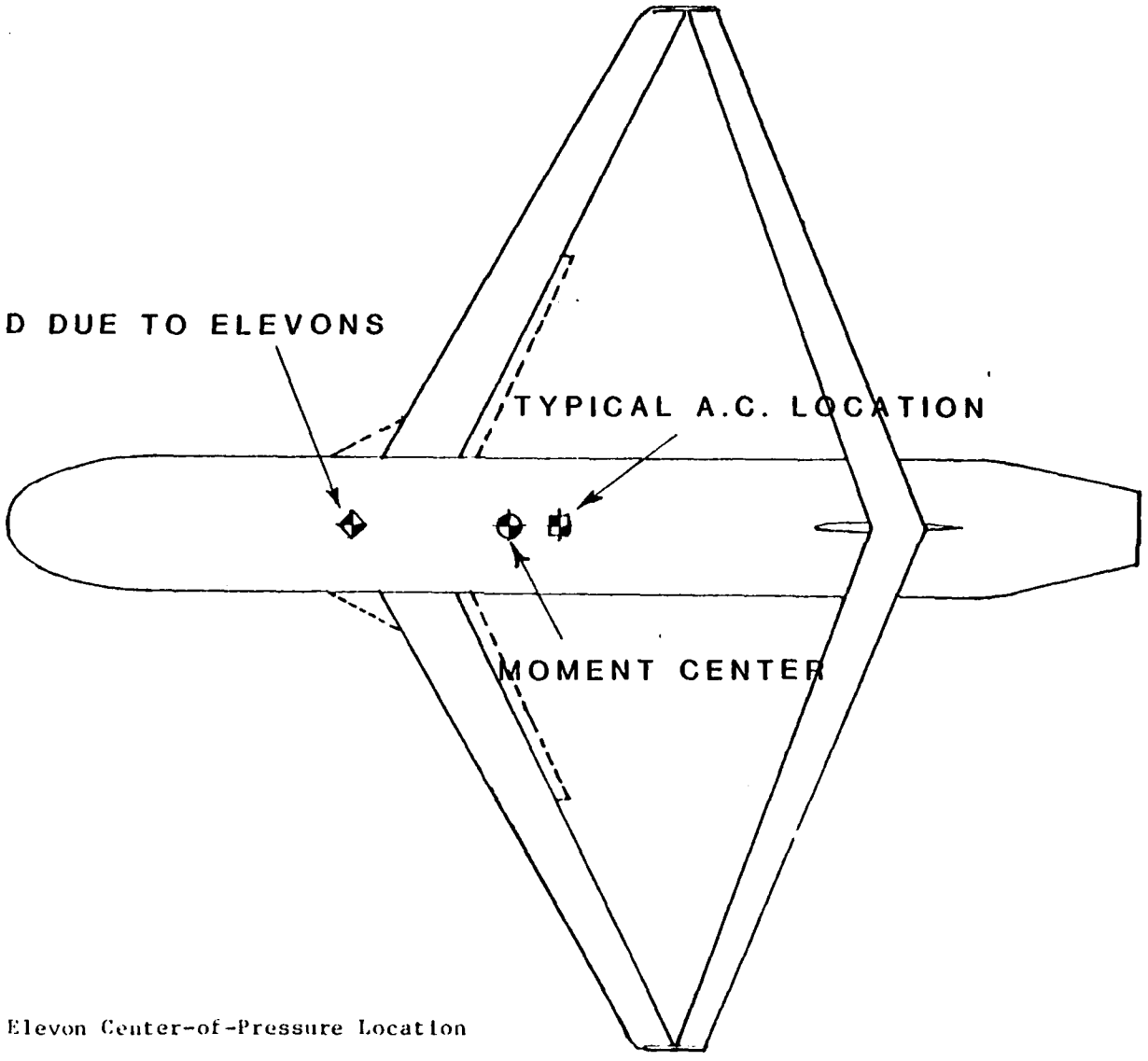

Figure 31. Elevon Center-of-Pressure Location

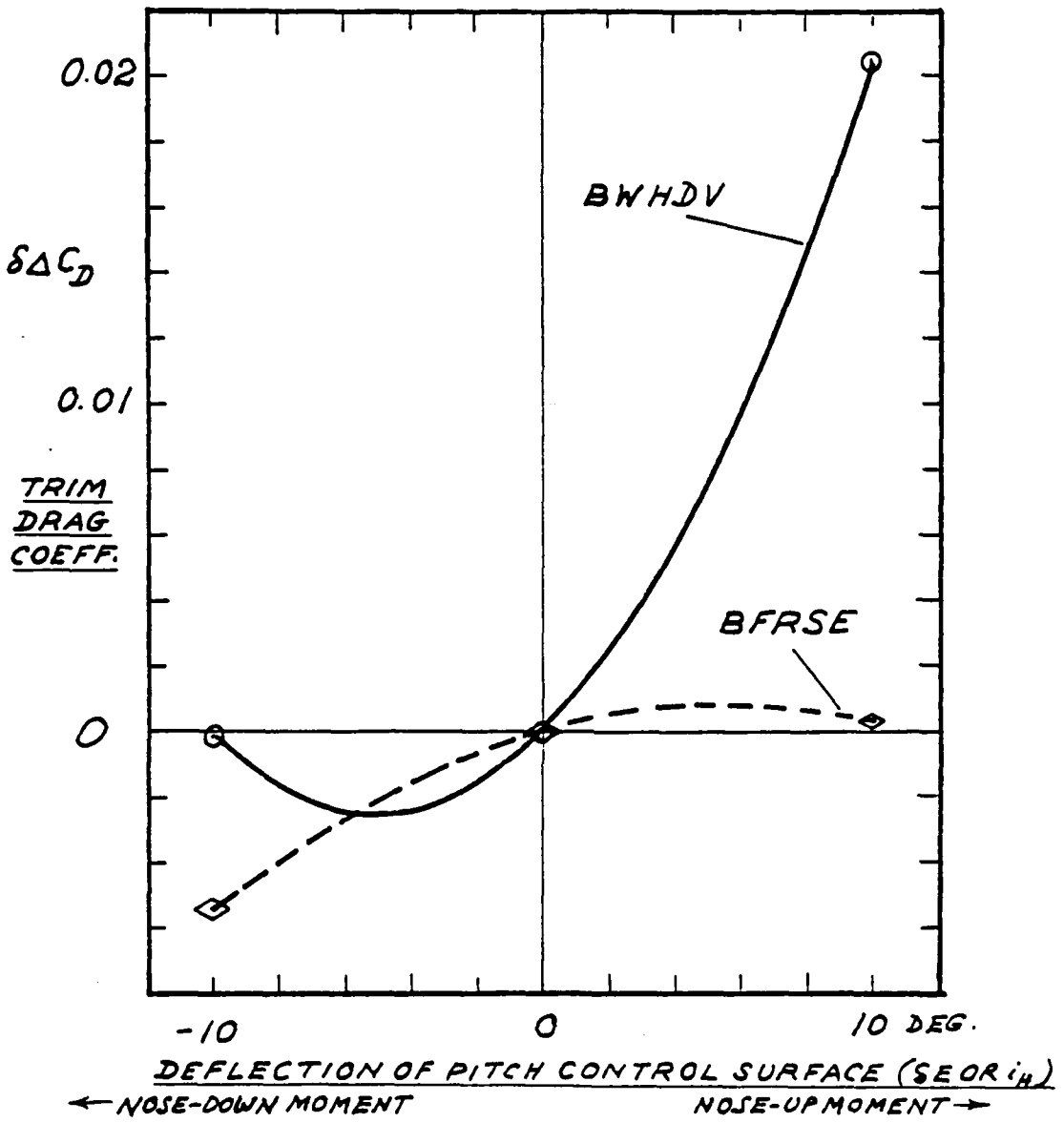

Figure 32. Trim Drag: ΔC_D Due to Control Deflection

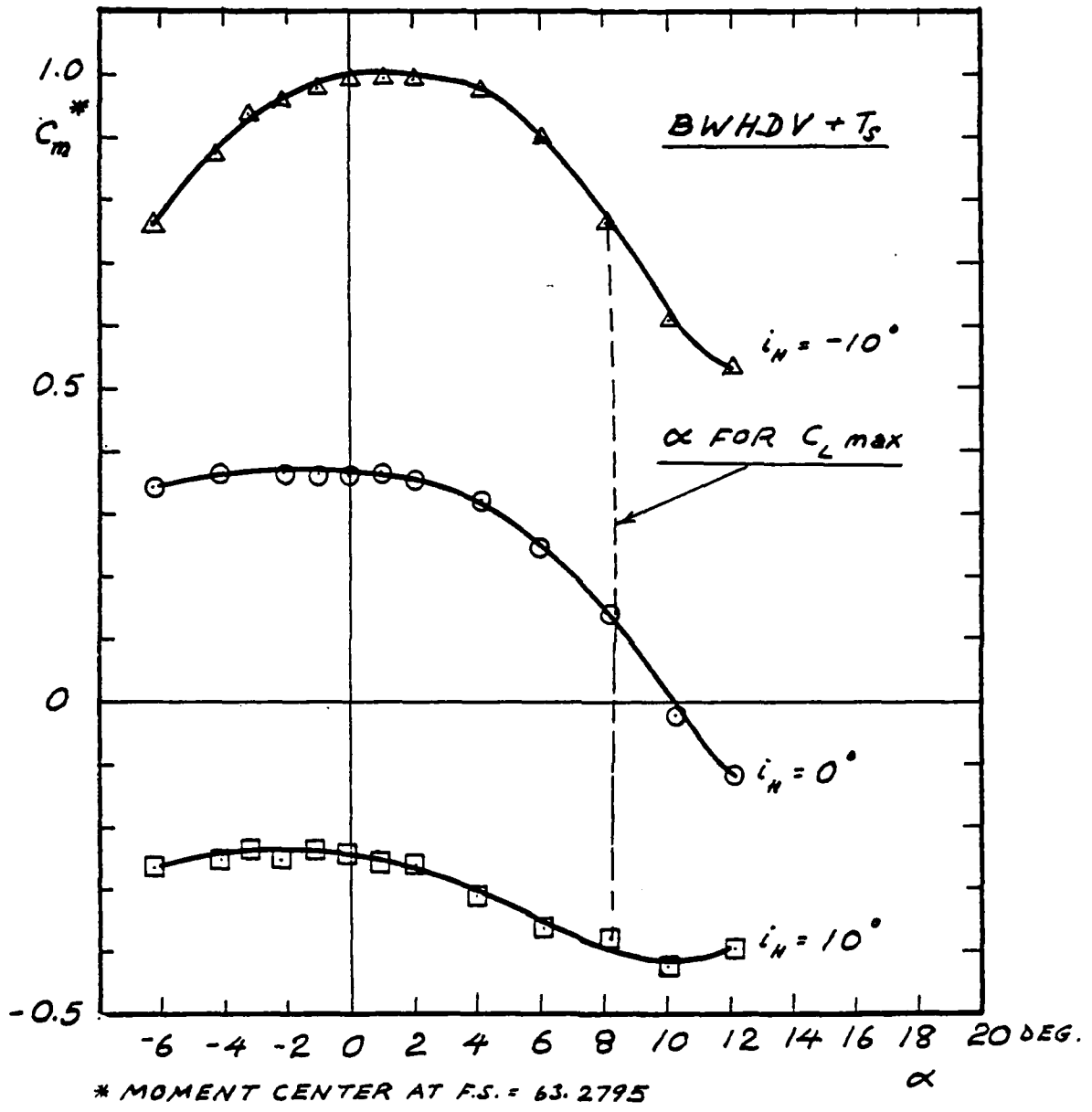

Figure 33. Pitching Moment Coefficient Versus Angle of Attack for Conventional Configurations

Figure 33 should be compared with Fig. 28, which graphs the same C_m data versus C_L. Figure 28 illustrates the near-zero static margins attained at low C_L, but does not provide much useful information at high C_L's, when the $C_L - \alpha$ variation is negative (i.e., beyond the stall). Figure 33 is of more value for such conditions: it shows that a strong pitch-down tendency exists at high angles of attack. Data from run No. 1, not shown on Fig. 33, confirms that this trend continues to α = 14 degrees, which was the highest angle of attack at which the conventional configuration was tested.

The highly nonlinear form of the $C_m - C_L$ graph for $C_L < C_{Lmax}$ is believed to be partially due to the high camber employed. Data given in Volume II (Fig. 11c) show that this pitch-down effect also occurs for the tail-off configuration. The results may therefore not be representative of configurations designed for C_L's appreciably less than the design C_L of 0.645 employed here (e.g., current Tomahawk type cruise missiles).

Joined Wing Configuration. As explained in Section 1, high-C_L data on the joined wing and hybrid configurations were taken at q = 7.5 lb/ft^2, yielding a lower Reynolds number than the conventional configuration shown in Fig. 33. This reduces the confidence level for comparisons of high angle of attack. With this reservation, we may proceed to study the pitching moment characteristics of the joined wing configurations. Figure 34 presents these data in a similar form to the conventional configuration data graphed in Fig. 33, i.e., the moment center has been relocated to yield approximately zero static margin at low angles of attack.

Figures 29 and 34 should be studied together, although the configurations illustrated are slightly different (BFRSE for Fig. 29, BFRS for Fig. 34). Below the stall, Fig. 29 indicates that the static margin increases, giving a pitch-down tendency for C_m versus α (Fig. 34) which is of similar magnitude to that for the conventional configuration. The high camber selected is believed to be responsible for this nonlinear characteristic.

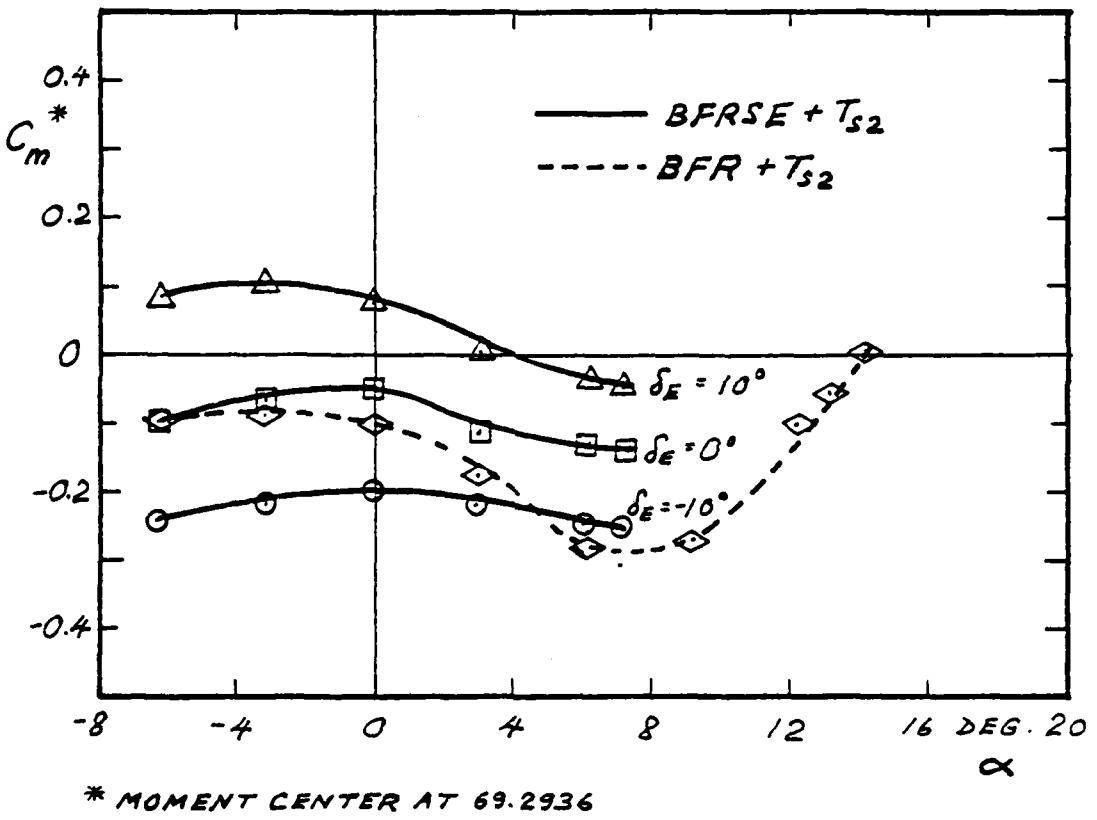

Figure 34. Pitching Moment Coefficient Vs. Angle of Attack for Joined Wing Configurations

For BFR and BFRS C_{Lmax} occurs at $\alpha \approx 11$ degrees, but the $C_L - \alpha$ curves are very flat for $\alpha > 11$ degrees, as shown in Fig. 27. For $\alpha > 10$ degrees a pitch-up tendency occurs for BFR (Fig. 34) and BFRS (Vol. II, Fig. 19c). From the tuft photos given in Volume II it appears that this pitch-up is associated with the fact that attached flow is maintained at the front wing root, although the flow over most of the rest of the wind has separated. Comparing the high angle of attack C_L's for strake-on and strake-off configurations (see Fig. 27) indicates that a high local C_L at the front wing root exists both with and without the strake. This high local C_L could be reduced by tailoring the airfoil at the front wing root to stall at a slightly lower angle of attack. Alternatively, it can be used to increased trimmed C_{Lmax} if a flap is incorporated on the inner portion of the rear wing. Deflecting such a flap T.E. down would increase total lift while re-establishing trim.

Hybrid Configuration. Figure 35 shows that the 60° sweep canard provides a large nose-up pitching moment at high angles of attack. Data graphed in Volume II (Fig. 30c) indicate that the canard is an effective trimming surface for $\alpha \leq 7$ degrees, but no canard incidence variations were tested at higher angles of attack. Therefore it is not known whether the nose-up pitching moment shown in Fig. 35 could be trimmed by the canard. A combination of canard deflection, front wing elevon deflection, and rear wing flap deflection might be required to maintain trim at the high C_L's provided by the canard.

The aerodynamic characteristics of the hybrid configuration with the 30° canard were intermediate between those with the 60° canard and no canard. The 60° canard configuration appears to be preferable in that it provides higher C_{Lmax} and has a lower C_{Dmin}.

4.4 IMPLICATIONS FOR FULL-SCALE CONFIGURATIONS

Reference 1 discusses the application of the joined wing to full scale configurations, especially cruise missiles. In Ref. 1 some discussion was given of the potential advantages of the joined wing with

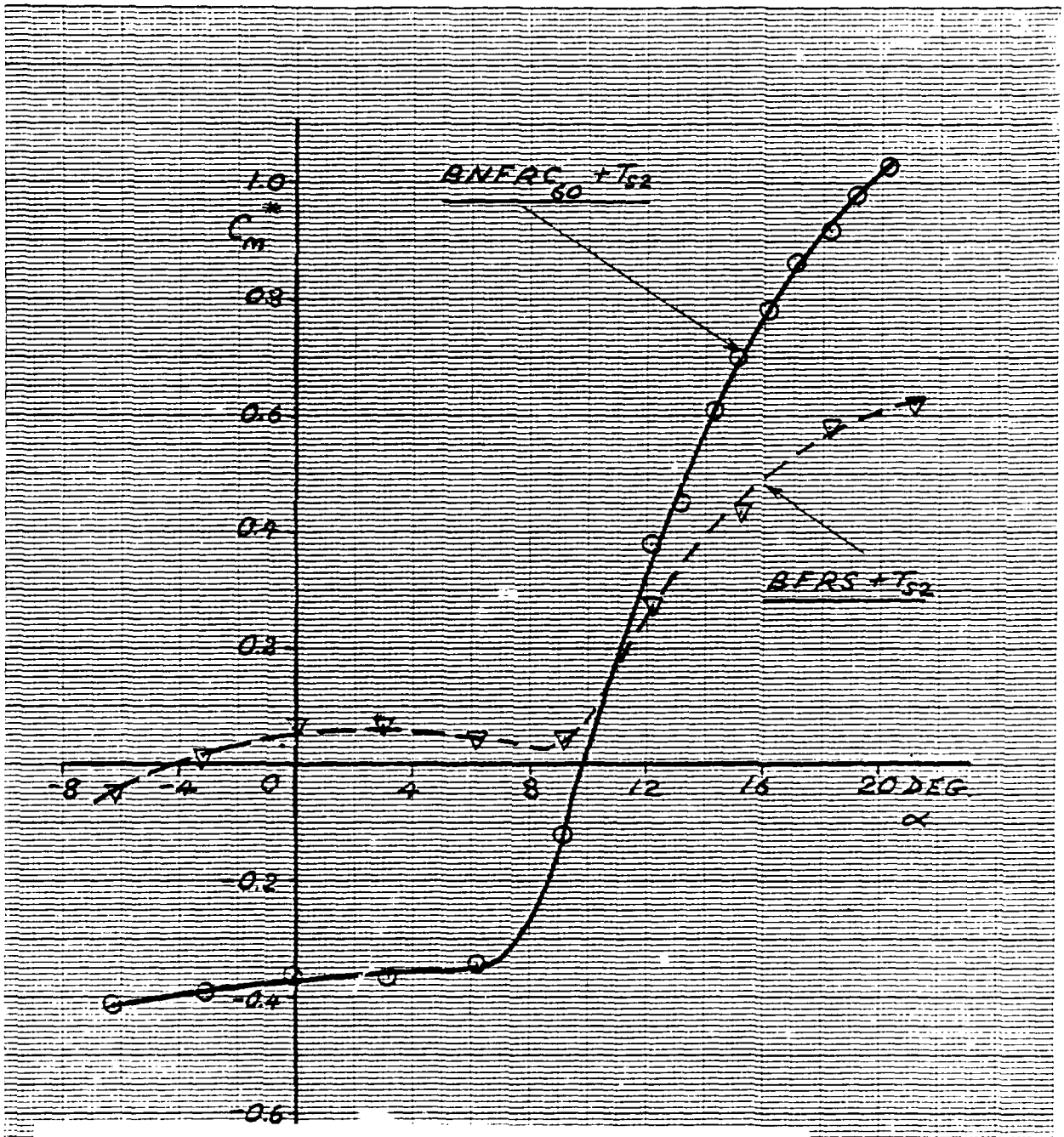

*Moment Centers (for this graph only)

Config. BFRS + T_{s2} Moment Center at F.S. 67.4306

Config. $BNFRC_{60}$ + T_{s2} Moment Center at F.S. 61.0605

Figure 35. Pitching Moment Coefficient Versus C_L for Hybrid and Joined Wing Configurations Showing Effect of 60° Sweep Canard

respect to trimmed C_{Lmax}. It was pointed out that to obtain high trimmed C_{Lmax} the local C_{Lmax} at the front wing root should be as high as possible. It is noteworthy that in the present tests this portion of the wing appears to have stalled last, despite the fact that no fillets were used. It is also remarkable that C_{Lmax} was not much affected by the strake (see Fig. 27). In view of these test results, it appears that the emphasis given in Ref. 1 to obtaining high root C_{Lmax} was perhaps misplaced. The data from the present tests suggest that the major concern should focus less on obtaining a high root C_L and more on the question of how a high root C_L can be trimmed. A rear wing flap is indicated, and it is recommended that such a flap should be included in any future joined wing tests. This flap would be a trimming device, not a primary control. As shown in Ref. 1, controls mounted on the front wing do not produce an initial wrong-way height response, and thus provide faster and more precise control of the flight path, than an aft-mounted elevator.

5.0 LATERAL-DIRECTIONAL CHARACTERISTICS

5.1 INTRODUCTION

This section summarizes the results of measurements of the lateral stability and control characteristics of the conventional, joined wing and hybrid configurations. It is shown that the latter have low directional stability, due to the small size of the fin employed on the present model and its limited moment arm. Methods of improving directional stability without increasing fin area are discussed.

Dihedral effect is shown to be positive for all configurations, the joined wing configurations displaying approximately 50% more rolling moment per degree of sideslip than the conventional configurations.

Outboard ailerons mounted on the rear wings are shown to provide good roll control with only very slight yaw coupling. Inboard ailerons (elevons) mounted on the front wing are shown to be less desirable.

5.2 DIRECTIONAL STABILITY

Figure 36 shows side views of the basic joined wing configuration BFR and of the conventional configuration BWHDV. The moment centers at F.S. 66.58 and F.S. 73.007 are also indicated. From Fig. 36 and the dimensional data of Table 1 it is clear that the vertical tail of the joined wing contributes much less to C_{n_β}* than the vertical tail of the conventional configuration. This is because the joined wing vertical tail has a smaller area, shorter moment arm, and lower aspect ratio than the vertical tail of the conventional configuration, as follows:

*Unless otherwise stated, moments are taken about the moment centers listed in Table 1, and derivatives are referred to these moment centers. As shown in Sec. 4 the moment centers give approximately equal static margins for all configurations at low angles of attack.

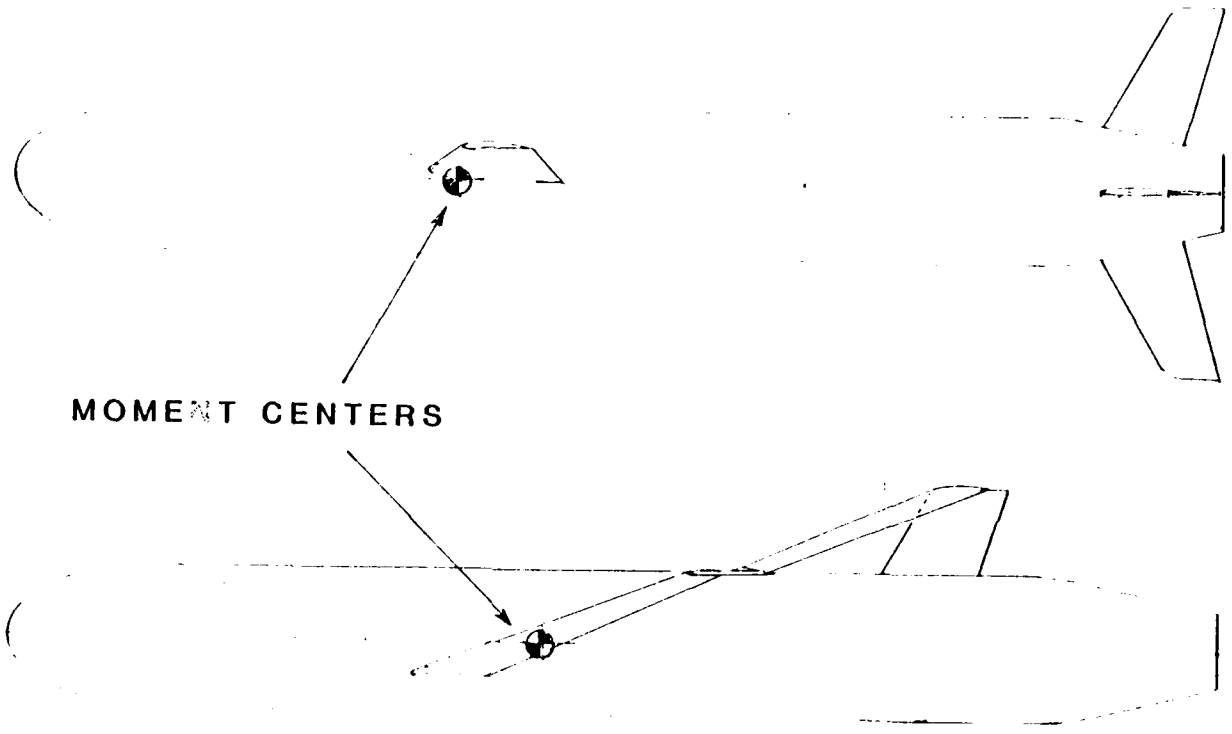

Figure 36. Comparative Side Views of Joined Wing and Conventional Configurations

AD-A145 394 LOW-SPEED WIND TUNNEL TEST ON JOINED WING AND MONOPLANE CONFIGURATIONS VO..(U) ACA INDUSTRIES INC RANCHO PALOS VERDES CA J WOLKOVITCH FEB 82 ACA-82-1

UNCLASSIFIED N00014-79-C-0953 F/G 20/4 NL

END
DATE FILMED
10 84
DTIC

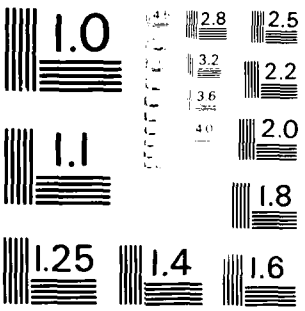

	Exposed Area	Moment Arm to 1/4 Chord	Aspect Ratio
Joined Wing	0.2433 ft^2	23.291 in.	1.10
Conventional	0.5781 ft^2	48.657 in.	4.741
Ratio $\frac{\text{Joined Wing}}{\text{Conventional}}$	0.4209	0.4787	0.232

The above ratios indicate that the joined wing configuration will have a considerably lower C_{n_β} than the conventional configuration. This trend is reinforced by the fact that the moment center of the joined wing is located 6.427" further aft than that of the conventional configuration. This increases the destabilizing yawing moment of the fuselage.

Table 12 shows C_{n_β}, C_{ℓ_β}, and the cross-wind force derivative C_{c_β} in wind axes for all the configurations for which sideslip data were measured. From Table 12 it is apparent that, while the conventional configurations have high directional stability, C_{n_β} is neutral or slightly unstable for most of the joined wing configurations. It is of interest to examine what can be done to improve directional stability of the joined wing configurations. The moment arm is dictated by the wing sweep angles and is not easily changed. The fin area can be increased, but for the present cruise missile configuration the fin height was limited by wing folding considerations, hence the additional area should be added as a ventral fin similar to that employed in the conventional configuration. A further possibility is to add effective fin area by tailoring the dihedral angles of the front and rear joined wings, i.e., less positive dihedral on the front wing and more negative dihedral on the rear wing. To examine this possibility the relative contributions of the fuselage wing and tail to directional stability must be determined. This is done below.

Isolated-fuselage directional stability measurements were not performed, but equivalent data can be derived from the longitudinal tests on the "body-alone" configuration. These yield $C_{n_\beta} = -C_{m_\alpha} \times c/b$. The resulting C_{n_β} values are given in the lower two rows of Table 13. By adjusting these values to the appropriate moment center (making use

TABLE 12. SIDESLIP STABILITY DERIVATIVES IN WIND AXES

Configuration	Run No.	α deg	β-Values deg	C_{n_β} rad^{-1}	C_{c_β} rad^{-1}	C_{ℓ_β} rad^{-1}
BWHDV + T_s	4	0	-10, 0, 10	0.3406	-1.1095	-0.1430
" + "	5	10	-10, 0, 10	0.2899	-0.7789	-0.1696
BNWHDV + T_s	9	0	-10, 0, 10	0.2472	-1.1496	-0.1498
" + "	10	10	-10, 0, 10	0.1908	-0.7812	-0.1627
BFR + T_{s2}	21	0	-5, 0, 5	-0.0229	-0.8021	-0.2372
" + "	21	0	-10, 0, 10	-0.0072	-0.8474	-0.2278
" + "	22	5	-5, 0, 5	-0.0074	-0.7305	-0.2343
" + "	22	5	-10, 0, 10	0.0075	-0.7766	-0.2320
BNFR + T_{s2}	25	0	-10, 0, 10	-0.0977	-0.9041	-0.2375
" + "	26	5	-10, 0, 10	-0.0871	-0.8210	-0.2292
$BNFRC_{30}$ + T_{s2}	28	0	-10, 0, 10	-0.0223	-0.8915	-0.2796
" + "	29	5	-10, 0, 10	-0.0083	-0.7978	-0.2805
BFRSE + T_{s2}	38	5	-10, 0, 10	0.0092	-0.7915	-0.2409

of C_{L_α} measurements to obtain C_{c_β} of the isolated body) the wing-plus-fin contributions to C_{n_β} and C_{c_β} can be estimated. These contributions are shown in Table 13 as ΔC_{n_β} and ΔC_{c_β}, and are discussed below.

First consider the side-force contribution, ΔC_{c_β}. The joined wing configurations produce a ΔC_{c_β} equal to approximately 70% of that given by the vertical tail of configuration BWHDV. This is much more than would be expected from the relative exposed areas and aspect ratios tabulated at the beginning of this section. Clearly the joined wings (even with the low dihedral angles employed here) generate substantial side forces due to sideslip. However, the contribution to C_{n_β} of the joined wing and its fin is only approximately 25% of that due to the ventral-plus-dorsal fins of the conventional configuration. To obtain more benefit from the joined wing sideforce capability, the dihedral angles should be tailored so as to move the lateral c.p. further aft. Table 12 indicates that this is feasible since the joined wing C_{ℓ_β} is approximately 50% greater than that of the conventional configuration with 3 degrees of dihedral. Hence the average joined wing dihedral can be reduced, as suggested above, without reducing C_{ℓ_β} to less than that of the conventional aircraft.

The general conclusion drawn from this is that joined wing vehicles are likely to require somewhat larger vertical tails than conventional vehicles, but not excessively so, provided that dihedral angles are properly selected.

Nonlinear Directional Stability. For most of the runs listed in Table 12 only three sideslip angles were employed: -10, 0, and +10 degrees. For configuration BFR tests were also conducted at -5 and +5 degrees of sideslip. As shown in Table 12, C_{n_β} was approximately 0.0157 rad^{-1} lower for the larger sideslip angles. This is not a serious drop. However, since it might become more severe at larger sideslip angles, it is worth while to determine the cause of the nonlinearity. The tuft photos given in Vol. II are helpful in this regard. Comparing photos No. 3, 9, and 10 indicates that, at 10 deg sideslip, trailing edge separation occurs on the joined wing fin, near its intersection with the rear wing. Presumably this is due to the high pressure

TABLE 13. CONTRIBUTION OF VERTICAL TAIL AND WING TO DIRECTIONAL STABILITY

(α = 0, Wind Axes; All derivatives are per radian)

Configuration	Run No.	Dynamic Pressure lb/ft^2	Moment Center (F.S.)in.	C_{n_β}	C_{c_β}	C_{n_β} of Isolated Body About Mom. Ctr.	C_{c_β} of Isolated Body	ΔC_{n_β}	ΔC_{c_β}
BHWDV + T_s	4	7.5	66.58	0.3406	-1.1095	-0.1811	-0.223	0.5211	0.8865
BNWHDV + T_s	9	7.5	66.58	0.2472	-1.1496	-0.2745†	-0.263	0.5217	0.8866
BFR + T_{s2}	21	15.0	73.007	-0.0229	-0.8021	-0.1540	-0.189	0.1311	0.6131
BFRSE + T_{s2}	38	15.0	73.007	0.0092	-0.7915	-0.1540	-0.189	0.1632	0.6025
BNFR + T_{s2}	25	15.0	73.007	-0.0977	-0.9041	-0.2288‡	-0.291	0.1311	0.6131
BNFRC$_{30}$ + T_{s2}	28	15.0	67.2306	-0.0223	-0.8915	-0.2312	-0.291	0.2089	0.6005
B + T_{s1}	14	7.5	66.58	-0.1811*	-0.223*	--	-0.223	--	--
" + "	16	15.0	66.58	-0.1383*	-0.189*	--	-0.189	--	--

*Obtained from measured C_m, C_L at α = 0 and 10 degrees.

†Effect of extended nose obtained by differencing runs 4 and 9.

‡Effect of extended nose obtained by differencing runs 21 and 25.

region on the rear wing undersurface. A streamlined body fairing of semi-circular cross-section starting at about 50% of the rear wing root chord and extending beyond the fin trailing edge might reduce this separation. It is recommended that such a fairing should be incorporated in future joined wing wind tunnel models.

5.3 LATERAL CONTROL

Two methods of lateral control were examined:

(1) Ailerons mounted outboard on the rear wing

(2) Elevons mounted inboard on the front wing

These controls were simulated by bent strips of aluminum sheet bolted to the appropriate wing, as described in Vol. II. (See also Fig. 11 of the present volume.) Figures 37 and 38 graph the measured derivatives $C_{\ell_{\delta A}}$, $C_{n_{\delta A}}$, $C_{c_{\delta A}}$, $C_{\ell_{\delta E'}}$, $C_{n_{\delta E'}}$, $C_{c_{\delta E'}}$ per radian, expressed in wind axes. (The prime on $\delta E'$ indicates differential elevon deflection.) The control deflection angles δA and $\delta E'$ are defined such that one angular unit (radian) of δA or $\delta E'$ corresponds to one unit of down-deflection on the port wing applied simultaneously with one unit of up-deflection on the starboard wing. Figure 39 illustrates the ratio of yawing moment to rolling moment for the ailerons and elevons. From Figs. 37, 38 and 39 it can be concluded that:

(1) The ailerons produce very little yawing moment compared to rolling moment (13% in the worst case at $\alpha = 6.22$ deg, corresponding to $C_L \approx 0.06$). This desirable characteristic stems from the negative dihedral of the rear wing, which causes the differential lifts on each rear wing half to generate yawing (as well as rolling) moments which approximately cancel the yawing moments due to differential induced drag.

(2) The elevons produce a relatively large ratio of yawing to rolling moment (41% at $\alpha = -6.22$ deg, which corresponds to $C_L \approx 0.1$). This appears to be due to positive dihedral of the front wing.

(3) As would be expected, the outboard-mounted ailerons are typically 2.2 times more effective than the inboard-mounted elevons in generating rolling moments.

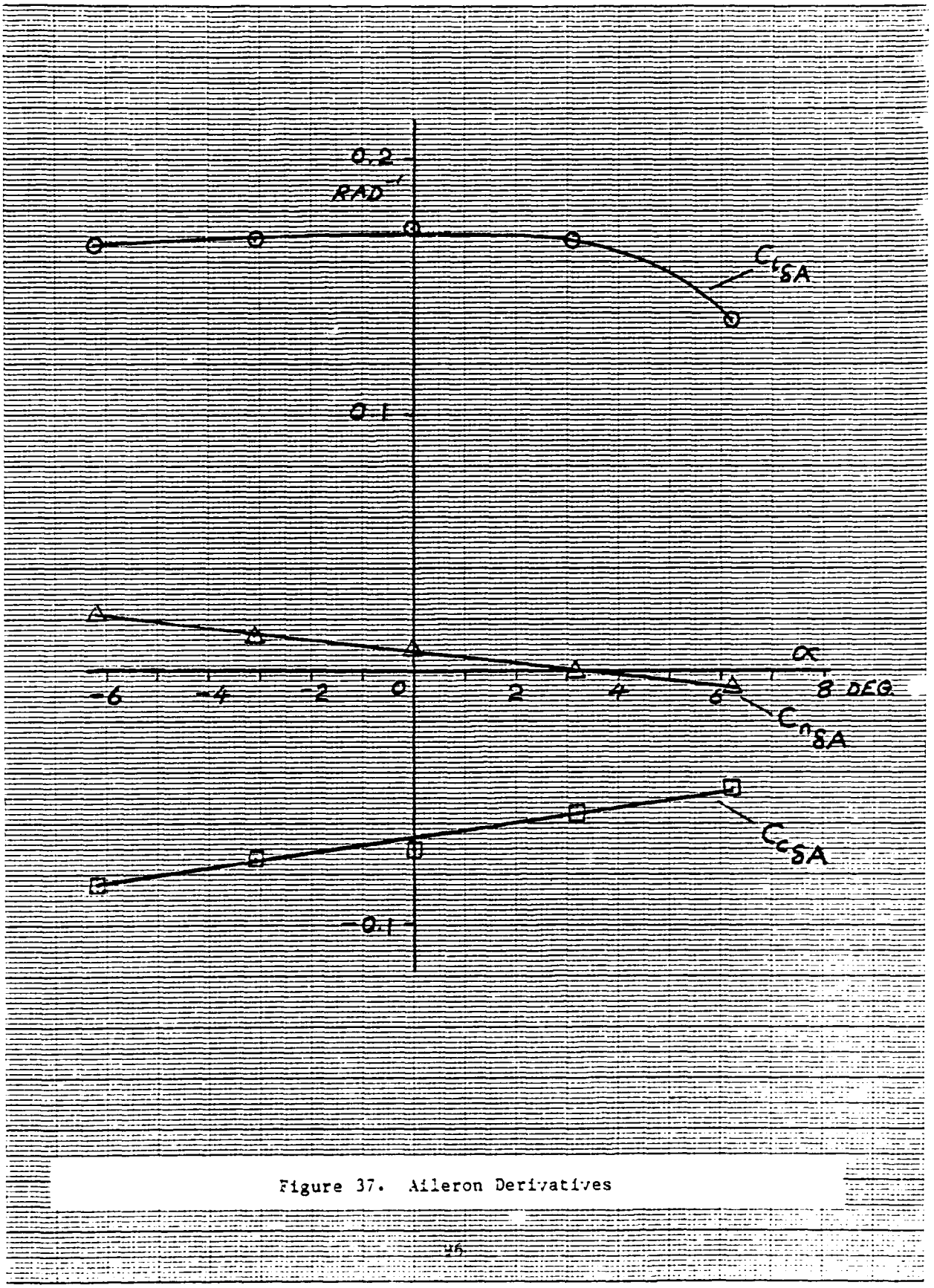

Figure 37. Aileron Derivatives

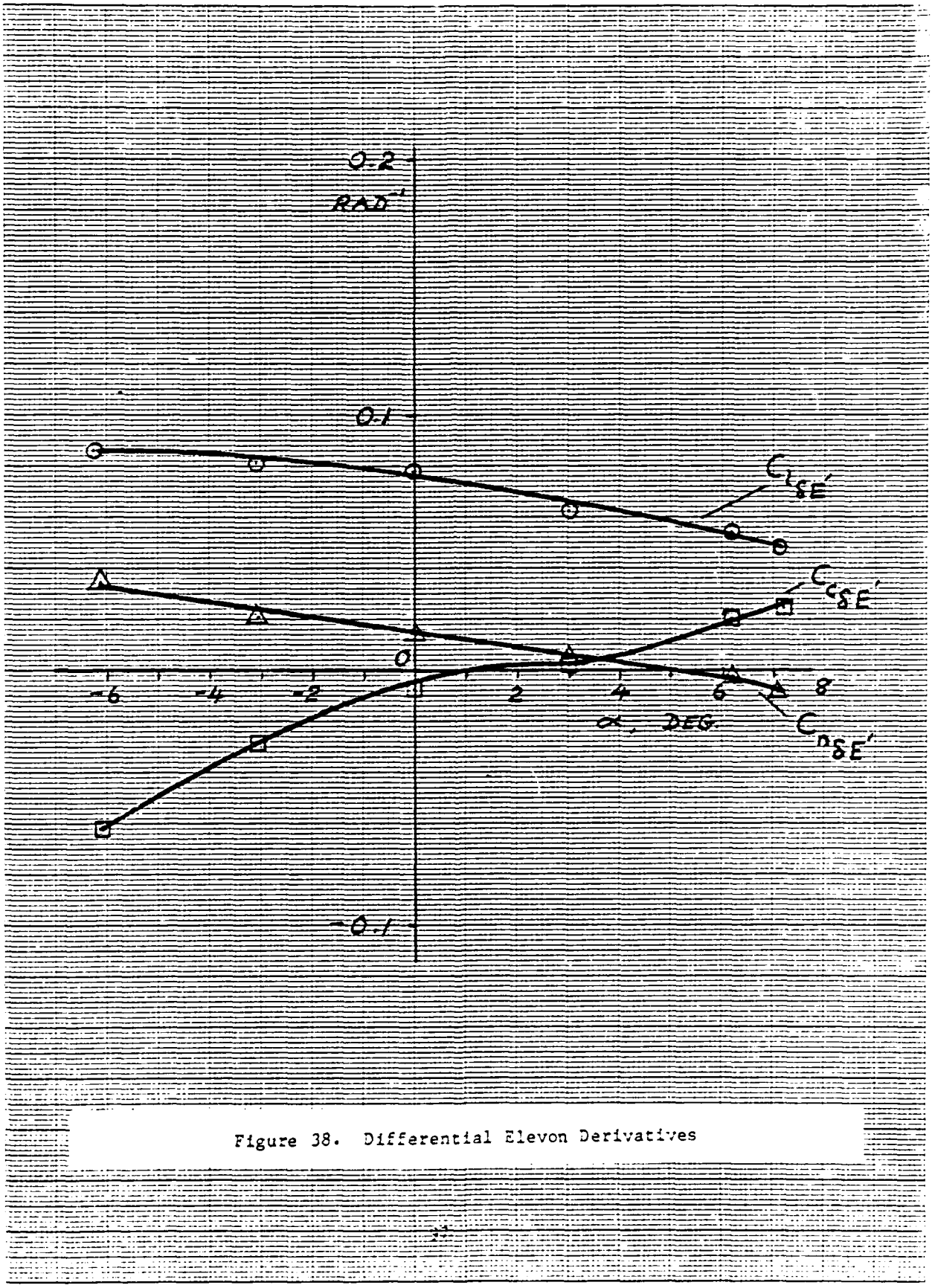

Figure 38. Differential Elevon Derivatives

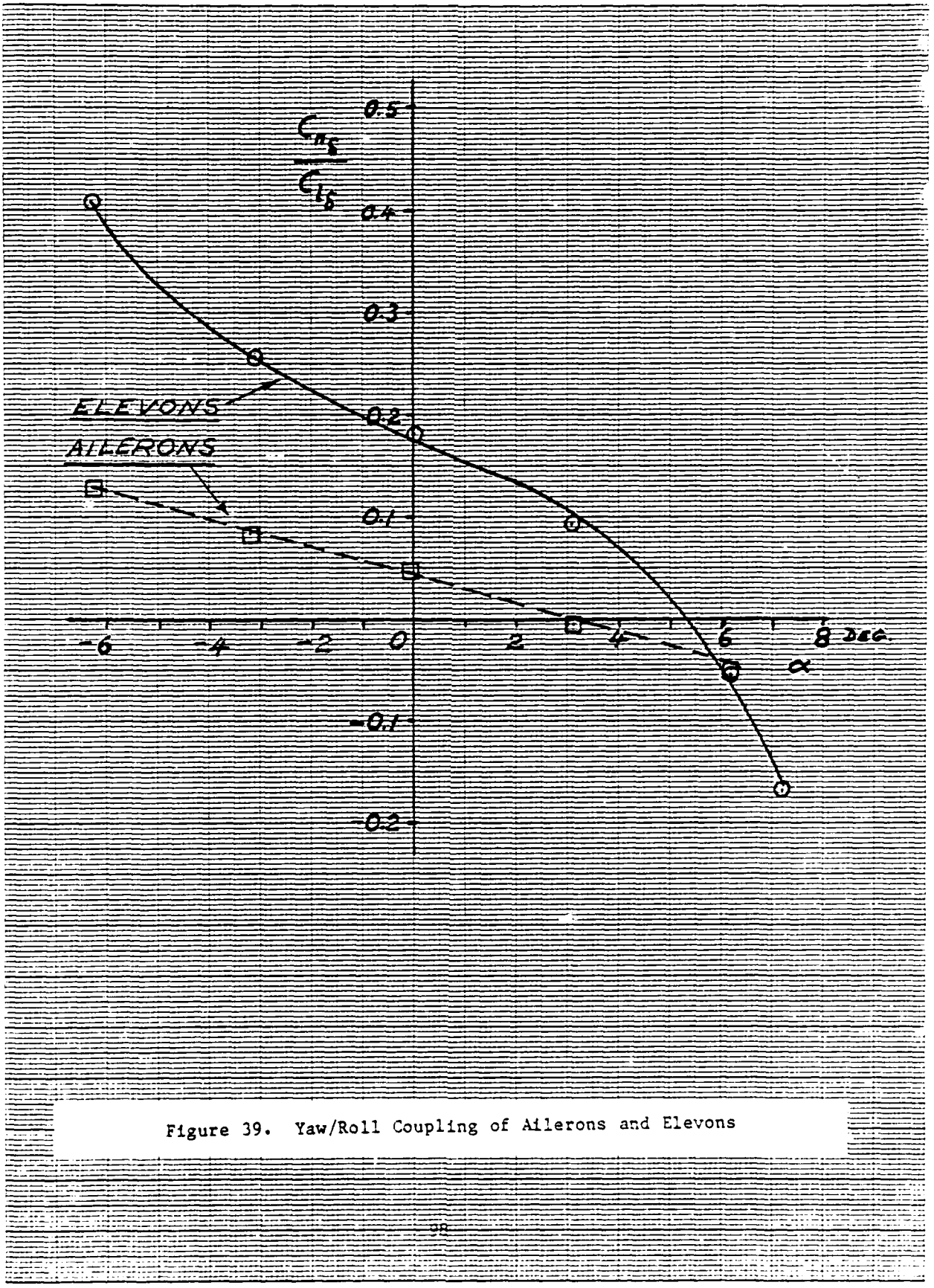

Figure 39. Yaw/Roll Coupling of Ailerons and Elevons

In addition to the data presented here, Vol. II presents measurements of C_L, C_m, and C_D, with positive, negative and neutral deflections of ailerons and elevons (see Figs. 23 and 24 of Vol. II). These data show that there are only negligible changes of pitching moment and lift as a result of equal and opposite control deflections. Thus the lateral controls do not produce any undesired longitudinal effects.

6.0 CONCLUSIONS AND RECOMMENDATIONS

6.1 CONCLUSIONS

1. Comparative low-speed wind tunnel tests of joined wing versus conventional wing configurations show that the theoretically-predicted induced drag advantage of the joined wing is attained or surpassed over a wide range of lift coefficients.

2. The trimmed maximum lift coefficient (based on exposed area) of joined wing configurations is higher than that of conventional configurations, particularly if a canard is added to the joined wing. The canard/joined wing interaction substantially increases C_{Lmax}.

3. The joined wing configurations exhibited milder stall characteristics than the conventional configurations, with little fall-off in lift coefficient at post-stall angles of attack.

4. For both the conventional and joined wing configurations tested the pitching moment varied nonlinearly with lift coefficient in the unstalled flow regime, giving a pitch-down characteristic. At post-stall conditions the joined wing displayed a pitch-up tendency, due to the flow remaining attached near the root of the front wing. At similar angles of attack the conventional configuration retained a pitch-down characteristic.

5. For the joined wing configuration tested here the directional stability contribution of the dihedralled wings did not fully compensate for the low directional stability supplied by the small vertical tail.

6. Front wing elevons provided effective pitch control. Rear wing ailerons gave effective roll control, with only very slight yaw moments and are preferable to front wing ailerons.

7. The strength advantage of full-scale (hollow) joined wings is not obtained with solid model wings. Such wings require reinforcing inserts to obtain the strength of solid monoplane wings of the same span and area.

8. The joined wing with approximately equal positive and negative dihedral angles provides a net positive dihedral effect which is approximately 50% greater than that of a conventional wing with 3 degrees of dihedral.

6.2 RECOMMENDATIONS FOR FURTHER WORK

1. Additional tests at higher Reynolds numbers, with a strengthened version of the existing model should be performed. These tests would check the effects of Reynolds number on the drag and high-lift characteristics.

2. Tests should be performed to exploit the high C_{Lmax} ned from canard/joined wing interactions. These tests should ir ide tests of trimmed C_{Lmax} using an elevator on the rear wing as a trimming control surface.

3. Analyses and tests should be performed to study the quantitative improvements in directional stability that can be obtained through employing increased negative dihedral on the rear wing with reduced positive dihedral on the front wing.

4. Theoretical methods of improved accuracy should be developed to calculate the induced drag and pitching moment characteristics of joined wings. Particular attention should be given to tailoring the high offset of the drag polar in order to achieve low trimmed induced drag over a wide range of lift coefficient.

5. Additional wind tunnel tests at higher Mach number should be performed, to study the transonic characteristics of joined wings.

6. Structural, aeroelastic, and preliminary design studies of airplane and missile configurations should be performed to quantify the gains in performance offered by the joined wing.

REFERENCES

1. Wolkovitch, J., Application of the Joined Wing to Cruise Missiles, ONR-CR212-266-1, Contract N00014-79-C-0953, N81-25068, ACA Industries Inc., Rancho Palos Verdes, CA, 1980.

2. Samuels, M. F., "Structural Weight Comparison of a Joined Wing and a Conventional Wing," J. Aircraft, 1982, pp. 485-491.

3. Lamar, J. E., A Vortex-Lattice Method for the Mean Camber Shapes of Trimmed Noncoplanar Planforms with Minimum Vortex Drag, NASA TN D-8090, 1976.

4. Letcher, J. S., "V-Wings and Diamond-Ring Wings of Minimum Induced Drag," J. Aircraft, Aug. 1972, pp. 605-607.

5. Kuhlman, J. M., and T. J. Ku, Numerical Optimization Techniques for Bound Circulation Distribution for Minimum Induced Drag of Nonplanar Wings: Computer Program Documentation, NASA CR-3458, 1982.

6. Torenbeek, E., Synthesis of Subsonic Airplane Design, Delft University Press, Holland, 1976.

7. Hoerner, S. J., Fluid-Dynamic Drag, Hoerner Fluid Dynamics, Brick Town, NJ, 1965.

8. Jacobs, E. N., and A. Sherman, Airfoil Section Characteristics as Affected by Variations of the Reynolds Number, NACA TR 586, 1936.

9. Althaus, D., Profilpolaren für den Modellflug, Neckar-Verlag VS-Villingen, West Germany, 1980.

10. Pope, A., and J. J. Harper, Low-Speed Wind Tunnel Testing, J. Wiley and Sons, New York, 1966.

11. Munk, M. M., The Minimum Induced Drag of Airfoils, NACA Rept. 121, 1921.

12. Margason, R. J., and J. E. Lamar, Vortex-Lattice Fortran Program for Estimating Subsonic Aerodynamic Characteristics of Complex Planforms, NASA TN D-6142, 1971.

13. Lamar, J. E., and B. B. Gloss, Subsonic Aerodynamic Characteristics of Interacting Lifting Surfaces with Separated Flow Around Sharp Edges Predicted by a Vortex-Lattice Method, NASA TN D-7921, 1975.

APPENDIX A

DISCUSSION OF JOINED WING WIND TUNNEL
MODEL STRUCTURAL CHARACTERISTICS

A.1 GENERAL DISCUSSION

As explained in Refs. 1 and 2, the joined wing requires an unconventional distribution of structural material for maximum strength. This distribution was not built into the wind tunnel models tested here, because of cost constraints. As a result, the joined wing model tested was less strong than the equivalent cantilever wing model. The test dynamic pressure and Reynolds numbers were consequently lower than those originally planned. Although no serious disadvantage resulted from this in the present test, the problem may recur in future joined wing tests, possibly limiting Mach number to undesirably low values. It therefore merits some further discussion, given below.

Consider Fig. A.1. This shows that the lift load acting upon any chordwise section of a joined wing at a distance y from the aircraft's plane of symmetry may be resolved into two components,

(1) An "inplane" component, $\Delta L \sin \vartheta$, inclined at the local "tilt angle," ϑ. This component acts within the plane of the truss formed by the joined wings.

(2) An "out-of-plane" component $\Delta L \cos \vartheta$.

The inplane component is well resisted by the truss structure, but the truss provides no special advantage in resisting the out-of-plane component. Therefore the joined wing structural material must be disposed so that each wing resists out-of-plane loads. For a full-scale aircraft, employing a conventional hollow wing structural box, this can be achieved by concentrating the wing box material at the maximum possible distance from the local plane of the truss (i.e., the plane x-x in Fig. A.1. This increases the wing's effective beam depth about its bending axis, as shown in the lower part of Fig. A.1. As shown in

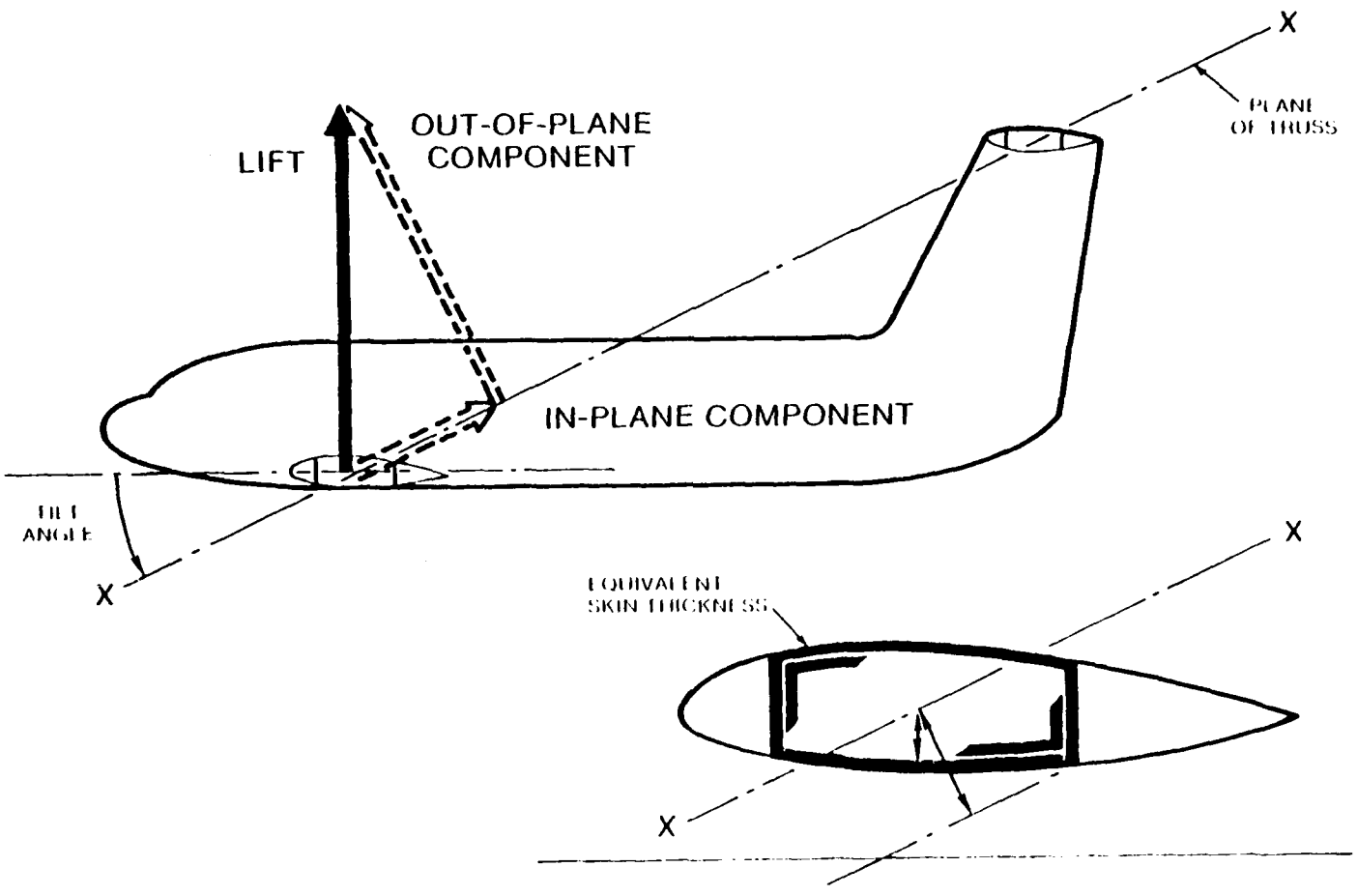

Figure A.1. In-Plane and Out-of-Plane Lift Components

Ref. 2 this form of structural material distribution provides a structure which is substantially lighter and stiffer than a conventional wing plus tail carrying the same total lift, with the same parasite and induced drag.

The foregoing discussion relates to full-scale (hollow) wings. It requires modification for model (solid) wings, constructed from uniform materials, with no voids. Most wind tunnel models employ solid wings. For such construction, comparing monoplane versus joined wings with similar spans and gross horizontal projected areas, the strength/weight ratios are found to be similar.

It can also be shown that (if identical airfoils are employed) the solid joined wing contains only half as much structural material as its above-defined cantilever counterpart. Hence, if constructed from the same material, the solid joined wing has only half the bending strength of the solid cantilever wing, and therefore it cannot be tested at more than half the limiting dynamic pressure of the cantilever wing.

This restriction was realized at an early stage in planning the tests described herein, but it was expected that the (wooden) joined wing could be strengthened by metal inserts. Subsequent detailed studies revealed that such inserts were too costly for the model construction budget. Solid metal wings also proved to be prohibitively expensive. Cost considerations therefore dictated unreinforced wood construction for both the joined and cantilever wings. As discussed in Section 1, this resulted in the test Reynolds numbers being lower than had originally been planned. No special problem resulted from this in the present tests, but in future joined wing tests such a limitation might not be acceptable.

In summary, the predicted structural advantages of the joined wing concept for full-scale (hollow) wings do not apply to wind tunnel models with solid wings constructed of uniform material. Such models may require reinforcing inserts of high-strength material to permit tests to be conducted at the desired Reynolds and Mach numbers.

A.2 MODEL STRENGTH AND RIGIDITY AS LIMITING FACTORS ON THE TEST CONDITIONS

For the reasons explained above the joined wing model strength limited the test dynamic pressure to approximately one half of the limiting dynamic pressure permitted by the strength of the monoplane wing. Thus static stress analysis of the monoplane wing indicated it would support a C_L of 1.2 at $q = 30.0$ lb/ft^2, whereas with an equal factor of safety (= 3.0 based on yield stress) and equal C_L the joined wing would be limited to $q = 15.0$ lb/ft^2. A further restriction was imposed on the joined wing after observing the stall buffet characteristics of the rear wing.

During runs at stalled and post-stalled conditions at $q = 7.5$ lb/ft^2 the monoplane wing tip oscillated approximately 0.6 inch peak-to-peak, in a normal buffeting mode. By contrast, at the same q and angle of attack, the joined wing tip oscillated only with an amplitude of approximately 0.1 inch peak-to-peak. However the rear joined wing developed a noticeable oscillation with a maximum amplitude of approximately 0.4 inch peak-to-peak at 1/3 of its span inboard from the tip. At this location the (steady component of) deflection of the rear joined wing also attained its maximum value. The co-location of this maximum steady deflection with the maximum oscillation amplitude caused some concern. However no model failure occurred during the tests, nor was any splitting of the wooden wing material found.

It is not known whether the observed buffet represented an incipiently dangerous condition, but since no flutter analyses had been performed it was decided to restrict the angle of attack to 7 degrees at $q = 15.0$ lb/ft^2. Therefore the joined wing tests done at $\alpha > 7$ deg were performed at $q = 7.5$ lb/ft^2 and hence a lower Reynolds number than the corresponding monoplane tests. Thus comparisons of post-stall behavior between the joined wing and the monoplane wing were not made at equal Reynolds numbers. However, the joined wing C_L vs. α results at $q = 7.5$ and $q = 15.0$ lb/ft^2 were in close agreement for $\alpha \leq 7$ degrees.


DATE
ILME